2016

Multifunctional Nanocarriers for Cancer Therapy

Bei Cheng
University of South Carolina

Multifunctional nanocarriers for cancer therapy

by

Bei Cheng

Bachelor of Engineering
Hubei University of Technology, 2007

Master of Science
Wuhan University, 2009

Submitted in Partial Fulfillment of the Requirements

For the Degree of Doctor of Philosophy in

Pharmaceutical Sciences

College of Pharmacy

University of South Carolina

2016

Accepted by:

Peisheng Xu, Major Professor

McInnes Campbell, Chairman, Examining Committee

Kennerly Patrick, Committee Member

Qian Wang, Committee Member

Igor Roninson, Committee Member

Lacy Ford, Senior Vice Provost and Dean of Graduate Studies

DEDICATION

I dedicate this work to my parents, brothers and my husband. I am really grateful for all your support. Thank you for the sacrifices you have made.

ACKNOWLEGEMENTS

I am very grateful that I have the opportunity to conduct research under the mentorship of Dr. Peisheng Xu. During the past five years, he has helped me quite a lot in my academia field and leading me on my way to an independent scientist. Next, I would like to acknowledge my committee members, Dr. Qian Wang, Dr. McInnes Campbell, Dr. Igor Roninson and Dr. Kennerly Patrick. Your constant support and valuable experience in academia world have broadened my perspective in science. I thank Dr. Padmavathy Nandha Premnath, Huacheng He and Dr. Sandra Craig for all your help me in utilizing lab facilities and scientific discussions. I thank Dr. Eleni Markoutsa for help in animal studies. I thank Dr. Feng Gao for teaching me on statistic software. I thank Dr. Hexin Chen's group for sharing research resources. I also want to thank all my friends for their support and making my life more exciting in Columbia. Last but not least, I would like to acknowledge my family members, my parents, my husband and my brothers for their constant support and love.

ABSTRACT

Cancer is one of the leading causes of human mortality and mortality in all diseases. There has been a boost in developing nanocarrier-based therapies for treating cancer or other diseases during the past decade. One of the major advantages about nanocarrier (with the size range from 1-1000 nm) lies in its ability to specifically target tumor and maximize drug accumulation in tumor foci through the enhanced permeability and retention effect. Advancement in nanotechnology has opened a new paradigm in pharmaceutical field. But new challenges have to be overcome in order to fully exploit the technology and improve safety in clinical application.

To improve their performance, at least two types of multifunctional nanocarriers are being developed in our lab. The first type of nanocarrier is glycol chitosan based polymer delivery system, which is a one-step preparation system, with excellent loading capacity. We can use the nanocarrier to guide its loading cargo such as anticancer agents to release in a particular subcellular location, or to load multiple drugs together to increase therapeutic efficacy. The other system is a gold nanoparticle gated mesoporous silica hybrid system, by which we are able to simultaneously execute multiple anticancer therapies such as the combination of photothermal therapy and chemotherapy. Compared with the first generation of nano-delivery system, our new nanocarrier enters cells more efficiently through sigma 2 receptors. Moreover, it can serve as a diagnostic tool

through PET (Positron emission tomography), and our study shows that it is able to detect all the spontaneously lung tumors. We believe that these multifunctional nanocarriers have the potential benefits in various areas of current pharmaceutical research including cancer diagnosis and treatment.

PREFACE

Cancer is among the leading causes of human morbidity and mortality of all the diseases worldwide. Three prevalent cancers among males are prostate cancer, colorectal cancer and melanoma, and in females they are breast cancer, uterine corpus and colon and rectum.[1] Although during the past decades a significant improvement has been made in extending patients' life or even curing some patients by chemotherapy, radiation or surgery, more efforts are still required to fight against this life threating disease. For all the subtypes of metastatic breast cancer and advanced pancreatic cancer, cytotoxic chemotherapy is still the fundamental strategy.[2] However, the traditional chemotherapeutic effect is often hampered by its side effects towards some important organs. For example, doxorubicin is a highly potent anticancer drug used to treat solid and hematopoietic tumors, but it can cause acute cardiac injury and chronic heart failure.[3] One of the common toxic effect associated with fluorouracil, oxaliplatin and irinotecan is hepatic steatosis with the frequency over 20%,[4] and for methotrexate, cytarabine and ifosfamide they are well known for central neurotoxic side effects.[5] Besides of these side effects, the poor pharmacokinetic parameters of some chemotherapeutical agents request for a frequent dose and often have insufficient bioavailability in tumor. Moreover, we are facing the complicating issues of cancer. No matter what kind of cancer or at which stage of cancer, there are constant needs for building up a personalized

therapy that has higher efficacy and less side effects. Therefore, a more advanced and systemic therapy is unmet need.

There has been a boost in developing nanocarrier-based therapies for treating cancer or other diseases during the past decade. One of the major advantages about nanocarrier lies in its selectivity in tumor foci through the enhanced permeability and retention effect (EPR, nanoparticles can accumulation tumor tissue through the highly porous vasculature structure of newly born tumor vessels and ineffective lymphatic drainage system).[6] The first generation of nanoformulation that enters the clinical can be categorized as liposome, PEGylated proteins, nanocrystals, protein-drug conjugates as well as polymer-based nanoparticles.[7] The representative examples include Abraxane (albumin-bound nanoparticles) for treating metastatic breast cancer,[8] Doxil (Doxorubicin liposome) for treating Kaposi sarcoma,[9] and Zinostatin stimalamer (polymer drug conjugates) for treating hepatocellular carcinoma. Advancement in nanotechnology has opened a new paradigm in pharmaceutical field. But more challenges have to be overcome in order to fully take advantage of this nanotechnology and push it to broader clinical applications. To improve their performance, various multifunctional nanocarriers are being developed by many groups. By infusing the original system with higher targeting efficacy, the function of diagnosis, higher drug-loading capacity and versatile drug-loading flexibility, the newer generation of nanocarries tends to be more efficient and practical in the era of personalized medicine.

With the goal above, three strategies have been developed and applied to improve the function of nanocarries in our thesis research. The first strategy is to functionalize the original polymer nanoparticles for selective intracellular delivery of drugs, which minimizes the off-target side effects. Because of specific environmental parameters, different subcellular compartments can be selectively targeted by specialized nanoparticles. For example, owing to the fact that lysosomes (pH range 4.5-5)[10] and cytosol and mitochondria have higher reducing environment, different stimuli-responsive nanoparticles made from polymers or metal particles have been designed and synthesized.[11] Disulfide bond, selenium or ferrocene and borate ester containing system were among the most popular oxidation-responsive systems for the intracellular delivery. Here, we developed an environment-sensitive peptide delivery system, dual secured nano-sting (DSNS), through the combination of a zwitterionic glycol chitosan and disulfide bonds. It released drug only if it went through an environment that had both acidic and reducing conditions.

The second strategy we utilized is to create multifunctional nanocarriers capable of diagnosis, therapy and therapeutic outcomes monitoring. Previous study showed that “theranostic particles”, with their unique optical properties, can either carry imaging molecules or acted as the imaging agent.[12] In our study, we fabricated gold nanosphere/mesoporous silica hybrid (GoMe) nanocarriers to encapsulate either a hydrophilic drug, doxorubicin, or a hydrophobic sensitizer, Pc 4. In the animal model study, the former nanocarrier not only showed the potential of providing a combined chemotherapy and photothermal (PTT) therapy

for cancer, but also demonstrated the ability of diagnosing lung cancer when radioactive copper was incorporated; by combining PTT and photodynamic therapy (PDT), the latter nanocarrier is able to kill cancer cells and eradicate head and neck cancer.

The third strategy we utilized is to generate multifunctional nanocarries with the capacity of co-delivering of different drugs. One of major advantages for co-deliver drugs is their suppression of the notorious chermoresistance and metastasis.[13] It is of particularly importance when a systemic chemotherapy is required for patients with middle- to late-stage of metastatic cancers. The classic example is to co-deliver anti-metastasis and chemotherapeutic agents, where angiogenesis inhibitor can normalize the tumor vasculature and potentiate the co-delivered chemotherapeutic drugs.[14] Especially at the low-dose of antiangiogenic/metronomic chemotherapy, this combination can achieve comparable efficacy but much less side effects and drug resistance.[15] In the last part of this project, we succeeded to combine the suramin, an inhibitor of VEGF (vascular endothelial growth factor) and bFGF (basic fibroblast growth factor), with doxorubicin in a bio-compatible polymer-based system, which partially utilized suramin as the constructing networks and showed that the new nanoparticle was able to improve median survival time for mice with breast cancer lung metastasis.

TABLE OF CONTENTS

LIST OF FIGURES

LIST OF ABBREVATIONS

CI ..... Combination index

CTAB ..... Cetyl trimethylammonium bromide

CTC ..... Circulating cancer cells

DLS ..... Dynamic light scattering

DMA 9, 10-dimethylanthracene

DME ..... Dulbecco's Modified Eagle Medium

DOX ..... Doxorubicin

DSNS ..... Dual secured nano-sting

DTT ..... Dithiothreitol

FBS ..... Fetal bovine serum

EDC ..... 1-Ethyl-3-(3-dimethylaminopropyl)-carbodiimide

EDTA ..... Ethylenediaminetetraacetic acid

EPR ..... Enhanced permeability and retention effect

FESEM ..... Field Emission Scanning Electron Microscope

aFGF ..... Acid fibroblast growth factor

bFGF ..... Basic fibroblast growth factor

FGFR ..... Fibroblast growth factor receptor

FRET ..... Förster resonance energy transfer

GCS ..... Glycol chitosan

GNC ..... Gold nanocage

GNR ..... Gold nanorod

GNS ..... Gold nanosphere

GNSH ..... Gold nanoshell

GoMe .....Gold/mesoporous silica hybrid nanoparticle

GSH .....Glutathione

^{1}H NMR.....1-dimensional proton nuclear magnetic resonance

HPLC ..... High-performance liquid chromatography

H&E ..... Hematoxylin and eosin stain

IEP ..... Isoelectric point

LDL .....Low density lipoproteins

LSPR .....Localized surface plasmon resonance

MBA ..... 4-methoxybenzoic acid

MPTMS ..... (3-mercaptopropyl) trimethoxysilane

MSN.....Mesoporous silica nanoparticle

MRI ..... Magnetic resonance imaging

MTT .....Thiazolyl Blue Tetrazolium Bromide

$NaBH_4$.....Sodium borohydride

NaOH..... Sodium hydroxide

NHS ..... N-Hydroxysuccinimide

NIR.....Near-infrared

PEG-SH .....Thiolated polyethylene glycol

PET.....Positron emission tomography

PBS.....Phosphate buffer

PDA ..... 2-(pyridin-2-yldisulfanyl)ethyl acrylate

PDI ..... Polydispersity index

PDT ..... Photodynamic therapy

PS ..... Photosensitizer

PTT ..... Photothermal therapy

RBCs ..... Red blood cells

RES ..... Reticuloendothelial system

ROS ..... Reactive oxygen species

SA ..... Succinic anhydride

SA-GCS ..... Succinic anhydride modified glycol chitosan

SA-GCS-SH ..... Thiolated acidified glycol chitosan

SEM scanning ..... Electron microscopy

SEM/EDX Scanning electron microscopy with energy dispersive X-ray spectroscopy

SM ..... Suramin

SOSG ..... Singlet Oxygen Sensor Green

SPDP ..... N-succinimidyl 3-[2-pyridyldithio]-propionate

SSNS ..... Single secure nano-sting

TCEP ..... Tris(2-carboxyethyl)phosphine

TEA ..... Triethlylamine

TEM ..... Transmission electron microscopy

TEOS ..... Tetraethyl orthosilicate

TNBSA ..... 2, 4, 6-trinitrobenzene sulfonic acid

TPP ..... Tripolyphosphate

VEGF ..... Vascular endothelial growth factor

CHAPTER 1

Dual secured nano-melittin for safe and effective eradicating cancer cells[1]

ABSTRACT

Clinical application of natural and synthetic amphipathic peptides (e.g., melittin) for cancer therapy is hindered by their notorious side effect, lysing red blood cells. To safely deliver a therapeutic peptide to the tumor tissue and kill cancer cells, we developed an environment-sensitive peptide delivery system, dual secured nano-sting (DSNS), through the combination of a zwitterionic glycol chitosan and disulfide bonds. Melittin loaded DSNS could kill almost 100% of MCF-7, HCT-116, SKOV-3, and NCI/ADR-RES (multidrug resistant) cancer cells at the concentration of 5 μM, while not showing hemolytic effect.

INTRODUCTION

The host defense amphipathic peptides found in eukaryotic cells have diverse activities in human and other species originating from their antibiotic, anticancer and anti-inflammatory activities.[16] These peptides oligomerize with phospholipids in cell membrane, result in pore formation, and subsequently cause cell death. Additionally, they act in a similar way on the membranes of internal organelles after intracellular transport, and induce cell apoptosis.[17]

---

[1]Cheng, B., Thapa, B., K.C., R., and Xu, P.*.2015. Journal of Materials Chemistry B. 3 (1): 25 - 29

Reprinted here with permission of publisher

Amphipathic peptides have been explored for cancer chemotherapy because of their wide-spectrum lytic properties. Melittin is one of the most promising amphipathic water-soluble α-helical cationic polypeptide and is derived from toxin of honey bee Apis melllifera.[18] Melittin partitions into and moves laterally in the cell membranes as monomers, followed by oligomerization into toroidal structures, forming pores which results in cell death.[18-19] Furthermore, most recent research showed that melittin can induce cancer cell apoptosis through the inhibition of JAK2/STAT3 pathway.[20] It is worth mentioning that melittin also suppresses the constitutively activated NF-κB, which is partially responsible for the development of drug resistance in cancer cells.[21] It is a very attractive cancer therapeutic agent, because cancer cells are less likely to develop resistance to cytolytic peptides.[19a, 22]

Despite all of these advantages, its non-specific cytolytic activity could lead to off-target effects such as hemolysis (lysis of red blood cells) when administrated intravenously. Besides that, positively charged peptide could be cleared from blood circulation rapidly by the reticuloendothelial system (RES) system.[23] Several groups developed melittin delivery systems either by covalently fusing melittin with receptor-targeted peptide motifs or through physically encapsulating it into liposomes or polymer nanoparticles to attenuate its hemolytic effect while achieving therapeutic efficiency comparable to free melittin.[24] Compared with free melittin, their anticancer efficacies were significantly decreased for the encapsulated form. Until recently, Soman et al. developed a liposome based melittin nanocarrier (“nanobee”), which showed

promising results in inhibiting the growth of melanoma tumors.[25] Despite the encouraging outcome of “nanobee”, they also found that “nanobee” was about five-fold less effective as that of melittin for the tested cancer cells.

An ideal melittin carrier should be able to completely quench its hemolytic activity while fully retaining its advantages, including wide spectrum and potent anticancer activities. To solve this dilemma, we rationally designed a melittin delivery system by integrating a zwitterionic glycol chitosan and disulfide bonds. Due to its zwitterionic property, succinic anhydride modified glycol chitosan (SA-GCS) shows negative surface charges at physiological pH. Positively charged melittin can form complexes with SA-GCS through the electrostatic effect. The complex will be further stabilized through disulfide crosslinking to yield dual secured nano-sting (DSNS) by aerial oxidation (**Figure 1.1A**).

RESULTS

Functionalization of zwitterionic glycol chitosan

The zwitterionic glycol chitosan was synthesized from glycol chitosan by acetylation with succinic anhydride. First, glycol chitosan was depolymerized by potassium persulfate according to the literature and purified by dialysis against DI water.[26] The molecular weight or the deacetylation degree of commercial glycol chitosan purchased from Sigma-Aldrich wasn’t strictly controlled. By depolymerization, we were able to minimize the batch to batch difference on molecular weight, solubility and cytotoxicity of GCS. Glycol chitosan was depolymerized by free radical degradation with thermal dissociation initiator potassium persulfate, which can maintain the structure integrity of glycol chitosan

during depolymerization. The resultant molecular weights of GCS was depend on the degradation time, a 0.5 h reduction time led to a final molecular weight of 40 kDa, and the longest degradation time (t=24 h) resulted in a 10 kDa molecular weight. Taking into account of the advantages of solubility, cytotoxicity and binding affinity, the resulting polymer was depolymerized for 2 h and achieved a molecular weight of 28 kDa and PDI of 1.38 (**Figure 1.2**). After that, glycol chitosan was modified according to our previously published method with succinic anhydride (**Figure 1.3**).[23, 27] SA-GCS showed negative surface charge at pH 7.4, and positive surface charge at pH below its isoelectric point (IEP) (**Figure 1.4B**). Furthermore, the IEP of the modified glycol chitosan can be tuned by adjusting the feeding ratio of succinic anhydride and glycol chitosan. To introduce free thiol groups, SA-GCS was reacted with N-succinimidyl 3-[2-pyridyldithio]-propionate (SPDP) and subsequently cleaved with tris(2-carboxyethyl)phosphine (TCEP) to achieve thiolated modified glycol chitosan (SA-GCS-SH) (**Figure 1.1B, 1.4A**). DTNB reacted with thiol groups in GCS and generated TNB product which was detectable at 412 nm. DTNB assay showed that each polymer chain contains 8.7 free SH groups. The IEP of the SA-GCS slightly decreased after the thiolation (**Figure 1.4B**).

To verify that zwitterionic glycol chitosan can form complexes with positively charged melittin, we fabricated the single secure nano-sting (SSNS) by mixing SA-GCS with melittin at pH 7.4 for 2 h at room temperature. The binding efficiency for SA-GCS was determined by measuring the fluorescence intensity of the tryptophan residue of melittin at λexi: 280nm, λemi: 350 nm. Fluorescence

measurement showed that with the increase of SA-GCS polymer, the detectable free melittin gradually decreases and achieved 100% encapsulation at the polymer to melittin ratio (W/W) of 40 (**Figure 1.5**).

To further stabilize the complex, inhibit its premature release of melittin, and eliminate its potential side effects, we substituted the SA-GCS with SC-GCS-SH and aerially oxidized the complex to promote the formation of disulfide bond among the SA-GCS-SH polymers to achieve so called dual secured nano-sting (DSNS). Since safety is an essential requirement for melittin related delivery, polymer to melittin ratio (W/W) of 200 was selected to ensure that no free melittin was remaining after the formation of the complexes. The formation of DSNS was confirmed by dynamic light scattering (DLS) (**Figure 1.6**) and transmission electron microscopy (TEM) (**Figure 1.7**). The hydrodynamic size of SSNS (220.2 nm, PDI: 0.191) was slightly increased to 223.4 nm after oxidation (PDI: 0.161). The size determined by DLS was larger than that obtained by TEM. This is because TEM measured the size of solid particles while DLS measured the hydrodynamic size of particles which includes the hydration shell surrounding a particle. This slight size difference between SSNS and DSNS reflected the size decrease and increase due to the formation of intra-particle and inter-particle crosslinking, respectively. Surface charge of the both nano-complexes at pH 7.4 was slightly negative (**Figure 1.8**), which will help the nano-complexes escape from the detecting of reticuloendothelial system and take advantage of the enhanced permeability and retention effect (EPR) of tumor tissue.[28] HPLC

confirmed that no any free melittin existed in the particle suspensions of SSNS and DSNS (**Figure 1.9**).

Investigate the pH responsiveness of nano-complexes by FRET

To evaluate the stability of SSNS and DSNS, Förster resonance energy transfer (FRET) technology was employed.[29] Before the fabrication of SSNS and DSNS, melittin and zwitterionic polymer were conjugated with Sulfo-Cy5-NHS and Cy3-NHS, respectively. Cy5-melittin was mixed with Cy3-SA-GCS and Cy3-SA-GCS-SH to achieve SSNS and DSNS, respectively (**Figure 1.10A**). DSNS exhibited a higher FRET signal than SSNS (**Figure 1.10B**) at pH 7.4, indicating that DSNS was tighter than SSNS. To evaluate the nano-sting stability at different pH environments, FRET signal was recorded in the pH range from 7.4 to 3.7. As the pH shifting from 7.4 to the IEPs of the polymers, the FRET intensities of both SSNS and DSNS increased and reached maximum at the pH close to the IEPs of the polymers, indicating the formation of more condensed nanoparticles. Similar to other zwitterionic macromolecules, SA-GCS showed lowest solubility at its IEP. The formation of water insoluble polymer would cause the condensation of SSNS and DSNS, and resulted in the highest FRET signal. SA-GCS displayed positive surface charge at pH lower than its IEP (**Figure 1.4B**), which would induce the repulsion between SA-GCS and positively charged melittin, similar to the scenario of nano-complex inside lysosome (**Figure 1.1**). As expected, both SSNS and DSNS displayed reduced FRET signal when environment pH was further decreased. At the pH of 3.7, SSNS showed a FRET intensity far less than that at pH 7.4, indicating the dissociation of nanoparticle. By contrast, the lowest FRET intensity DSNS reached at pH 3.7 was still higher than that of SSNS at pH

7.4, suggesting that the formed disulfide bonds did restrict melittin from premature release upon the fluctuation of pH. There was one pH unit left shift of the FRET curve from their corresponding IEPs, which we think was due to the lag response of nano-complexes to the change in environmental pH. The dual secured effect was also evidenced by the slower melittin release from DSNS than SSNS, as well as more melittin released at pH 5.0 than pH 7.4 (**Figure 1.11**).

Investigate the hemolytic activity of nano-complexes

To validate that the combination of zwitterionic polymer coating and disulfide crosslinking can effectively quench the hemolytic activity of melittin in DSNS, a hemolytic assay was carried out. SSNS and DSNS were incubated with red blood cells (RBCs) in PBS (pH 7.4) first, followed by centrifugation to separate the intact RBCs from the released hemoglobin. As shown in **Figure 1.12A**, melittin lysed almost all RBCs at the concentration of 1 μM. The formation of SSNS partially inhibited the hemolytic activity of melittin. In contrast, there was no detectable red color in the supernatant of RBCs incubated with DSNS at the melittin concentration of 5 μM. The hemolytic activities of SSNS and DSNS were further quantified by UV spectrophotometer. **Figure 1.12B** showed that free melittin was highly lytic to RBCs, lysed almost 100% RBCs at 2 μM, which is the major obstacle for its clinical application. The hemolytic activity of melittin in SSNS was significantly quenched after its complexation with zwitterionic glycol chitosan. The residual hemolytic activity indicated that some melittin was released when incubating with RBCs. Further stabilized through the formation of

disulfide bonds, DSNS did not show any hemolytic activity at 2 μM and only caused very few RBCs lyses at the concentration of 5 μM. Therefore, we proved that SSNS was safer than free melittin, while DSNS was almost non-toxic to RBCs up to the melittin concentration of 5 μM in pH 7.4 buffer.

To investigate the intracellular membrane lytic activity of SSNS and DSNS, RBCs were co-incubated with melittin, SSNS, or DSNS in PBS (pH 5.0) buffer or PBS (pH 7.4) supplemented with 10 mM glutathione (GSH) to mimic the environments in the acidic lysosome and reducing cytosol, respectively. Acidic pH and reducing environment quenched the hemolytic activity of melittin (**Figure 1.13**), which is consistent with others' observation.[30] SSNS at the concentration of 0.5 and 1.0 μM displayed much higher hemolytic activities in acidic pH than that in pH 7.4, suggesting the release of free melittin at low pH, which was consistent with our FRET observation in **Figure 1.10B**. In contrast, because of the restraint of disulfide bonds, acidic stimulus couldn't trigger the release of melittin from DSNS (**Figure 1.10B**), and induced only slightly more RBCs lysis (**Figure 1.13**). As expected, the addition of 10 mM GSH to pH 7.4 buffer greatly enhanced DSNS's hemolytic activity, reached the similar level as that of SSNS at the concentration of 2 and 5 μM (**Figure 1.13**). Furthermore, the hemolytic activity of DSNS was investigated in 50% serum containing buffer to mimicking blood. **Figure 1.14** revealed that DSNS was also stable in blood simulating buffer, not causing RBC lysis. Based on these observations, we validated that DSNS should be safe during circulating in the blood stream while effectively lysing intracellular organelles as illustrated in **Figure 1.1**.

Cellular uptake of nano-complexes

To investigate how the stability of nano-complexes affects their cellular uptake, confocal microscopy was employed. SSNS and DSNS were fabricated as described above except that Cy3-SA-GSC was used instead of SA-GCS. More red spots were detected in cells treated with DSNS than SSNS (**Figure 1.15**), which suggested that more DSNS nano-complexes entered cancer cells intact than their SSNS counterparts, while some SSNS had dissociated before endocytosis, evidenced by less Cy3 labeled SA-GCS uptake. Since DSNS was more stable than SSNS, as shown in **Figure 1.10** and further prove by **Figure 1.12**, DSNS won't premature release melittin when contacting with serum protein and red blood cell (**Figure 1.15**). In contrast, SSNS was only stabilized by the electrostatic effect, which can be dissociated by the competing effect of serum protein. Therefore, more DSNS entered cancer intact than SSNS.

Cell killing effect of nano-complexes

Due to the limitation of SSNS associated unwanted hemolytic toxicity, further anticancer efficacy evaluation only included DSNS. NCI/ADR-RES (OVCAR-8 Adriamycin-resistant ovarian) cancer cells were co-cultured with free melittin and DSNS (melittin concentration of 5 μM) for 24 h.[31] MTT reagent (3-(4, 5-Dimethylthiazol-2-yl)-2, 5-diphenyltetrazolium bromide) was added after that. Living cells could convert MTT reagent into water insoluble purple crystals (**Figure 1.16A**). The absence of crystals in both melittin and DSNS treated cells indicated that the cells in both treatments were dead. To investigate the possible mechanism of cell death, we examined the cell morphology after treatment. Cells creanated after co-incubating with free melittin and lost its original shape (**Figure**

1.16B). In contrast to its free melittin treated counterpart, cells in **Figure 1.16C** kept their intact shape after DSNS treatment. Since melittin can attack cancer cells by forming pore structures on cell membrane [31c], we postulate that the cell death in melittin treatment group was mainly due to the loss of cell membrane integrity. DSNS, due to the dual-secured mechanism, could effectively enter cancer cells (**Figure 1.15**) and release melittin intracellularly (**Figure 1.1 and Figure 1.13**). Therefore, we postulate that DSNS treated cells were killed mainly due to the compromised membranes of internal organelles (e.g., mitochondria). After co-incubating with DSNS and followed by JC-1 staining, the emerging green fluorescence signals in DSNS treated cell (**Figure 1.17**) confirmed that cancer cells were killed due to mitochondria damage.

The anticancer efficacy of DSNS was further quantitatively evaluated in four types of cancer cells, HCT-116 colon cancer cells, MCF-7 breast cancer cells, SKOV-3 ovarian cancer cells, and NCI/ADR-RES/OVCAR-8 ovarian (Adriamycin-resistant) cancer cells by MTT assay. As expected, both free melittin and DSNS showed dose-dependent cytotoxicity and could kill 100% of the cancer cells at a high dose (**Figure 1.16**). It is worthwhile to note that DSNS was more effective in killing HCT-116 cells. DSNS killed 100% of HCT-116 cells at the melittin concentration of 5 μM, at which free melittin could only kill 76% cancer cells (**Figure 1.16D**). Most importantly, DSNS only showed negligible hemolytic activity at the same concentration (**Figure 1.12B**). A similar anticancer effect was observed for MCF-7 breast cancer cells and SKOV-3 ovarian cancer cells (**Figure 1.16E and 1.16F**). Furthermore, we also found that DSNS killed 100% of

Adriamycin-resistant ovarian cancer cells at the melittin concentration of 5 μM (**Figure 1.16G**), which have developed multidrug resistance. Altogether, we proved that anticancer capacity of melittin of DSNS, in contrast to other melittin carrier systems,[21, 24a] was fully retained. In addition, the polymer carrier itself was not toxic for all four tested cell lines (**Figure 1.18**).

DISCUSSION

In summary, we have fabricated DSNS nano-complexes through the electrostatic absorption of zwitterionic glycol chitosan and disulfide crosslinking to deliver melittin for cancer therapy. The hemolytic activity of melittin in DSNS could be completely quenched by our unique dual secured design. Due to the pH and redox potential dual responsiveness of DSNS, the wide-spectrum anticancer activity of melittin was fully retained, eradicating 100% of four types of tested cancer cell lines, including a drug resistant cell line. These studies demonstrated that the combination of zwitterionic polymer and redox sensitive bonds offer a new strategy for safe and effective therapeutic peptide delivery. The next step of research would be adding cancer cell targeting ligands, such as folic acid, anisamide, and disaccharide moiety of bleomycin,[32] to the DSNS to further enhance its tumor specificity.

MATERIALS AND METHODS

Materials

Glycol chitosan (GCS, Mw = 200 kDa; degree of deacetylation = 90%), potassium persulfate, sodium borohydride, succinic anhydride, melittin from bee venom, sodium dodecyl sulfate, D-(+)-trehalose dehydrate, N-succinimidyl 3-[2-

pyridyldithio]-propionate (SPDP), tris(2-carboxyethyl)phosphine (TCEP), triethlyl amine (TEA), ethylenediaminetetraacetic acid (EDTA), and dimethyl sulfoxide (DMSO) were purchased from Sigma-Aldrich (St Louis, MO, USA). L-cysteine HCl and Ellman's reagent were purchased from Thermo Scientific (Rockford, IL, USA). Dulbecco's Modified Eagle Medium (DMEM) supplied with high glucose, trypsin and penicillin-streptomycin were purchased from Invitrogen (Carlsbad, CA, USA). Fetal bovine serum (FBS) was purchased from ATCC (Manassas, VA, USA).

Depolymerization of glycol chitosan

Glycol chitosan (Mw: 200 kDa) was first depolymerized to Mw 28 kDa using potassium persulfate, and then modified by reacting with succinic anhydride and SPDP sequentially. Briefly; glycol chitosan (400 mg) was dissolved in 37.5 ml of hydrochloric acid (2%, v/v). After that, potassium persulfate (67.5 mg) was added to the above glycol chitosan solution to start the depolymerization. The reaction was kept at 70 °C for 2 h and then stopped by adding sodium borohydride (300 mg). The reaction mixture was neutralized with sodium hydroxide (1 M). The resulting polymer was dialyzed (Spectra 7 MWCO: 3500 Da) against ddH2O for 24 h followed lyophilization. Molecular weight of the polymer was obtained from GPC (Viscotek GPCmax VE 2001 GPC solvent/sample module, Viscotek VE 3580 RI detector and 270 Dual Detector) using 0.3 M acetic acid, 0.3 M sodium acetate, 0.02% sodium azide, 1% ethylene glycol (pH 4.5) as the mobile phase.

Acetylation of glycol chitosan with succinic anhydride (SA-GCS)

Succinic anhydride (SA) was grafted onto the above yielded low molecular weight glycol chitosan (28 kDa) by acidification reaction. Briefly; glycol chitosan (30 mg) was dissolved in deionized water (6 mL) and succinic anhydride (4.17 mg) was added under stirring. After 2 h of reaction at room temperature, the pH of the reaction mixture was adjusted to 8 with NaOH (1 M). The reaction was then allowed to proceed for another 2 h. The product was purified by dialysis (Spectra 7 MWCO: 3500 Da) against water (pH 9) for one day and lyophilized for 48 h. The structural composition of modified glycol chitosan (SA-GCS) was characterized by ^{1}H-NMR spectroscopy. The appearance of methylene proton peaks at δ = 2.4 to 2.6 ppm corresponding to succinic acid along with the glycol chitosan peaks at δ = 2.06, 2.75, 3.7 and 4.5 ppm (**Figure 1.3**). To determine the IEP of SA-GCS, ζ potential was measured as a function of pH using Zetasizer Nano-ZS (Malvern, UK). In a typical experiment, 0.5 mg/mL polymer solution was prepared in NaCl (10 mM), and the surface charges of SA-GCS at different pH were recorded.

Modification of acetylated glycol chitosan (SA-GCS-SH)

To generate thiol groups on SA-GCS, SA-GCS was reacted with SPDP. The introduced disulfide bonds were then cleaved by TCEP to yield free thiol groups. Briefly; SA-GCS (60 mg) was first dissolved in dimethyl sulfoxide (10 mL). TEA (300 µL) and SPDP (21.63 mg) were then added under stirring. After overnight reaction at room temperature, the disulfide bonds were cleaved by adding TCEP thereby generating free thiol group. Then, the polymer was purified

by dialysis (Spectra 7 MWCO: 3,500 Da) against 10 mM EDTA (24 h) followed by ddH_2O (24 h). The product was obtained after lyophilization for 48 h and stored at -20 °C. IEP of SA-GCS-SH was determined in a similar way as SA-GCS. The concentration of thiol group was quantified by DTNB assay. The number of thiol groups per polymer molecule was found to be 8.7 as calculated by DTNB assay.

Nano-complexes preparation and characterization

Melittin and SA-GCS-SH were dissolved in Tris buffer saline (TBS) pH 7.4 to get 0.1 mg/mL and 5 mg/mL, respectively. Then, 1 ml melittin solution was incubated with different amounts (0.1 to 4 mL) of SA-GCS-SH solution for 1 h at room temperature to get non-crosslinked complexes (single secured nano-sting, SSNS). To develop cross-linked complexes (dual secured nano-sting, DSNS), SSNS was aerially oxidized for 2 h at room temperature. SSNS and DSNS were freeze-dried with 5% trehalose and stored at -20 °C until use. The binding efficiency of SA-GCS-SH was measured by measuring the fluorescence of free melittin. Free melittin from the complexes was separated by centrifugal filtration at 14,000 rcf for 8 min using Nanosep 30 K Omega (Pall corporation, USA) and the concentration was determined by measuring its fluorescence (λexi=280nm, λemi=350 nm) using a SpectraMax M5 Multi-Mode Microplate Reader (Molecular Devices). Nano-complexes prepared at the ratio of 200:1 (polymer: melittin, w/w) were used for the following experiments.

The size and surface charge (ξ-potential) of the complexes were measured using a Zetasizer Nano-ZS (Malvern, UK) at pH 7.4. The morphology of the complexes was observed by transmission electron microscopy (Hitachi H-

800 TEM) using a formvar/carbon coated Copper Grids (Electron Microscopy Science). The original complexes solution (5 µL) was dropped on a grid, washed with ddH_2O (3 ×) to remove the remaining salt, and dried with a tissue paper. HPLC determination of melittin was carried out with a Waters 2996 instrument equipped with a photodiode array detector and a hypersil gold column (250 × 4.6 mm, Fisher); mobile phase: mixture of acetonitrile and water supplemented with 0.1 % TFA (linear gradient from 4:96 to 64:36, v/v, over 60 min); flow rate: 1.5 mL/min; detection: 220 nm. The retention time for melittin was 41.6 min. Standard solutions were prepared by dissolving melittin in ddH_2O followed by a series of dilutions. Melittin stock solution was prepared at 100 µg/mL. For sample preparation, 50 µg of SSNS and DSNS were dissolved in 500 µL ddH2O and the free melittin solution was collected by centrifugation at 13,000 rcf for 30 min twice with Nanosep centrifugal device 10K Omega (Paul life sciences). The resulting filtrate (50 µL) was injected for HPLC determination. No peak detected at 41.6 min suggested that both SSNS and DSNS were free of free melittin (**Figure 1.9**).

FRET measurement

The donor fluorescence dye Cy3-NHS was chemically conjugated with SA-GCS and SA-GCS-SH prior to forming the complex. Similarly, the receptor fluorescence dye Sulfo-Cy5-NHS was conjugated with melittin. The conjugated Cy3 amounts in SA-GCS and SA-GCS-SH were adjusted carefully to ensure that the same conjugation efficiency was achieved, which was further validated by measuring the fluorescence intensity of Cy3 with a SpectraMax M5 Multi-Mode Microplate Reader. After that, SSNS was fabricated from Cy3-labeled SA-GCS

and Cy5-labeled melittin, while DSNS was fabricated from Cy3-labeled SA-GCS-SH and Cy5-labeled melittin. Cy3 and Cy5 dual-labeled SSNS and DSNS were prepared following the same protocol except that the DSNS needed aerial oxidation. Therefore, the amount of each dye in SSNS and DSNS was the same. The titration of nano-complex was carried out by adding 0.1 M HCl and NaOH to adjust pH to the pre-designed values. Both SSNS and DSNS samples were loaded into Coring® 96 well black flat bottom plates. Samples were excited at 500 nm with the cutting off 530 nm. The entire fluorescence spectra (from 530 nm to 750 nm) of both nano-complexes were then recorded as a function of the pH with the help of a SpectraMax M5 Multi-Mode Microplate Reader (Molecular Devices).

Release kinetics of SSNS and DSNS

Cy5 labeled melittin were fabricated into SSNS and DSNS as described above. SSNS and DSNS samples (2 mL) were loaded into dialysis bags (MWCO: 6000-8000). The dialysis bags were put into different media (pH 7.4,10 mM PBS and pH 5, 10 mM acetic acid buffer) at 37 °C under continually stirring. At predesigned time (1, 2, 4, 8 h), 1 mL sample was taken and supplemented with 1 mL corresponding fresh medium. Samples were lyophilized and re-suspend in 200 µL ddH_2O. To calculate the release amount of melittin, the originally labeled Cy5-melittn was employed to obtain standard curve with the help of a fluorescence microplate reader. The fluorescence intensities of released samples were quantified under excitation of 630 nm and emission of 670 nm.

Hemolytic assay

Sprague Dawley Rat whole blood was purchased from Bioreclamation LLC (NC, USA). Briefly, RBCs were washed with NaCl (210 mM) until no red color was visible in the supernatant. The washed RBCs were used to compare hemolytic effects of melittin, SSNS and DSNS using DI water as positive control and PBS (pH 7.4) as negative control. Melittin of different concentrations (0.1 to 5 μM) and SSNS or DSNS (equivalent with free melittin) were added to fixed number of washed RBCs (2.5×10^7 cells) and incubated at 37 ºC for 1 hour. The release of hemoglobin was quantified by measuring the absorbance at 405 nm of the supernatant in a microplate reader (ELX808, Bio-Tech Instrument) after centrifugation at 300 rcf for 2 minutes. The results were expressed relative to the reference standard. To investigate the effect of pH and redox potential on the hemolytic activity of SSNS and DSNS, nano-complexes were co-incubated with RBCs in PBS (pH 5.0) and PBS (pH 7.4) supplemented with 10 mM GSH, respectively. The stability of DNSN was also tested by co-incubating RBCs with DSNS in PBS buffer containing 50% serum.

Confocal microscopy

HCT-116 cells were seeded at a density of 2×10^4 cells per chamber slides and allowed to grow for 24 h. SA-GCS and SA-GCS-SH were conjugated with Cy3 followed by excessive dialysis to remove free Cy3. The purified Cy3 labeled polymer were used to prepare SSNS and DSNS. After treated with SSNS and DSNS for 2 h at 37 °C in a 5% CO_2 incubator, cells were washed with PBS three times and fixed with 4% formaldehyde in PBS, followed by staining with

Hoechst33342 1 μg/mL (Invitrogen) and washed again with PBS for 3 times. Finally, cells were imaged with confocal laser scanning microscopy (Zeiss LSM 700).

JC-1 Staining

HCT 116 cells were seeded in each petri dish at density of 300K cells per dish. After overnight incubation, cells were treated with 2 μM Melittin or DSNS for 1 h. Cells were then stained with JC-1 for 30 min (Cayman chemical, MI), and observed under confocal microscope using FITC and Texas Red channels.

Cytotoxicity assay

The anticancer activities of melittin and DSNS in MCF-7, HCT-116, SKOV-3 and NCI/ADR-res cells were evaluated by MTT assay using melittin as a positive control and non-treated cells as a negative control. The cells were seeded in 96-well plates at an initial density of 12,000 cells/well in 150 μL of DMEM medium supplemented with 100 U penicillin/streptomycin and 10% FBS. After 24 h, the medium was replaced with 150 μL of fresh medium containing DSNS and melittin (corresponding to 0.1 to 10 μM melittin) and incubated for another 24 h. After the defined time of co-incubation, the media were replaced with 100 μL fresh media containing 1 mg/mL MTT reagent and incubated for 4 h. The formed MTT crystal was dissolved with a stop solution and the finally optical density of the medium was measured using a microplate reader (ELX808, Bio-Tech Instrument, Inc) at λ = 595 nm. The cytotoxicity of melittin and DSNS was calculated as relative to the control group (untreated cell). The cytotoxicity of oxidized SA-GCS-SH polymer was evaluated in parallel.

A

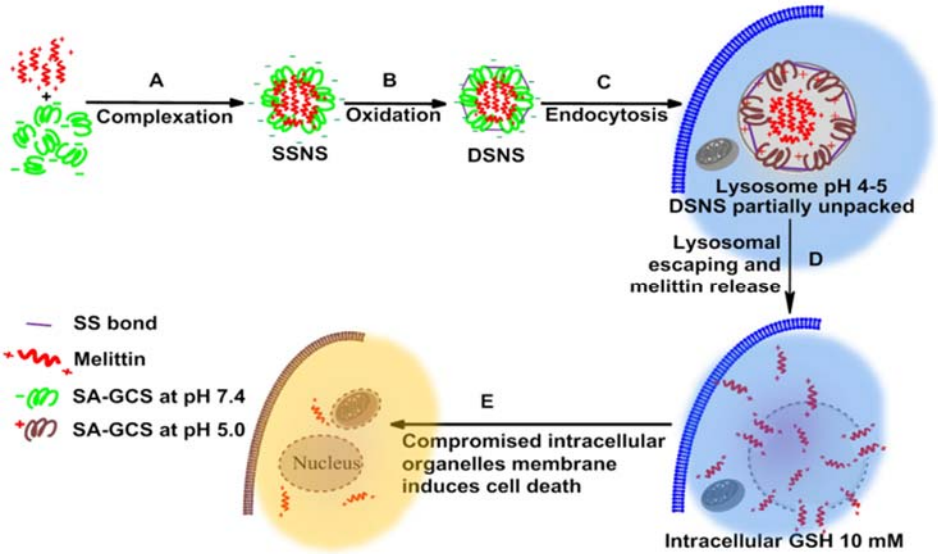

B

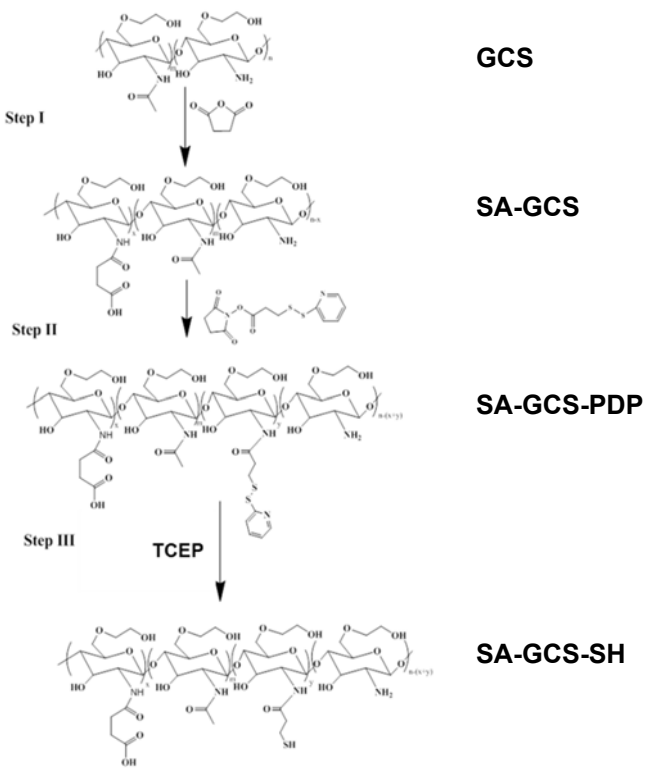

Figure 1.1 Schematic illustration of complex formation and reaction scheme of the polymer synthesis. (A) Schematic illustration of the formation and intracellular pathway of DSNS. (B) Reaction scheme for synthesis SA-GCS, SA-GCS-PDP, and SA-GCS-SH.

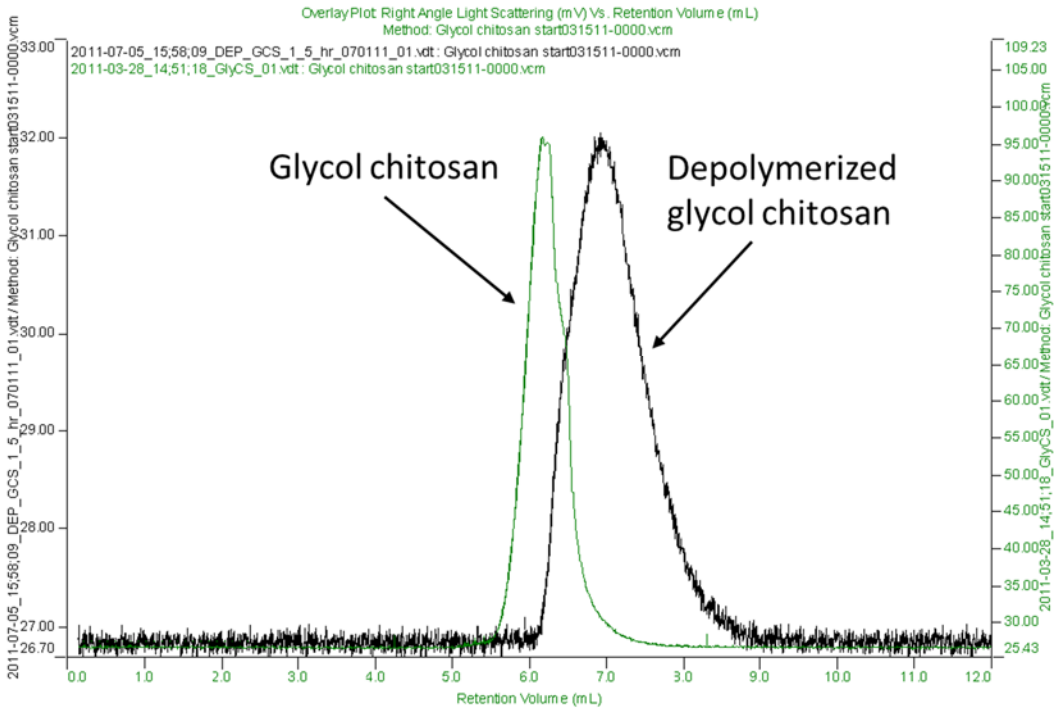

Figure 1.2 The GPC spectra of glycol chitosan and depolymerized glycol chitosan.

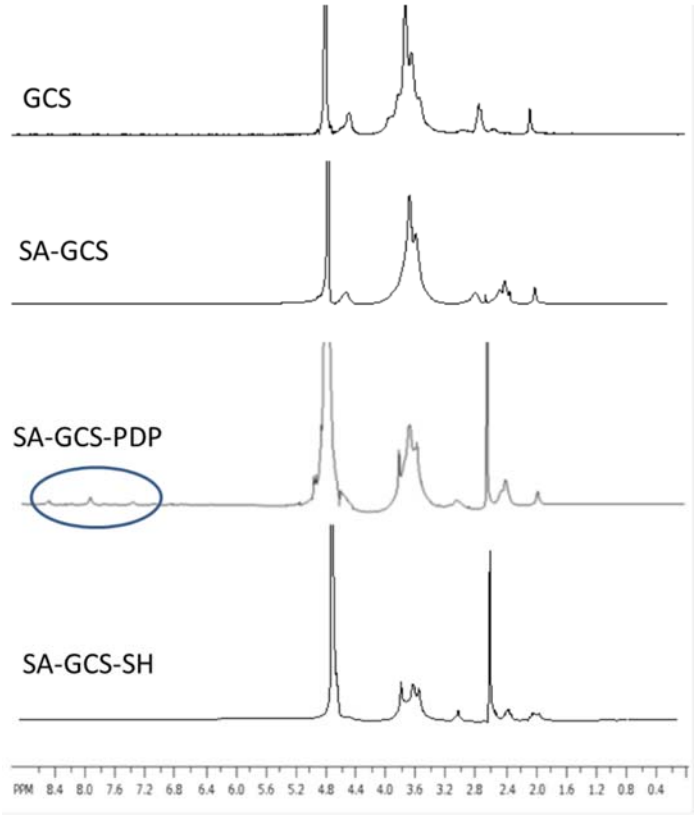

Figure 1.3 The ^{1}H-NMR spectra in D_2O of GCS, SA-GCS, SA-GCS-PDP, and SA-GCS-SH. The circled area indicates the peaks of PDP.

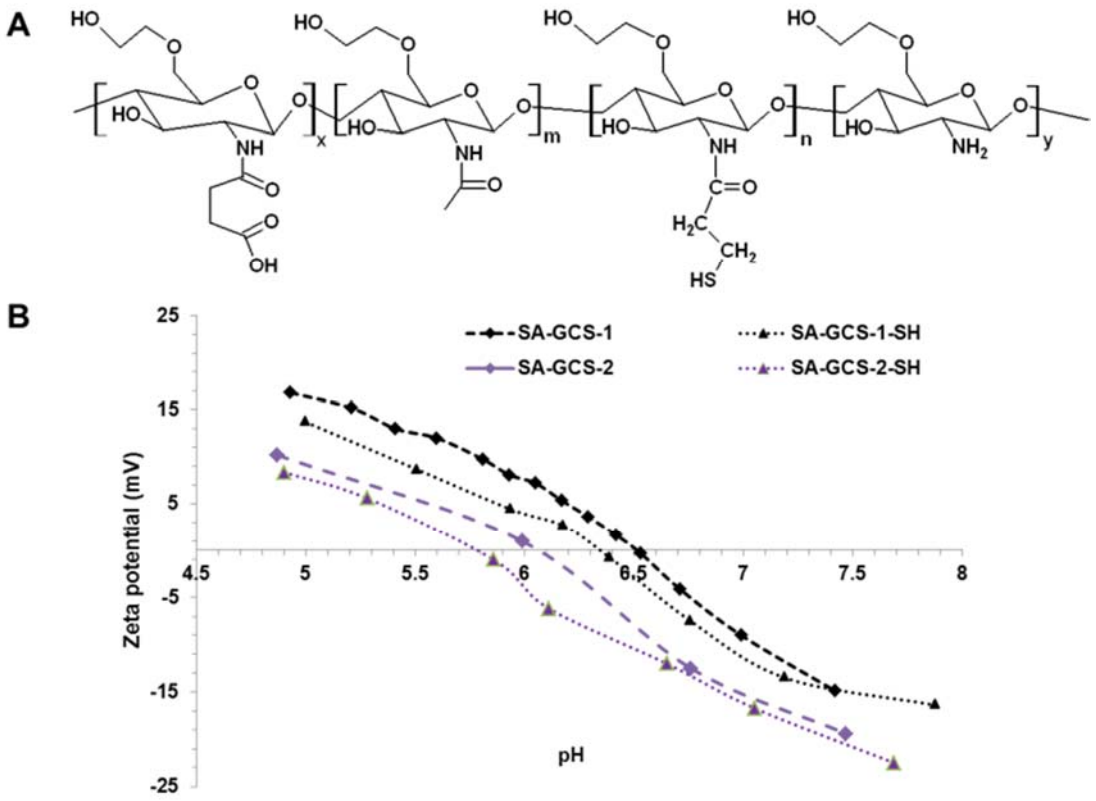

Figure 1.4 IEP measurement of polymers. (A) The structure of SA-GCS-SH. (B) The surface charges of SA-GCS and SA-GCS-SH at different pH.

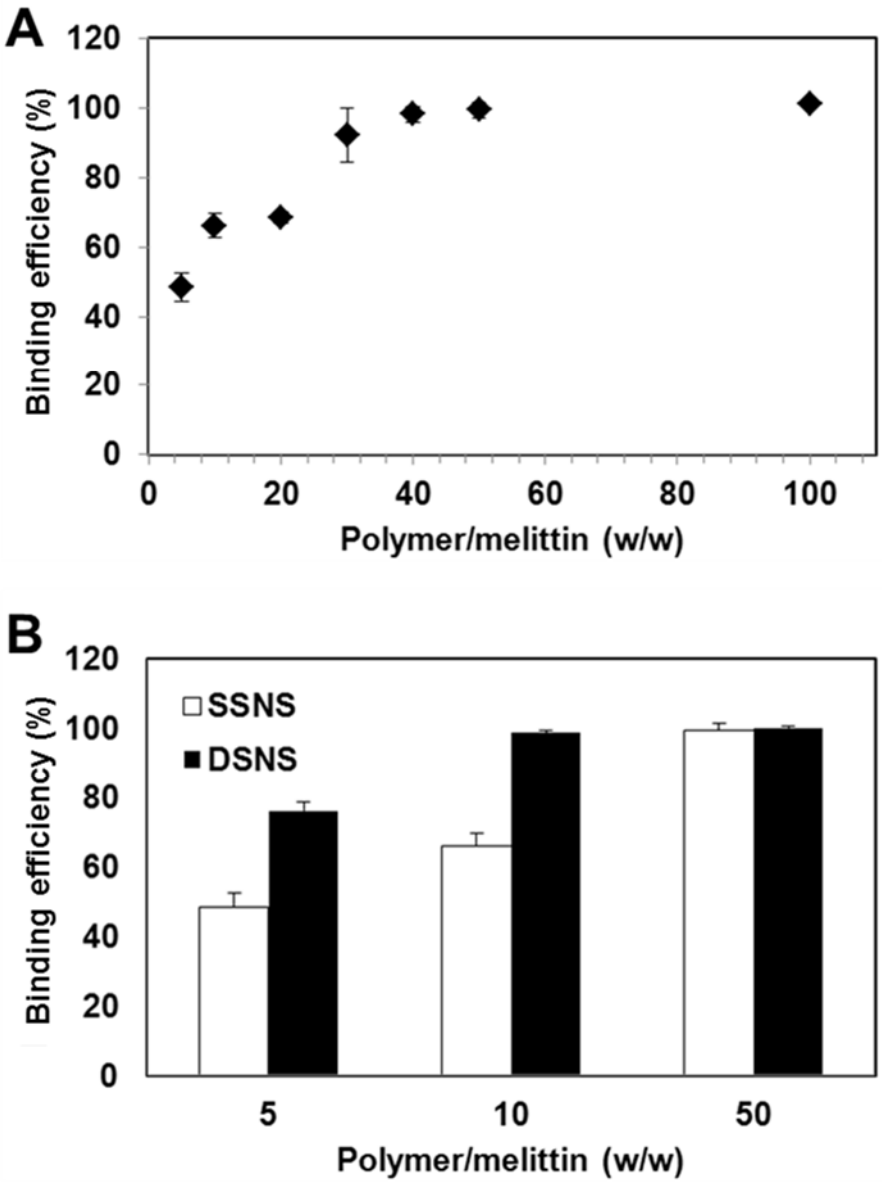

Figure 1.5 Binding efficiency characterization of nano-complexes. (A) Binding efficiency of nano-complex formed at different polymer/melittin (w/w) ratios. (B) Binding efficiency of SSNS and DSNS at different polymer/melittin (w/w) ratios. Data represents mean ± SD, n=3.

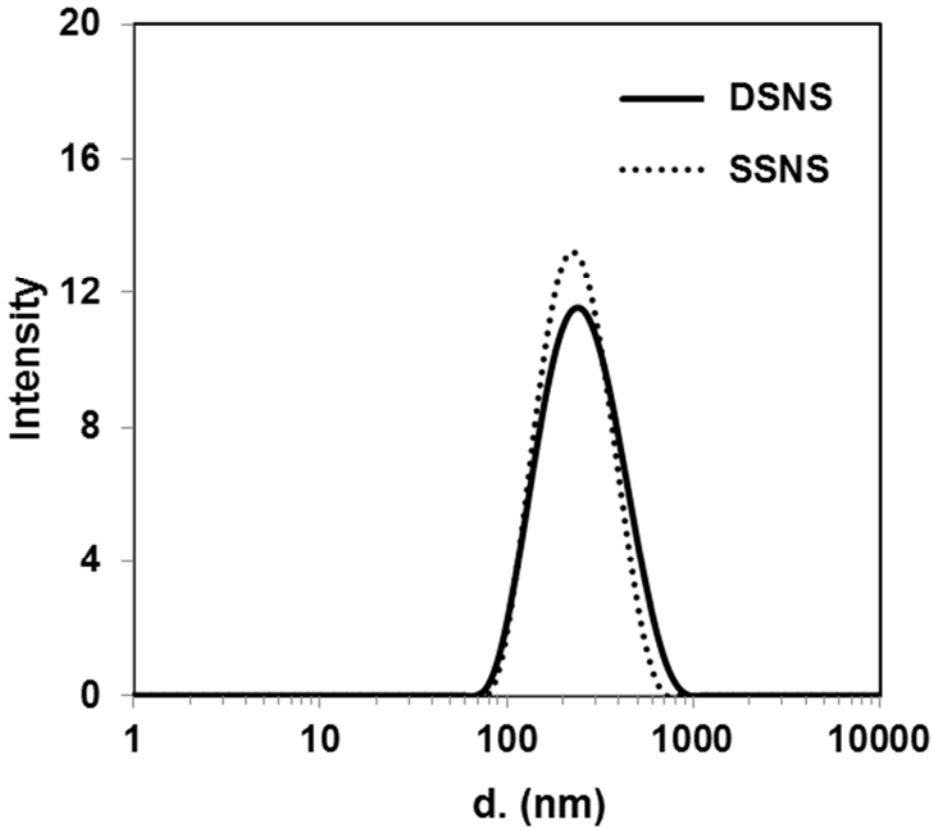

Figure 1.6 The size distribution of SSNS and DSNS determined by dynamic light scattering.

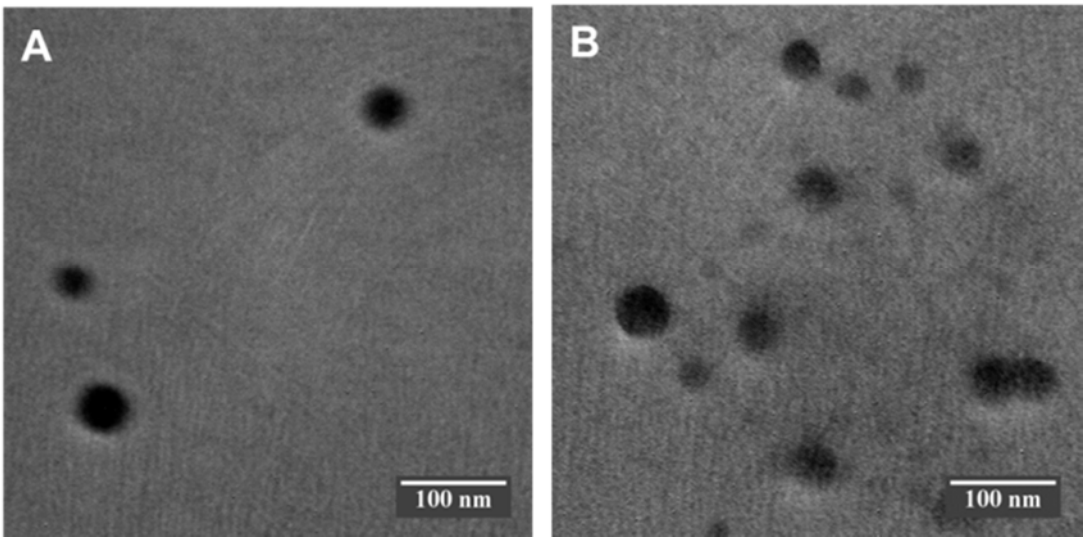

Figure 1.7 Transmission electron microscopy images. (A) SSNS and (B) DSNS. Scale bars are 100 nm.

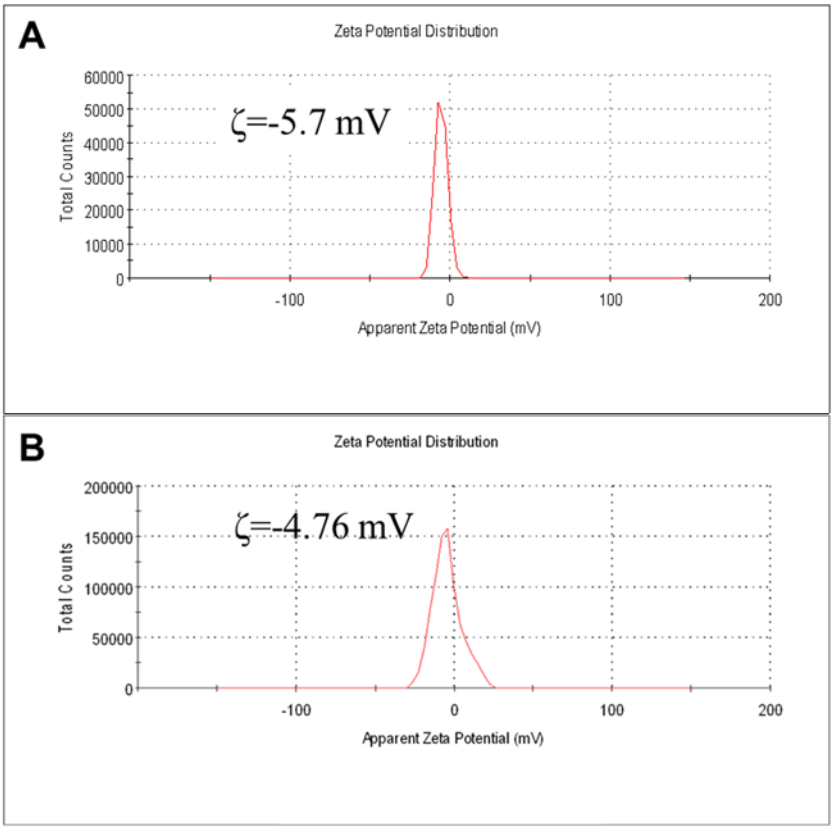

Figure 1.8 The surface charge of complex was determined by phase analysis light scattering. (A) SSNS and (B) DSNS.

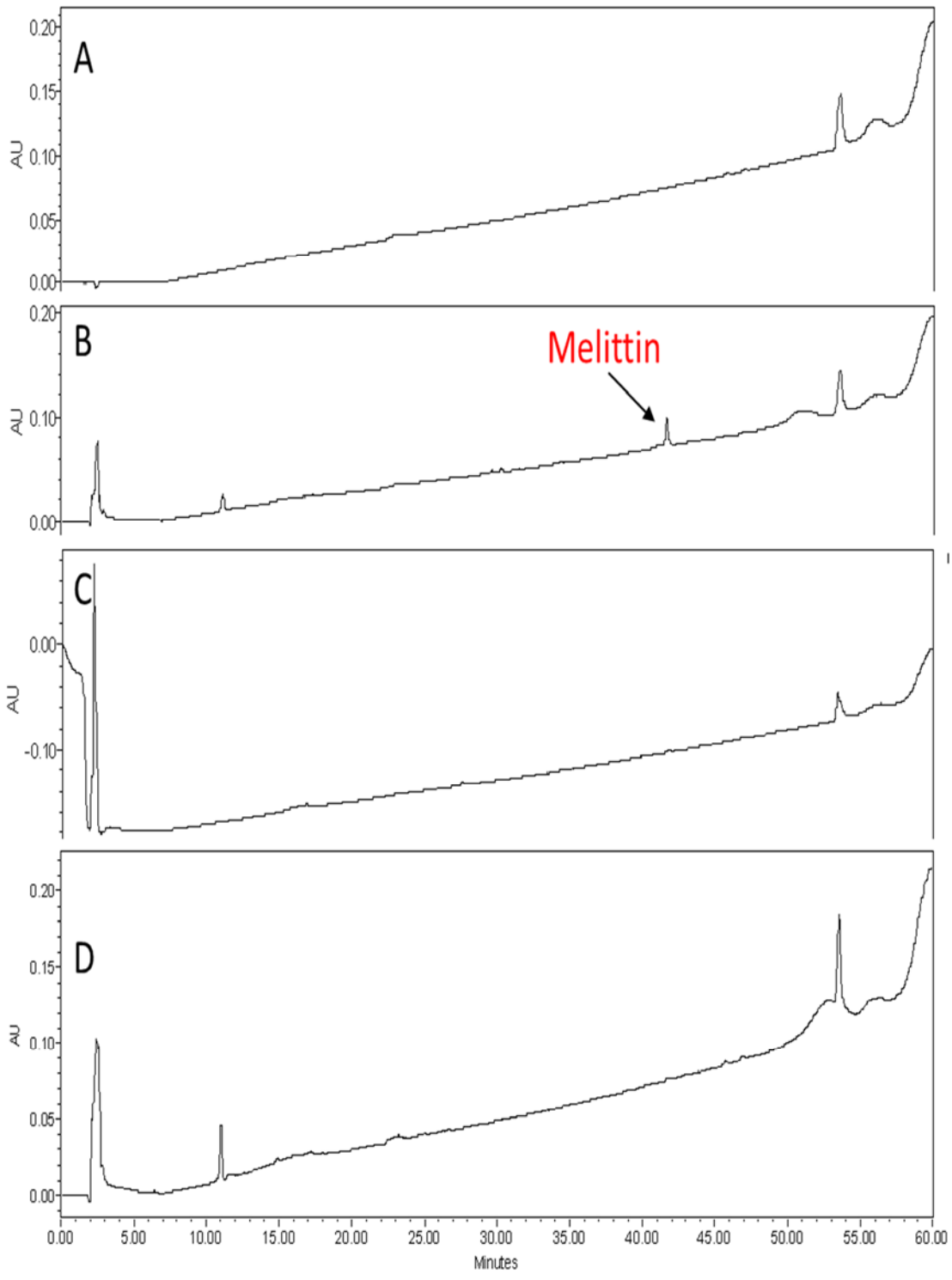

Figure 1.9 HPLC spectra of SSNS and DSNS for the detection of free melittin in the nano-complexes. (A) Solvent, (B) free melittin, (C) SSNS, and (D) DSNS.

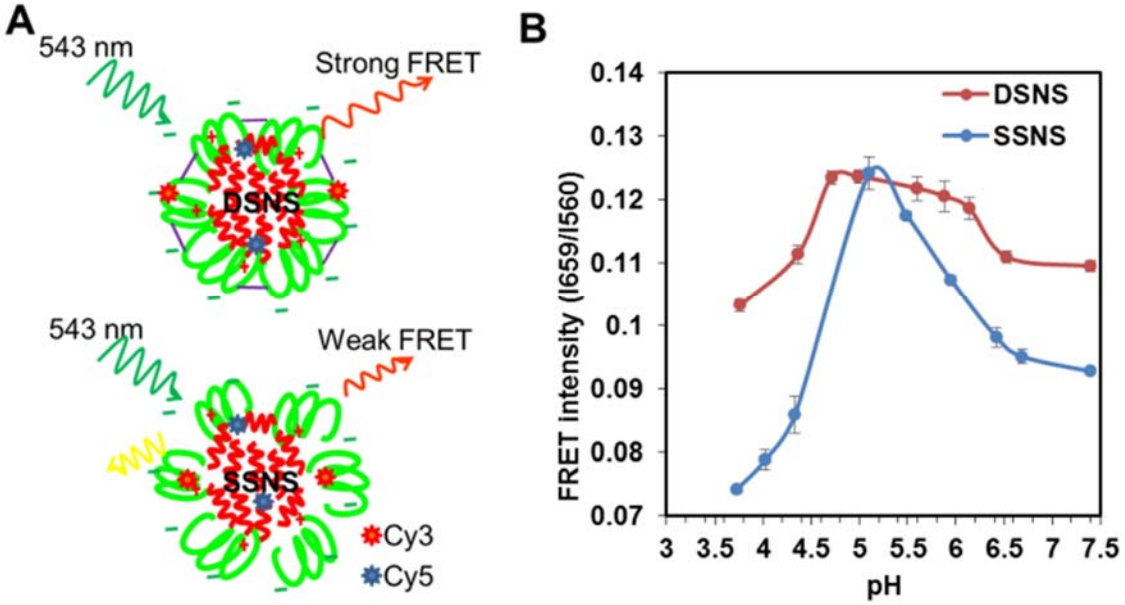

Figure 1.10 The FRET produced by DSNS. (A) The schematic of FRET produced by DSNS and SSNS. (B) The measured FRET intensities of DSNS and SSNS at different pH.

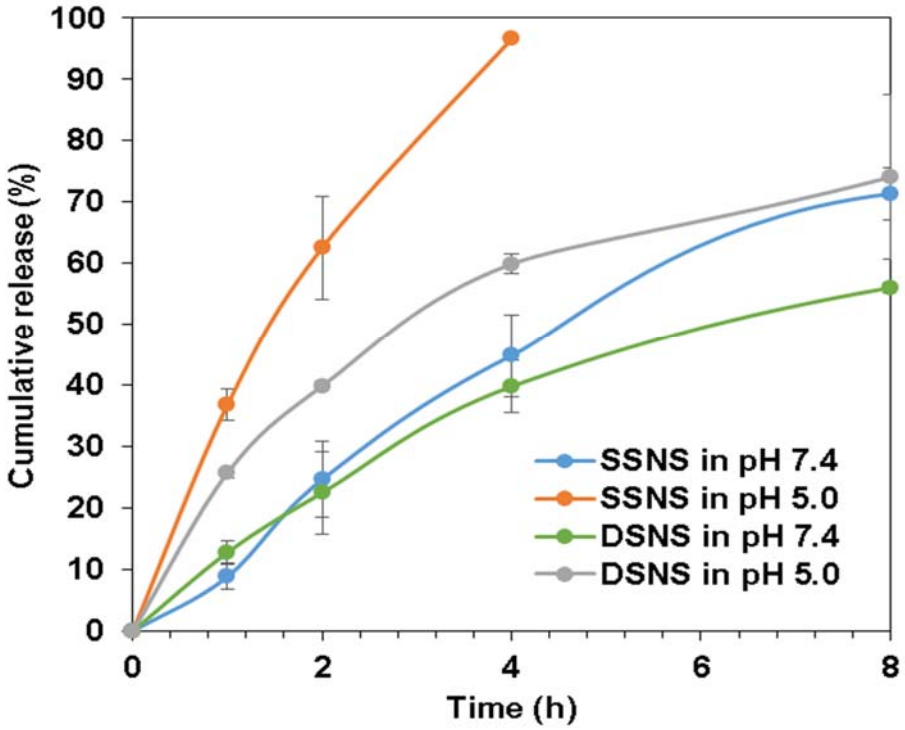

Figure 1.11 The release kinetics of SSNS and DSNS at pH 7.4 and 5.0 buffers.

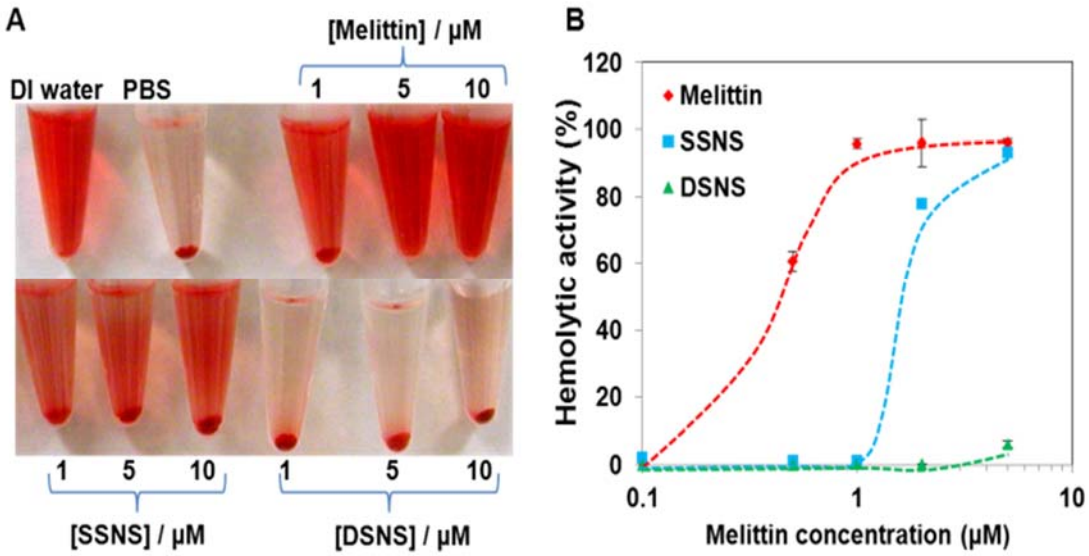

Figure 1.12 Hemolytic assay after incubation of melittin, SSNS, and DSNS with RBCs. (A) Images of RBCs after hemolytic assay. (B) The hemolytic activity of melittin, SSNS, and DSNS.

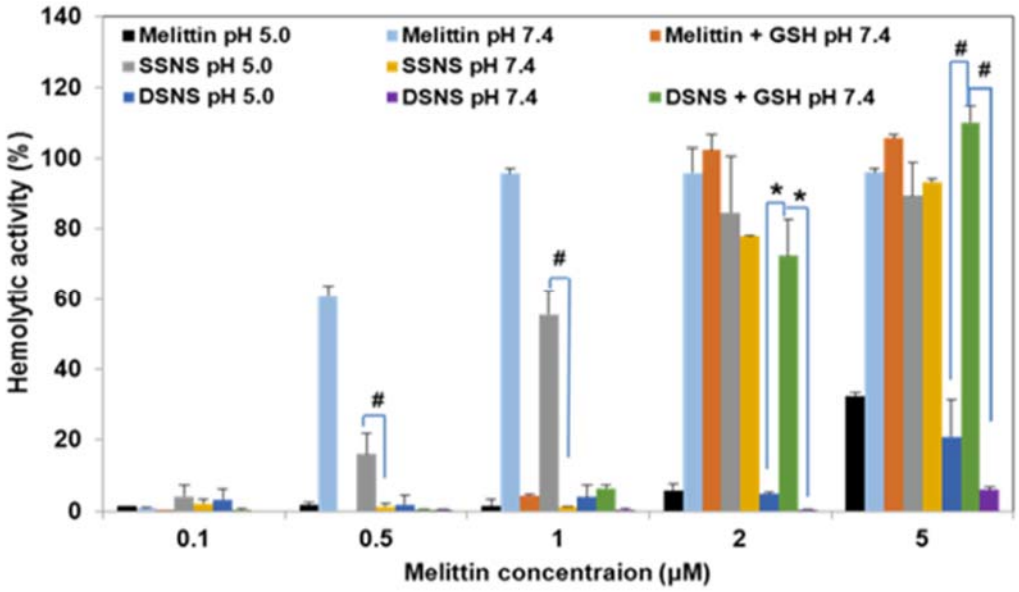

Figure 1.13 Hemolytic activity of melittin, SSNS, and DSNS at different pH and redox potential conditions. * $p < 0.05$ and # $p < 0.01$ (unpaired Student's t-test).

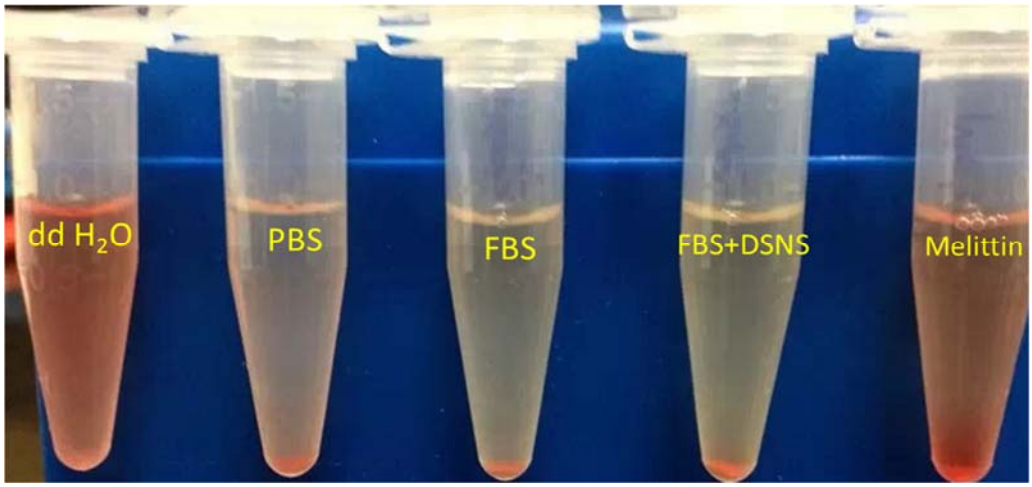

Figure 1.14 The image of RBCs after co-incubating with DSNS in 50% serum containing buffer.

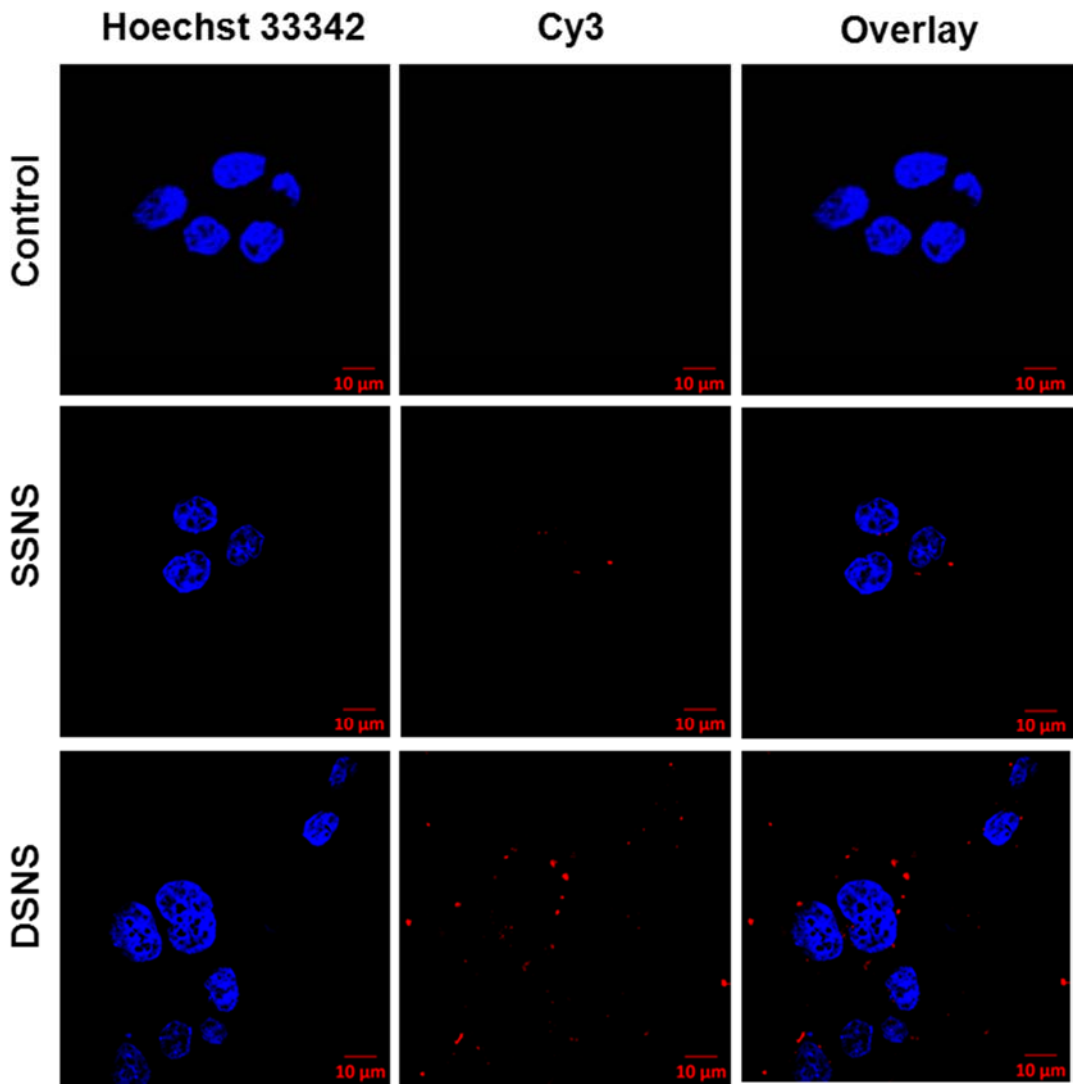

Figure 1.15 Uptake of SSNS and DSNS by confocal microscopy. Confocal microscope images of HCT-116 colon cancer cells after incubation with SSNS and DSNS for 2 h. Scale bars are 10 µm in all images (Blue-Hoechst, Red-Cy3 labeled SSNS or DSNS).

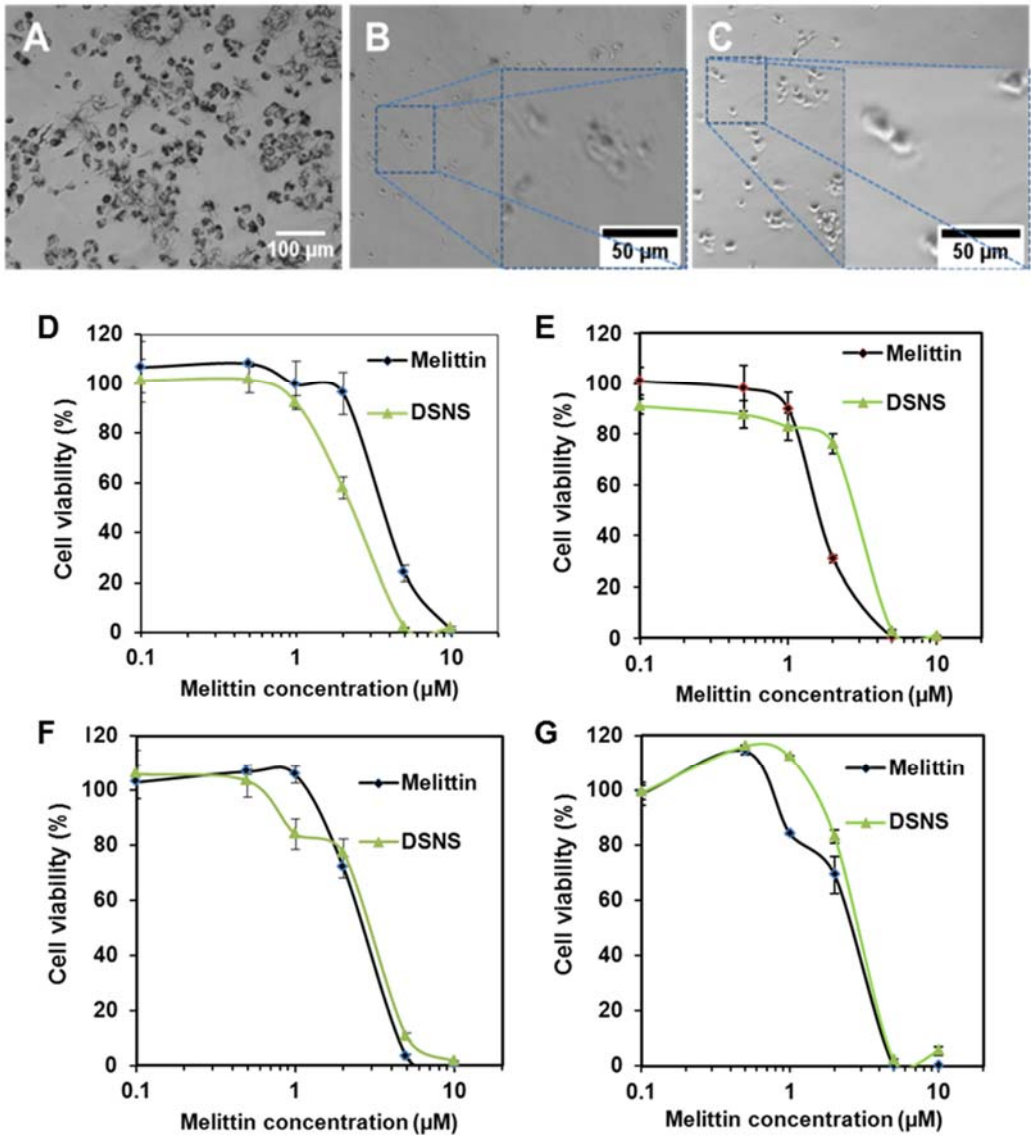

Figure 1.16 Cytotoxicity evaluation of DSNS. The light microscopy images of the morphologies of NCI/ADR-RES cells treated with 5 μM melittin. (A) Control, (B) free melittin, (C) DSNS. (D-G) Cytotoxicity of DSNS and melittin treatments in different cancer cell lines. (D) HCT-116, (E) MCF-7, (F) SKOV-3, (G) NCI-ADR/RES.

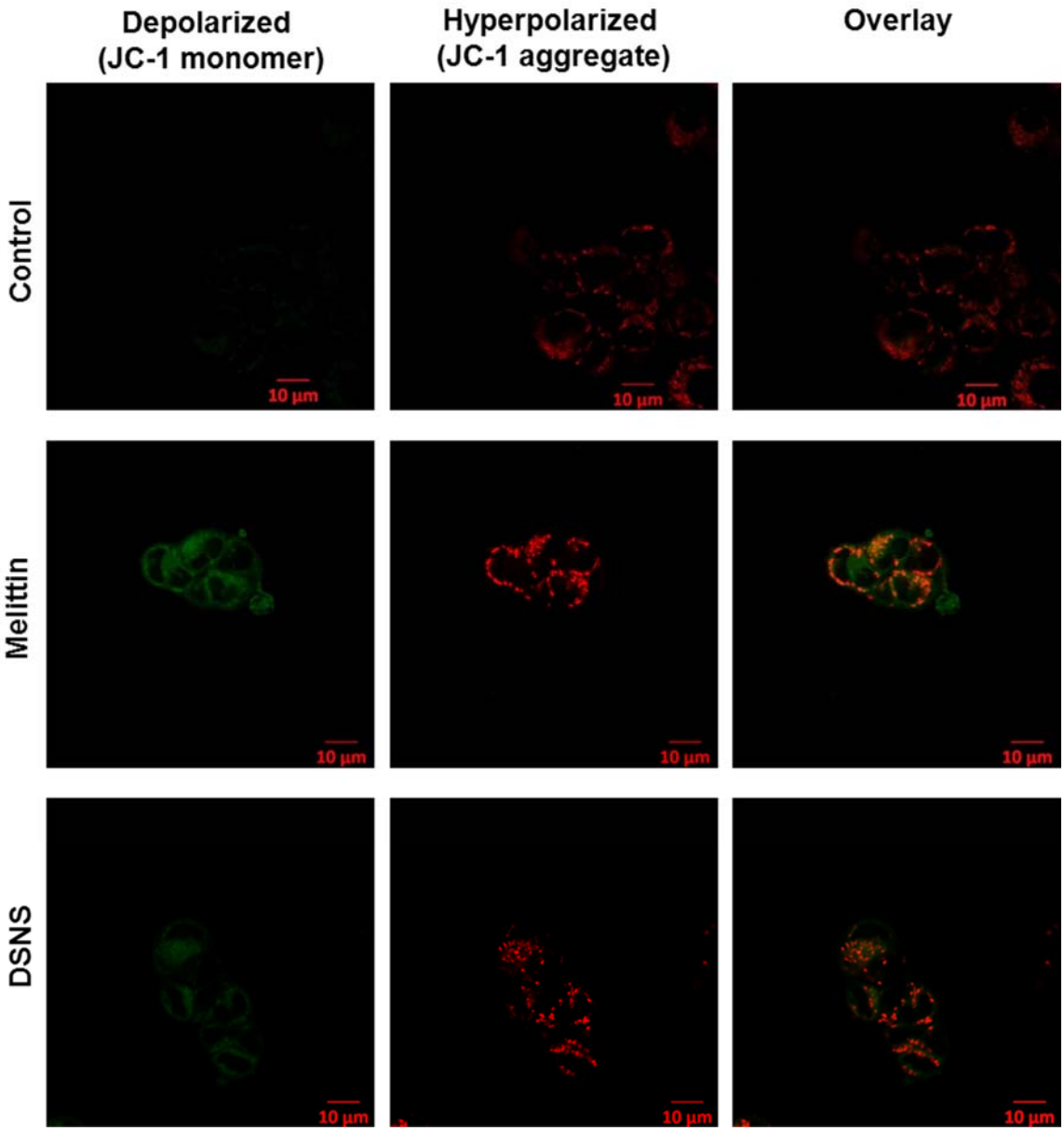

Figure 1.17 Mitochondrial membrane potential changed with the incubation with melittin and DSNS. Confocal microscope images of HCT-116 colon cancer cells after incubation with melittin and DSNS for 1 h and stained with JC-1. Scale bars are 10 µm in all images. Green fluorescence indicates depolarized membrane potentials (JC-1 monomer form) due to the damaged mitochondria function, and red indicates hyperpolarized membrane potentials (JC-1 aggregation).

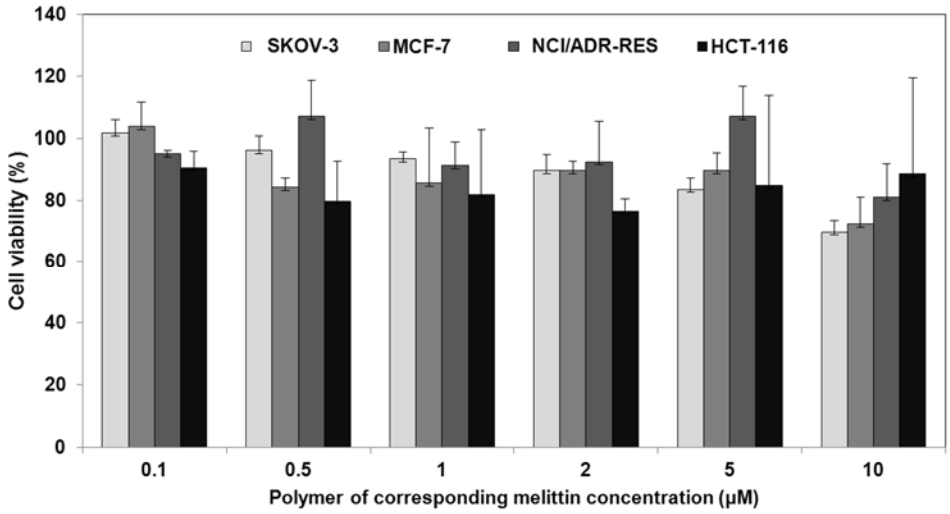

Figure 1.18 Cytotoxicity of SA-GCS-SH. Polymers at the corresponding melittin concentration of 0.1 to 10 μM were tested in SKOV-3, MCF-7, NCI/ADR-RES, and HCT-116 cancer cells.

CHAPTER 2

Gold nanosphere gated mesoporous silica nanoparticle responsive to NIR light and redox potential as a theranostic platform for cancer therapy [2]

ABSTRACT

A gold/mesoporous silica hybrid nanoparticle (GoMe), which possesses the best of both conventional gold nanoparticles and mesoporous silica nanoparticles, such as excellent photothermal converting ability as well as high drug loading capacity and triggerable drug release, has been developed. In contrast to gold nanorod and other heat generating gold nanoparticles, GoMe is photothermal stable and can be repetitively activated through NIR irradiation. Doxorubicin loaded GoMe (DOX@GoMe) is sensitive to both NIR irradiation and intracellularly elevated redox potential. DOX@GoMe coupled with NIR irradiation exhibits a synergistic effect of photothermal therapy and chemotherapy in killing cancer cells. Furthermore, ^{64}Cu-labeled GoMe can successfully detect the existence of clinically relevant spontaneous lung tumors in a urethane-induced lung cancer mouse model through PET imaging. Altogether, GoMe can be utilized as an effective theranostic platform for cancer therapy

[2]Cheng, B., He, H., Huang, T., Berr, S., He, J., Fan D., Zhang, J., and Xu, P.* 2016. Journal of Biomedical Nanotechnology. 12, 435-449.
Reprinted here with permission of publisher.

INTRODUCTION

Gold nanoparticles, including gold nanosphere (GNS), gold nanorod (GNR), gold nanoshell (GNSH), and gold nanocage (GNC), have attracted tremendous attentions during the past decade and have been extensively explored in biomedical applications, such as drug and gene delivery, disease detection, treatment, and response monitoring, due to their excellent biocompatibility, and easy surface modification.[33] Upon irradiation, gold nanoparticles generate heat attributable to the localized surface plasmon resonance (LSPR) phenomenon.[34] By manipulating their shape, size, and geometry, the LSPR peak of GNR, GNSH, and GNC can be tuned to near-infrared (NIR) region, also called tissue transparent window (650-900 nm), within which light can penetrate deeply.[35] Because of that, upon NIR irradiation, these gold nanoparticles generate heat and can be applied for photothermal therapy.[34a, 36] Although gold nanoparticles have been evaluated in numerous systems and proven to be promising in photothermal therapy and drug delivery, there are several intrinsic properties limiting their translation from bench to clinical practice. First, due to their poor photothermal stability, traditional gold nanoparticles gradually lose their photothermal converting capacity upon repetitive NIR irradiation. It has been well documented that the shape and extinction of GNR changed after NIR laser irradiation and resulted in lower heat generating capacity after each heating/cooling cycle.[37] Similar scenarios also have been observed in GNSH and GNC if the generated heat could not be dissipated to their surrounding environment.[38] In addition, except GNCs, other

gold nanoparticles are not good drug carriers either due to limited drug loading capacity or poorly controlled drug release profile.[39] Furthermore, although tremendous efforts have been devoted, how to effectively integrate both photothermal therapy and chemotherapy modules into one system remains a challenge, especially when repetitive activation is needed.

Similar as gold nanoparticles, last decade also witnessed increasing attention gained by mesoporous silica nanoparticle (MSN) due to its high and versatile drug loading capacity as well as good biocompatibility. Numerous MSN based carrier systems have been developed for the delivery of drugs, peptides, DNAs, and siRNAs. To better control the release kinetics of their payloads, many gatekeepers have been explored, such as polyelectrolytes,[40] macrocyclic organic molecules,[41] and inorganic nanoparticles.[42] Generally, these MSN delivery systems are responsive only to the changes in the physiological environment, such as pH and redox potential. Once the MSN is administrated *in vivo*, the drug release profile will be out of the control of the clinician and be totally relying on its fabrication method and biodistribution. To overcome the limitations of existing gold nanoparticles and MSNs in photothermal therapy and drug delivery, we developed a gold/mesoporous silica hybrid nanoparticle (GoMe) by conjugating gold nanospheres (GNS) onto the surface of MSN (**Figure 2.1A**) to take advantage of the best of both worlds.

RESULTS

Gold/mesoporous silica hybrid nanoparticle (GoMe) fabrication

Thiolated MSN was fabricated by the co-condensation of (3-mercaptopropyl) trimethoxysilane (MPTMS) with tetraethyl orthosilicate (TEOS). With CTAB and F127 applied as structure directing agents, these silica sources were able to be constantly hydrolyzed. After the nanoparticle grew to a certain size, the template of CTAB was removed by ion exchange with ammonia nitrate. TEM revealed that most MSNs are in spherical or oval shape with a size of 50.87 ± 10.69 nm (**Figure 2.1B**). The N_2 sorption measurement revealed that the pore size of MSN is about 2-3 nm (**Figure 2.2**), with a surface area of 858 m^2/g. The accessible thiol groups on the MSN were quantified with Ellman's reagent using cysteine as a reference standard. The amount of thiol groups in MSNs was 31 μmol/g. The super stable gold nanosphere (GNS) was synthesized according to literature with minor modification.[43] Thiolated polyethylene glycol (PEG-SH, Mw=2000 Da) was added into the gold isopropanol alcohol solution before the formation of GNS. The resulting PEG-GNS was spherical with a diameter of 3.93 ± 0.70 nm (**Figure 2.1C**). The resulting PEG-GNS was further functionalized through a two-step procedure by conjugating PEG-GNS with cysteamine first, followed by reacting with homemade 2-(pyridin-2-yldisulfanyl)ethyl acrylate (PDA) via Michael addition reaction to yield PDA-GNS as shown in **Figure 2.1A**. DTNB assay revealed that about 200 PDA molecules were anchored to each GNS. PDA-GNS was grafted onto MSN through thiol-disulfide exchange reaction (**Figure 2.1A**) by simply mixing PDA-GNS and thiolated MSN in DI water for 24 h. TEM was employed to

investigate the assembly between GNSs and MSNs. **Figure 2.1C** showed that most GNSs were evenly attached to the surface of MSNs. This gold nanosphere/mesoporous silica nanoparticle hybrid assembly was named as GoMe. To our surprise, only a few free GNSs were detected after the reaction, indicating the high efficiency of the conjugation reaction. The success of grafting of GNS onto MSN was further confirmed by SEM image and SEM/EDX analysis. The evenly distributed small spherical dots on the bigger balls (**Figure 2.3**) and the presence of gold element (**Figure 2.4 and 2.5**) indicated that GoMe had a structure as shown in **Figure 2.1A**. Zetasizer found that GoMe carried slightly negative surface charge (-5.92 ± 0.75 mV, **Figure 2.6**). Due to the existence of PEG outer layer, GoMe was stable in culture medium containing 10% FBS (**Figure 2.7**), and no obvious size change and aggregation were observed after two months of incubation. The size of GoMe determined by dynamic light scattering (DLS, 141.7 nm) was larger than that observed by TEM (54.71 ± 9.63 nm), which is because that TEM measures physical size of the dried particles while DLS measures their hydrodynamic diameter (including the water layer surrounding the particle).

Photothermal property characterization

To monitor the fabrication progress of GoMe, UV-Vis spectrophotometer was employed by recording the absorbance from 400 to 1000 nm during the reaction. **Figure 2.8A** showed that the absorbance peak of the reaction mixture at 524 nm decreased over time and slightly shifted to long wavelength direction, while its absorbance in the NIR region gradually increased. To evaluate the

photothermal properties of the reaction mixture changing with the progress of the reaction, the reaction suspension was irradiated with NIR laser (808 nm, 2.83 W/cm^2) for 10 min at predesigned time intervals and its temperature was monitored with a FLIR i7 thermal imaging camera and recorded every 30 sec. Before the mixing, the aqueous nano-suspension of MSN produced none while GNS produced little heat under the NIR irradiation (**Figure 2.8B**). To our surprise, after 12 h of reaction, the temperature of the mixture of MSN and GNS raised 21.2 °C after irradiation (**Figure 2.8B**). Furthermore, the longer the reaction time, the higher the temperature reached. The mixture after 24 h of reaction could be heated to 52.8 °C (30 °C increase) upon the same intensity and length of NIR irradiation. The photothermal conversion efficiency of GoMe was 29.65%, which is slightly higher than the reported GNSH (25%) while lower than GNR (50%).[44]

To probe the mechanism for the mixture of GNS and MSN generating heat upon NIR laser irradiation, TEM was employed to observe the morphology change during the reaction. The reaction mixture was centrifuged to remove unconjugated GNS before loaded onto copper grids for TEM observation. **Figure 2.8C** showed that GNSs can be conjugated onto MSN within 2 h. Longer reaction time resulted in a higher GNS decorating density on the surface of MSN (**Figure 2.8D and 2.8E**). Altogether, higher decorating density of GNS on GoMe led to a higher absorbance in the NIR region, which opened the window for the biomedical application of GoMe using a NIR laser (**Figure 2.8A**). As a consequence, GoMe with higher GNS decorating density produced more heat

upon the NIR laser irradiation (**Figure 2.8B**). **Figure 2.9** revealed that GoMe exhibited a concentration-dependent photothermal heating effect. Therefore, a desired photothermal heating curve can be achieved by simply tuning the concentration of GoMe. Photothermal stability is a vital property for the success of photothermal therapy, especially when repetitive treatment is necessary for the management of recurrent cancer. To evaluate the photothermal stability of GoMe, aqueous suspension of GoMe was repetitively irradiated with the 808 nm NIR laser (10 min on and 20 min off) at the light intensity of 2.83 W/cm^2. The temperature of the nano-suspension was monitored as described above. GNR (aspect ratio of 3.89 and peak absorbance of 804 nm) synthesized according to literature was employed as a control.[45] GNR at a concentration that could produce heat to reach similar temperature as that of GoMe was irradiated in parallel. **Figure 2.10** showed that the temperature of both GoMe and GNR suspensions increased rapidly upon laser irradiation and reached 74 °C in 10 min. As expected, the repetitive heating of GNR suspension resulted in decreased peak temperatures, declined from 74 to 65.8 °C during the second heating cycle and further dropped to 48.5 °C after 6 cycles of laser irradiation induced heating/cooling. In an apparent advancement to the field, GoMe suspension could reach the same peak temperature after 6 heating/cooling cycles, and achieved even higher peak temperature after 24 h of resting period, which suggests that GoMe was stable in keeping its photothermal property during laser irradiation induced heating/cooling process. Such stability is critical for certain biomedical applications which require multiple laser irradiations. Since

GNSs were grafted onto MSN through disulfide bonds, the photothermal property of GoMe in reducing environment was further investigated. **Figure 2.11** showed that GoMe only slightly decreased its peak temperature in an environment containing 10 mM GSH, suggesting that most of GNSs were still attached to MSN. As we have confirmed that each GNS had 200 thiol reactive PDA groups, it is reasonable to postulate that every GNS was connected with MSN through multiple disulfide bonds. Therefore, at any given time, GSH only cleaved partial of those disulfide bonds for each GNS and loosened the binding between GNS and MSN. More importantly, repetitive heating/cooling in reducing environment did not change its photothermal converting capacity (**Figure 2.11**). Therefore, GoMe would retain its competence in generating heat upon NIR irradiation in an intracellular environment, where it has high GSH level.[46]

To probe why GoMe was stable during the NIR laser irradiation induced heating/cooling cycles, while GNR was instable, the UV-Vis spectra of GoMe and GNR after each cycle were recorded. The UV-Vis absorbance of GoMe only marginally changed after 6 cycles of heating/cooling (**Figure 2.12A**), while the absorbance of GNR significantly diminished in the NIR region (**Figure 2.12B**). To investigate the morphologies of the GNR and GoMe after above treatment, TEM was employed. **Figure 2.12D** proved that the morphology of GoMe remained intact after laser irradiation. By contrast, some GNRs changed their shape significantly after 5 cycles of laser irradiation, becoming shorter and fatter or round (**Figure 2.12F**). This rod-to-sphere shape transformation was due to the melting of GNR under the extensive heat itself generated.[47] Since gold

nanoparticles melt at high temperature and form gold nano-droplet (or so called nanosphere), similar shape transformations also have be documented for gold nanoshells and gold nanocages.[38c] As a consequence of losing their original geometries, these gold nanoparticles showed a compromised photothermal property. However, GoMe, which was fabricated from GNS and MSN, kept its shape unchanged, since GNS remained its original spherical after melting. Therefore, GoMe kept its photothermal capacity intact over multiple heating/cooling cycles.

Drug release kinetics measurement

To investigate whether the decoration of GNS on the surface of MSN could affect the release profile of its payload, anticancer drug doxorubicin (DOX) was adopted as a model drug and loaded into MSN as described by literature.[33] Due to its high surface area and pore volume, GoMe achieved 28% drug loaded content. Because DOX is a potent anticancer drug, DOX loaded GoMe (DOX@GoMe) of 4.58% drug loading content was adopted for the in vitro assay. However, in drug release kinetics study, the DOX@GoMe of 28% drug loading content was employed to achieve a more accurate drug release profile.

An ideal drug carrier should be premature-release free before reaching its target. Furthermore, for a desired delivery system, the release of its payload should be either spontaneously responsive to the stimuli from its target or remotely controlled by external signals. To investigate the release kinetics of DOX from GoMe, DOX@GoMe was suspended in phosphate buffer (PBS, pH 7.4) and PBS supplemented with 10 mM GSH to mimic the environments in the

circulating blood and cytosol, respectively. Researchers found that surface non-modified MSN can easily aggregate in aqueous medium,[48] which could result in false release profile. For fair comparison, DOX loaded MSN (DOX@MSN) was also stabilized though PEG-SH surface modification. Figure 2.5A showed that DOX@MSN released more than 28.8% of its payload within 10 h of incubation in PBS, suggesting that unsealed MSN was not a desired carrier. Interestingly, GoMe, MSN decorated with GNS, released much less of DOX (8.3%) within the same period of time, indicating that GNS could serve as a plug to prevent DOX from leaking out from the pores of MSN during circulating in blood stream. Since GNS was conjugated onto the surface of MSN through disulfide bonds, we further investigated the responsiveness of GoMe to reducing environment by dispersing it in PBS supplemented with 10 mM GSH. As expected, GoMe released much more DOX in reducing environment (66.4% of DOX within 24 h) than that in PBS (10.3%), demonstrating that GoMe was a good carrier for intracellular drug delivery. As we already proved that GoMe could efficiently convert NIR laser irradiation into heat, we further investigated the effect of NIR irradiation on drug release by applying irradiation (10 min laser on in every 24 h period) on the GoMe nano-suspension. Remarkably, **Figure 2.13B** showed that 10 min of NIR irradiation induced more than 23% immediate DOX release. The removal of laser irradiation promptly slowed down the drug release. Moreover, the re-introducing of laser irradiation could accelerate drug release repetitively. The first time NIR irradiation triggered more drug release than the later ones, which possibly due to the liberation of drugs bonded on the surface MSN for the

first irradiation while later stimuli induced the release of encapsulated drugs from the pores of MSN. This light activable two-stage drug release pattern can be utilized to meet the clinical setting in drug administration by providing both loading dose and maintenance dose.

Observation of GoMe by confocal fluorescent and dark-field microscopies

To explore the potential of using GoMe as a carrier to deliver drug into cancer cells, DOX-loaded GoMe was co-incubated with A2058 melanoma cells for 3 h, and then observed with a confocal microscope. The red fluorescence signals in **Figure 2.14F** proved that GoMe loaded DOX could effectively enter A2058 cells. To further confirm that GoMe entered cancer cells, the above cells were also observed with a dark-field microscope. Scatter light signals (yellow and red dots) collected inside A2058 cells (**Figure 2.14J**) through a dark-field detector proved that GoMe could be taken up by cancer cells.

Cell killing effect of GoMe

Figure 2.15 displayed that GoMe raised medium temperature from 21.8 to 34.6 and 50.3 °C within 10 min of laser irradiation at GoMe concentrations corresponding to 1.67 and 5 μM DOX, respectively. Since GoMe could generate heat and raise medium temperature upon NIR laser irradiation, we first investigated its photothermal therapy effect on the cancer cells through Live/Dead cell assay. A 2058 cells were co-incubated with blank GoMe at the corresponding Dox concentration of 5 μM and coupled with NIR laser irradiated for 10 min before the Live/Dead cell assay, and then visualized with a fluorescent microscope. As expected, nearly all non-treated cells were stretched and green

(**Figure 2.16A**). It was also noted that blank GoMe treated cells (**Figure 2.16B**) did not show any morphology difference as compared with the non-treated ones, suggesting GoMe itself was not toxic. By contrast, cells treated with blank GoMe and laser irradiation dramatically changed their morphology, showing round shape (**Figure 2.16C**). It was also noticed that the cell density in Figure 2.6C was much lower than the group without receiving laser irradiation, which was due to the detaching of cells as a result of apoptosis and subsequently being removed during the washing procedure. In addition, a significant portion of cells in **Figure 2.16C** were stained in red, confirming that GoMe coupled with NIR irradiation could effectively kill cancer cells.

We have confirmed that NIR laser irradiation could trigger the release of DOX from GoMe, and also proved that photothermal effect of blank GoMe could kill cancer cells. To investigate the cell killing efficacy of DOX@GoMe coupled with NIR irradiation, A 2058 cells receiving different treatments were analyzed by MTT assay. Due to the potential residual of cetyl trimethylammonium bromide (CTAB) in the MSN, blank GoMe showed some cytotoxicity. As expected, the application of NIR irradiation enhanced the cell killing effect of GoMe (**Figure 2.16D**), especially for GoMe at the concentration of 5 μM. Because the capping effect of GNS and consequent slower drug release, DOX@GoMe was less potent than DOX@MSN in killing cancer cells. Furthermore, **Figure 2.16D** also evidenced that the DOX@GoMe coupled with NIR irradiation did show superior anticancer efficacy than either GoMe coupled with NIR irradiation or DOX@GoMe alone. Due to the photothermal effect of GoMe, NIR irradiation of

DOX@GoMe could kill cancer cells by the combination effect of photothermal ablation and boosted drug release and subsequent enhanced chemotherapy. It is worth noting that the effect of NIR irradiation only became significant when GoMe concentration reached 2 μM, at which GoMe could generate enough heat to ablate cancer cells and augment drug release. The combination index (CI) analysis further revealed that the combination of DOX@GoMe and NIR irradiation exhibited synergistic effect at the DOX concentration 5 μM (CI value = 0.50).[49] Therefore, to warrant the synergistic effect between DOX@GoMe and NIR irradiation, high retention of DOX@GoMe in the targeted tissue or cells is required.

In vivo tumor detection

To endow the PET imaging function to GoMe, DOTA was conjugated onto GoMe nanoparticles by adding maleimido-mono-amide-DOTA. With the help of conjugated DOTA, the yield for GoMe 64Cu-labeling was above 98%, which suggests that GoMe is a good carrier for radiopharmaceuticals. To validate that ^{64}Cu-labeled GoMe can be used as a tool for cancer detection, a clinically relevant spontaneous lung tumor model was employed. The 3 small tumors in the lung (previously revealed by a ClinScan MRI system as shown in **Figure 2.17A**) were clearly detected by PET at both 6 h (**Figure 2.17B and C**) and 20 h (**Figure 2.17D**) post-administration, suggesting the high retention of GoMe in the tumor, which proved that GoMe is good tool for the cancer detection. Similar as other nanoparticles, significant amount of GoMe nanoparticles accumulated in liver and spleen as shown in the PET images. The increase of PET signals in the

abdomen (colon and rectum) from 6 h to 20 h revealed the rout for GoMe to be cleared from the body.

DISCUSSION

Various gold/silica hybrid nanoparticles have been explored as tools for bioimaging and drug carrier. Lee et al. revealed that α-synuclein-coated gold nanoparticle decorated MSN could release its payloads upon the intracellular Ca^{2+} stimulus.[50] Aznar et al. developed a gold/MSN hybrid system through the formation of boronate esters. Due to the hydrolysis of boroester bonds at acidic pH and light induced heat, low pH and light can be used to trigger the release of its cargo.[42a] In addition, Sharma et al. also found that gold nanoparticle coated silica nanoparticles could produce strong signals for magnetic resonance imaging (MRI) and photoacoustic tomography (PAT).[51] In our design, gold nanospheres were grafted onto the surface of MSN through disulfide bonds, which endowed the intracellular redox potential responsiveness to GoMe. The surface-assembled GNS can be considered as a structure well-defined assembly of “chainlike gold nanoparticles”,[52] or a discontinuous form of gold nanoshell, both of them can efficiently generate heat upon NIR irradiation. In contrast to its continuous counterpart, GoMe kept its original shape after NIR irradiation due to the distance between each GNS and the support of MSN. Consequently, GoMe exhibited stable photothermal property. Because the release kinetics of GoMe is super sensitive to the NIR irradiation, DOX@GoMe showed synergistic effect in killing cancer cell upon NIR irradiation. Since the first *in vitro* report of mesoporous silica-coated gold nanorod reported by Zhang et al.,[53] several recent studies

explored its application for tumor growth inhibition in vivo.[54] However, none of them have been utilized for cancer detection. Due to the abundance of PDA segments on the GNS, GoMe could be conveniently modified with DOTA and achieved excellent chelating capacity needed for PET imaging. To the best of our knowledge, GoMe is the first gold/mesoporous silica hybrid nano-system which is capable of both detecting clinically relevant spontaneous tumor and achieving the synergetic effect of photothermal therapy and chemotherapy in killing cancer cells. To further enhance the sensitivity of its cancer detection capacity and boost its anticancer efficacy, the next step research will incorporate tumor targeting ligands, such as RGD peptide, folic acid, and anisamide, which target cancer cells overexpressed integrin,[55] folate,[55b, 56] and sigma-2 receptors,[32b, 57] respectively, into GoMe. In summary, a photothermal stable gold/mesoporous silica hybrid nanoparticle (GoMe), which possesses the merits of both conventional gold nanoparticles and mesoporous silica nanoparticles, such as good photothermal converting ability and high drug loading capacity, has been developed. In contrast to other MSN based system, GoMe is well dispersed in serum containing medium. Contrary to GNR and other heat generating gold nanoparticles, GoMe is stable in structure and maintains its photothermal converting capacity after repetitive NIR irradiation. The release of drug from GoMe can be triggered by both intracellularly elevated redox potential and NIR irradiation. The localization of doxorubicin loaded GoMe can be detected by both fluorescence and dark-field microscopies. In addition, the combination of DOX@GoMe and NIR irradiation exhibited synergistic effect at the DOX

concentration 5 μM through the integration of photothermal therapy and chemotherapy. Furthermore, PET imaging proved that GoMe is a good tool for the detection of clinically relevant spontaneous lung tumor. Based on these promising in vitro and in vivo results, further studies will focus on the pharmacokinetics of GoMe and utilizing it as an effective tool for image-guided cancer therapy.

MATERIALS AND METHODS

Materials

Terraethylorthosilicate (TEOS), (3-mercaptopropyl)trimethoxysilan) (MPTMS), hexadecyltrimethyl ammonium bromide (CTAB), sodium hydroxide (NaOH), pluronic® F-127, ammonium nitrate, methanol, gold chloride trihydrate, cysteamine hydrochloride, 2,2'-dipyridyl disulfide, triethylamine (TEA), doxorubicin (DOX), and sodium borohydride ($NaBH_4$) were purchased from Sigma-Aldrich. PEG2000-SH was purchased from Laysan Bio. Ethanol and acetic acid were acquired from Fisher Scientific.

Synthesis of mesoporous silica nanoparticles (MSN)

The MSN was synthesized in a dual surfactant system using a classic fast self-assembling method containing both the cationic surfactant cetyl trimethylammonium bromide (CTAB) and non-ionic surfactant triblock polymer F 127 to obtain a good suspending nano-sized MSN. In a typical synthesis, CTAB (50 mg) and F 127 (40 mg) were dissolved in 24 mL DI water. After that, NaOH aqueous solution (175 μL, 2M) was added into the above mixture. The reactants were heated to 80 °C with vigorous stirring for 30 min. TEOS (200 μL) was added

dropwise to the above solution followed by 3-mercaptopropyl trimethoxysilan (MPTMS, 20 μL). A white precipitant was formed after a few minutes and the mixtures were allowed to stir for 2 h at 80 °C. The crude product was collected by centrifugation at 16,000 rcf for 15 min. CTAB was removed through ion exchange by washing in ethanol solution of NH_4NO_3 at 50 °C. This process was repeated for 3 times, followed by extensively washing with ethanol and the purified product was stored at 4 °C in ethanol solution.

Synthesis of PEG stabilized gold nanosphere (PEG-GNS)

The super-stable gold nanosphere was synthesized according to literature with minor modification.[43] Briefly, gold (III) chloride trihydrate (12 mg) was first dissolved in 18 mL isopropyl alcohol and followed with the addition of 0.2 mL acetic acid. Thiolated polyethylene glycol (PEG-SH, MW=2000 Da) (15.24 mg in 2 mL isopropyl alcohol) was added into the gold alcohol solution. The mixture was stirred for 1 h at room temperature following the addition of sodium borohydride (37.84 mg in 1.5 mL methanol). The reaction mixture was stirred vigorously overnight at room temperature. After overnight reaction, the mixture was centrifuged for 30 min (2500 rcf) to remove large particles. The resulting supernatant was precipitated in hexane. The precipitant was re-dispersed in 5 mL DI water. To remove free PEG-SH from gold nanoparticle, the PEG-GNS was purified by repeatedly washing with water in a Millipore Centricon (MW CO=10,000 Da). The successful anchoring of PEG-SH onto gold nanosphere was confirmed by 1H-NMR (**Figure 2.18A**). The zeta potential of PEG-GNS was measured by Zetasizer Nano ZS (Malvern) and showed a near neutral potential

(-8.65 mV), which further confirmed the successful coating of PEG onto the GNS. The morphology of PEG-GNS was confirmed by TEM. The UV-Vis spectrum of PEG-GNS was recorded by UV-Vis spectrophotometer (DU®650 Spectrophotometer, Beckman Coulter, USA), which showed an absorbance peak at 510 nm.

Synthesis of 2-(pyridin-2-yldisulfanyl)ethyl acrylate modified GNS (PDA-GNS)

PDA-GNS was synthesized in a two-step procedure by conjugating PEG-GNS with cysteamine first, followed by reacting with 2-(pyridin-2-yldisulfanyl)ethyl acrylate (PDA) through Michael addition reaction. Briefly, the PEG-GNS synthesized above was dispersed in 10 mL DI water, and then cysteamine (0.216 mg in 40 μL H_2O) was added. The mixture was kept stirring at room temperature. After 24 h of stirring, the reaction solution was loaded to a Millipore Centricon (MWCO=10,000 Da) and repeatedly washed by centrifugation to remove un-reacted cysteamine. The successful conjugating of cysteamine was confirmed by zeta potential measurement, which showed a highly positive charge (+27 mV) on the GNS surface. The surface amine concentration was further measured by TNBSA assay, which also proved the successful replacement of PEG by cysteamine. The GNS concentration was determined by calculating UV-Vis absorbance. The result showed that there were around 1000 $–NH_2$ groups located on the surface of each GNS. After that, PDA was conjugated to the GNS by reacting with amine groups via Michael addition reaction. Typically, cysteamine modified GNS was dispersed in 500 μL of DMSO, and triethylamine

(0.265 µL in 26.5 µL DMSO) was added, following the addition of PDA (0.459 mg in 50 µL DMSO). The ratio between $–NH_2$ and PDA was optimized at 2:1 since a higher $-NH_2$ to PDA ratio could easily result in GNS aggregation during the post-purification process. The reaction mixture was purged with nitrogen and then kept at 50 °C for 24 h. The resulting PDA-GNS was precipitated in cold ether for three times to remove unreacted PDA and finally re-dispersed in 2 mL DI water. The successful conjugation of PDA was confirmed by UV-Vis spectrum (**Figure 2.18B**). PDA-GNS showed a PDA characteristic peak around 375 nm after reacting with dithiothreitol (DTT). The PDA concentration of PDA-GNS was measured by DTNB assay, which proved that about 200 PDA was anchored to each GNS.

Encapsulation of doxorubicin (DOX) into MSN

To load DOX into MSN, DOX•HCl was firstly converted to its base form by mixing with triethylamine for 30 min. In a typical synthesis batch, 10 mg DOX was added to 18.6 mg MSN and the mixture was sonicated for 30 min to obtain a uniform dispersion. The mixture was stirred at room temperature for 24 h and the unloaded DOX was removed by washing with DI water twice. It was denoted as DOX@MSN. The loading efficiency of DOX was quantified by a fluorospectrometer (Beckman Coulter, DTX 880). Different loading of DOX can be simply tuned by changing the ratio between DOX and MSN. In this experiment, the highest drug loading content of DOX in DOX@MSN reached 28%.

Fabrication of GNS decorated MSN (GoMe)

GNS was grafted onto MSN through thiol-disulfide exchange reaction. MSN (200 µg in 200 µL) aqueous solution was added to 2 mL PDA-GNS aqueous suspension while stirring. The mixture was allowed to react at room temperature for 24 h, and then washed three times with DI water (**Figure 2.1**). The final product was collected by centrifugation. The size and morphology of the GoMe was determined by TEM. Cells were plated onto 12-mm glass coverslips in 24-well plates prior to drug treatment or transfection.

Photothermal stability assay

The repetitive laser irradiation experiments were carried out to test the photothermal stability of GoMe and gold-nanorod, which is critical for multiple photothermal treatments. Firstly, the concentration of GoMe and gold nanorod were adjusted to generate equal increment in temperature upon the same intensity of laser irradiation. The GoMe suspension was irradiated by the 808 nm laser for 10 min (Scorpius D-700 laser, 2.83 W/cm^2). The temperature of the nano-suspension was monitored with a FLIR i7 thermal imaging camera and recorded every 30 sec. Both the GoMe and the GNR (maximum absorbance peak at 804 nm) were undergone 6 continuous laser irradiation cycles (10 min irradiation and 20 min cooling). The 7th irradiation was applied 24 h after the 6th cycle. The UV-vis spectra and TEM images were recorded to reveal the change during the repeating cycles. The photothermal stability of GoMe in reducing environment was further investigated by dispersing GoMe in DI water supplemented with 10 mM GSH.

Laser irradiation triggered release of GoMe

To evaluate the responsiveness of GoMe to NIR light, 20 µL of GoMe containing 4 µg of DOX was diluted with 250 µL DI water. The GoMe suspension was incubated at 37 °C to carry out the release study. GoMe nano-suspension was centrifuged at 1, 2, 4, 6, 8, 12, and 24 h at 16,000 rcf for 10 min to separate released DOX from GoMe particles. After that, the same amount of fresh medium was added to re-suspend the GoMe pellet. At 24 h post the start of the releasing experiment, the GoMe suspension was irradiated by an 808 nm laser for 10 min (2.83 W/cm^2). Sample was collected immediately by centrifugation after the irradiation. The sample was then incubated at 37 °C followed by sampling twice (at 1 h intervals), and then incubated till the next 24 h point. The whole release process was continued for 4 days. The amount of DOX in the supernatant was determined by a fluorospectrometer (Beckman Coulter DTX 880, excitation: 485 nm and emission: 545 nm).

GNS decorating density effect assay

The effects of different GNS density on a single MSN were explored by examining the product of the reaction between GNS and MSN at different time intervals. The reaction was carried out in a transparent 2.5 mL spectrophotometer cuvette. The UV absorbance spectrum was recorded directly as the reaction proceeding, while the photothermal converting capacity of the mixture was examined by irradiating the diluted reaction mixture with the 808 nm laser. The reaction was also monitored by observing the morphology of GoMe with the help of TEM.

Cellular internalization assay

The A 2058 cell, a human melanoma cell line, was cultured in Dulbecco's modification of eagle medium (Corning, Manassas, VA) supplemented with 10% FBS and 1% penicillin-streptomycin (Life Technology, Grand Island, NY) at 37 °C in 5% humidified CO_2 atmosphere. Cells were seeded in 35 mm petri dishes with a density of 200,000 cells/petri dish. After overnight incubation, 5 μM DOX@GoMe was added and continued incubation for another 3 h. Cells were washed once with complete medium and then stained with Hoechst 33342, followed by confocal microscopy imaging (LSM 700, Zeiss) and dark field microscopy imaging (Leica DM6000 M).

Live/dead cell assay after photothermal therapy

The photothermal effect of GoMe in cell culture medium was evaluated in a 96-well plate. GoMe of different concentrations were added to each well containing 100 μL complete medium. The resulting GoMe nano-suspension was irradiated with NIR laser (808 nm, 2.83 W/cm^2) for 10 min at predesigned time intervals and its temperature was monitored with a FLIR i7 thermal imaging camera and recorded every 1 min. To visualize the effect of laser irradiation on the cell death, Live/Dead cell imaging kit (Molecular Probe®) was used. 10,000 cells were seeded in 96-well plate and incubated at 37 °C in 5% CO_2 overnight. Blank GoMe (1 μM or 5 μM) was added and incubated for 2 h. For GoMe treated groups, an 808 nm laser was used to irradiate cells for 10 min, while others had no laser treatment. Cells were kept in the incubator for 2 h and stained with Live/Dead cell imaging kit according to the manufacturer's instruction. Each well

was imaged from 5 different positions (top, bottom, left, right and middle) with fluorescent microscopy (Axiovert 200, Carl Zeiss) under 20 × magnification using FITC and Texas red channels.

Cytotoxicity assay

For cell viability assays, A2058 cells were seeded in a 96-well plate (10,000 cells/well) and incubated at 37 °C in 5% CO_2 overnight. DOX, MSN, DOX@MSN, GoMe, and DOX@GoMe were diluted with complete medium to achieve targeted concentrations. After 24 h of incubation, GoMe and DOX@GoMe irradiation groups were exposed to 808 nm laser irradiation for 10 min. The cells were allowed to grow overnight and then added with MTT reagent. MTT stop solution was added after 4 h of incubation to dissolve MTT formazan crystals. The optical density of the medium was measured using a microplate reader (ELX808, Bio-Tech Instrument, Inc.) at λ = 595 nm.

^{64}Cu Radiolabeling of GoMe Nanoparticle

DOTA was conjugated onto GoMe nanoparticles by adding Maleimide-mono-amide-DOTA (20 mM, 50 μL in DMSO) to 1 mg GoMe aqueous solution (1 mg/ml). After 6 h of reaction at room temperature, the free DOTA was separated from GoMe by centrifugation and washing with DI water twice. The resulting pellet was re-suspended in 1 ml DI water. GoMe nanoparticles were further radiolabeled by 64Cu via the DOTA chelator as previously reported [58]. The radiolabeling was accomplished by addition of 1.0-1.5 mCi of $^{64}CuCl_2$ in 0.1 M HCl (University of Wisconsin) to a mixture of 50 μL 0.1 N ammonium acetate (pH 5.5) buffer and 150-200 μL of the nanoparticles suspension, followed by

incubation at 37 °C for 30 min. The radiolabeled nanoparticles were collected into 300-400 μL of phosphate buffered saline by centrifugation.

Animal model establishment

All experiments were carried out under protocols approved by the Institutional Animal Care and Use Committee. Our mouse model was based on one reported by Berr's group.[58] Female FVB mice (Jackson Laboratory) aged 6-8 weeks received weekly intraperitoneal (IP) injections of 1 mg urethane/g body weight dissolved in sterile 0.9% NaCl. Twenty weeks after the initial urethane injection, MRI was used to verify lung tumor presence. PET imaging was performed when at least one lung tumor reached 1.5 mm in diameter.

MRI and PET Animal imaging

Twenty-four weeks after urethane treatment, lung tumor bearing mice were first imaged on a 7 Tesla ClinScan MRI system (Bruker BioSpin Corporation, Billerica, MA), Inc., Palo Alto, CA). MRI were acquired with a cardiac and respiratory gated, multi-slice, spin-echo sequence developed in our lab with the following parameters: field of view 30 mm, effective matrix = 192 × 192 zero-filled to 256 × 256, slice thickness 0.7 mm, TR was a function of the breathing cycle and averaged to about 1 second. The TE was 11ms, the number of averages was 4, and the number of slices was 15 with a gap equal to 0.7mm between slices to avoid crosstalk. The slice stack was moved by 0.7mm and 15 other interleaved slices were acquired. Gadolinium-DTPA contrast agent (Magnevist; Bayer Schering Pharma, Berlin, Germany) was injected at a dose of 50 mmol/kg body weight in the hind leg muscle. Before PET imaging, mice were

injected with 64Cu-labeled GoMe nanoparticles via the lateral tail vein. Each mouse received 500-750 μCi of 64Cu for a total volume of 150-200 μL. Mice were imaged using a Focus 120 PET scanner (Positron Emission Tomography) (Siemens, Knoxville, TN) at 6 h and 20 h post administration. During the 40 min PET acquisition, anesthesia was maintained using 1.25% isoflurane in O_2 inhaled through a nose cone. Heart rate, respiration, and rectal temperature were monitored (SAII, Stony Brook, NY). PET data were reconstructed using OSEM algorithm with 2 iterations and 12 subsets followed by MAP algorithm (18 iterations). The reconstructed image (not corrected for attenuation) was composed of 95 axial slices of thickness 0.79 mm with an in-plane voxel dimension of 0.4 mm × 0.4 mm (128 × 128 pixels).

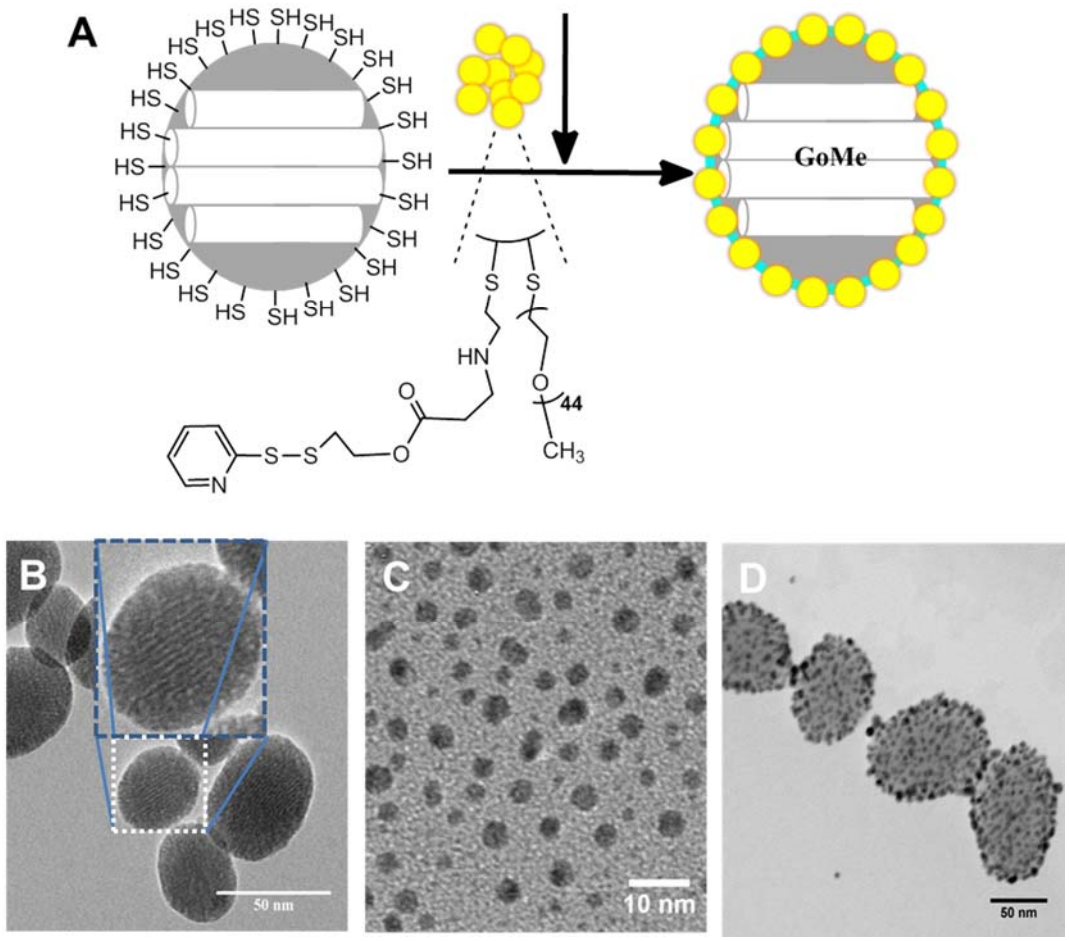

Figure 2.1 Schematic illustration of the fabrication of GoMe. (A) The preparation scheme of GoMe. (B-D) TEM images of MSN, PEG-GNS, and GoMe nanoparticles. Scale bars are 50, 10, and 50 nm in (B), (C), and (D), respectively. The inset in (B) shows the TEM image of one individual MSN.

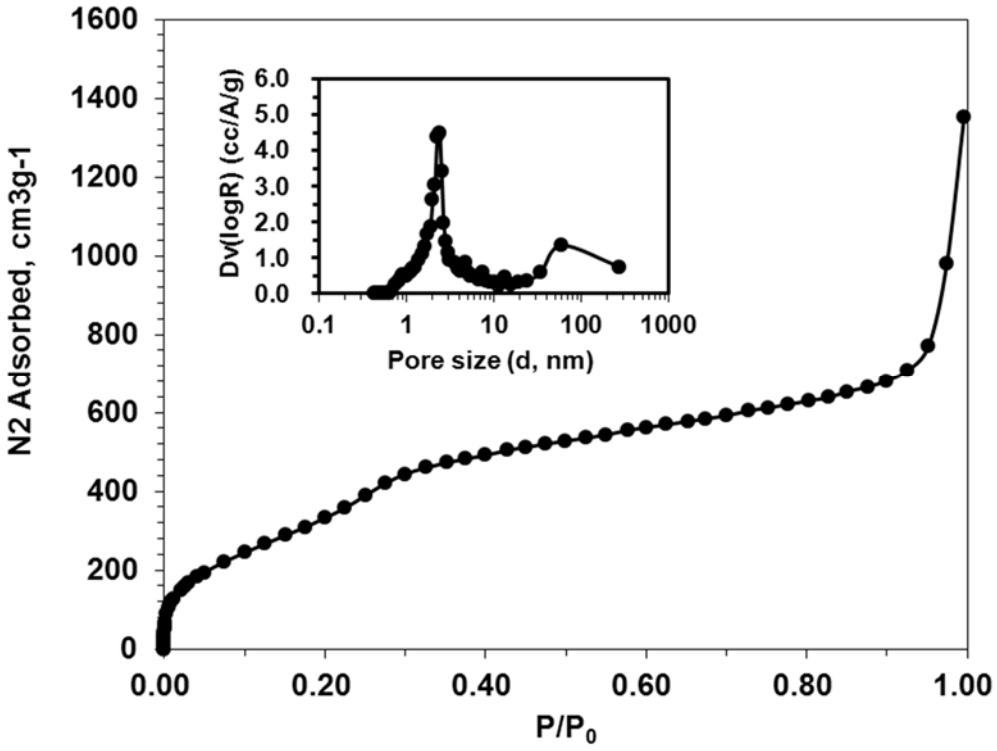

Figure 2.2 Nitrogen adsorption isotherm for MSN. The insert shows the pore size distribution.

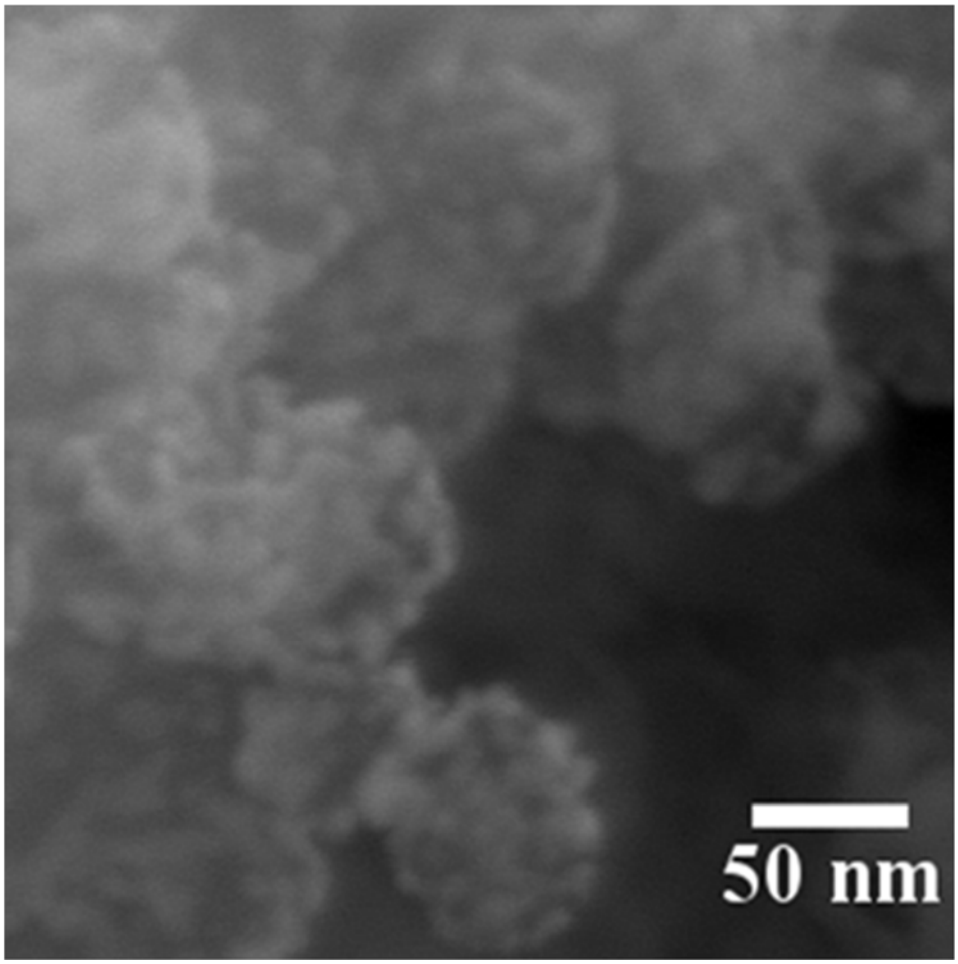

Figure 2.3 SEM image of GoMe. Image was acquired with a Zeiss Ultra Plus FESEM at the magnification of 300,000 ×.

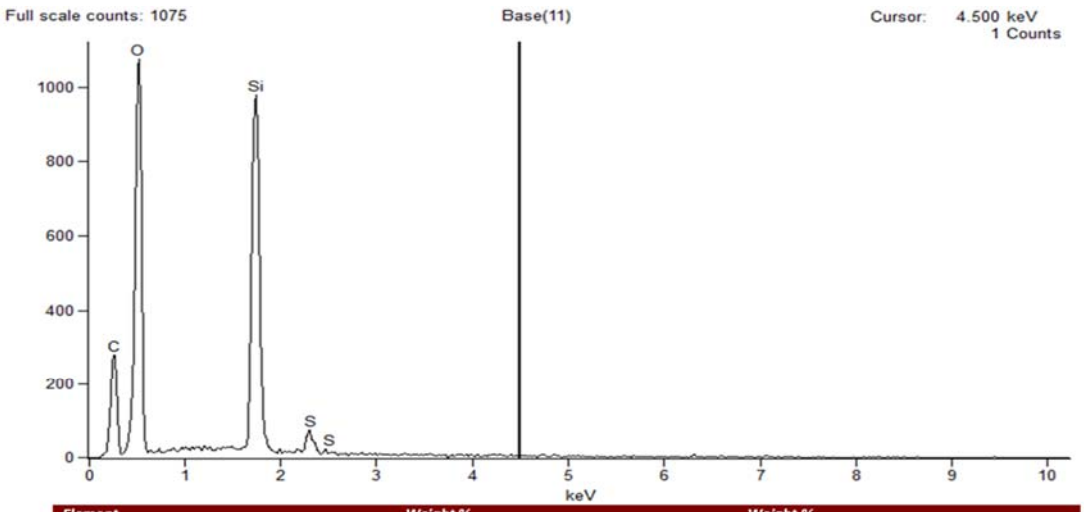

Element	Weight %	Weight % Error
C	28.34	± 0.92
O	42.52	± 0.56
Si	26.88	± 0.33
S	2.26	± 0.25
Total	100.00	

Figure 2.4 SEM-EDX analysis of MSN-SH.

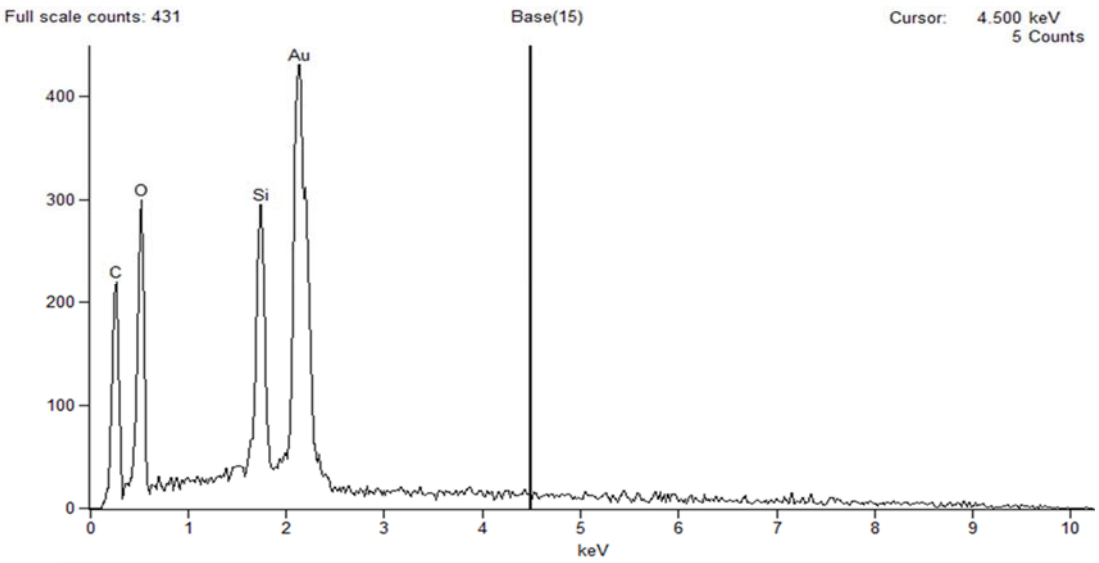

Element	Weight %	Weight % Error
C	20.00	± 0.72
O	14.71	± 0.57
Si	7.73	± 0.34
Au	57.56	± 1.65
Total	100.00	

Figure 2.5 SEM-EDX analysis of GoMe.

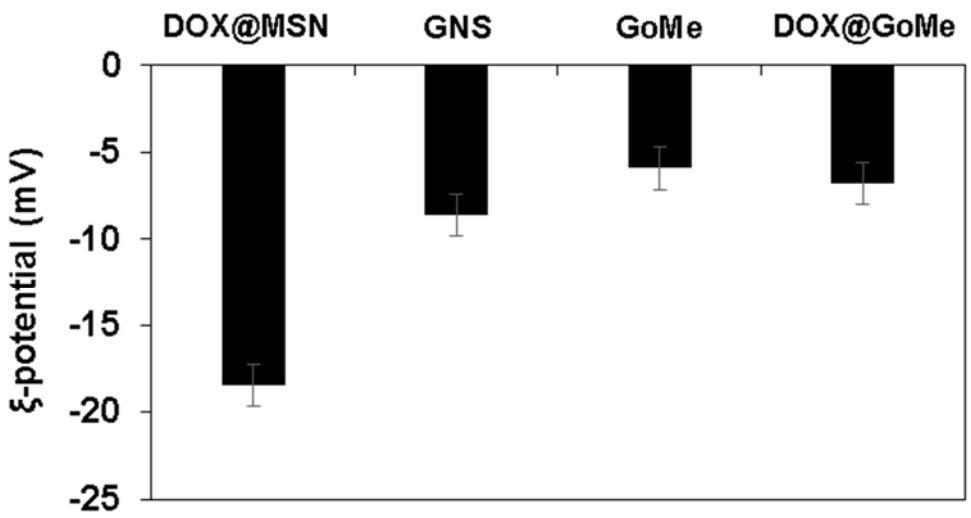

Figure 2.6 The surface charge of MSN, GNS, GoMe, and DOX@GoMe.

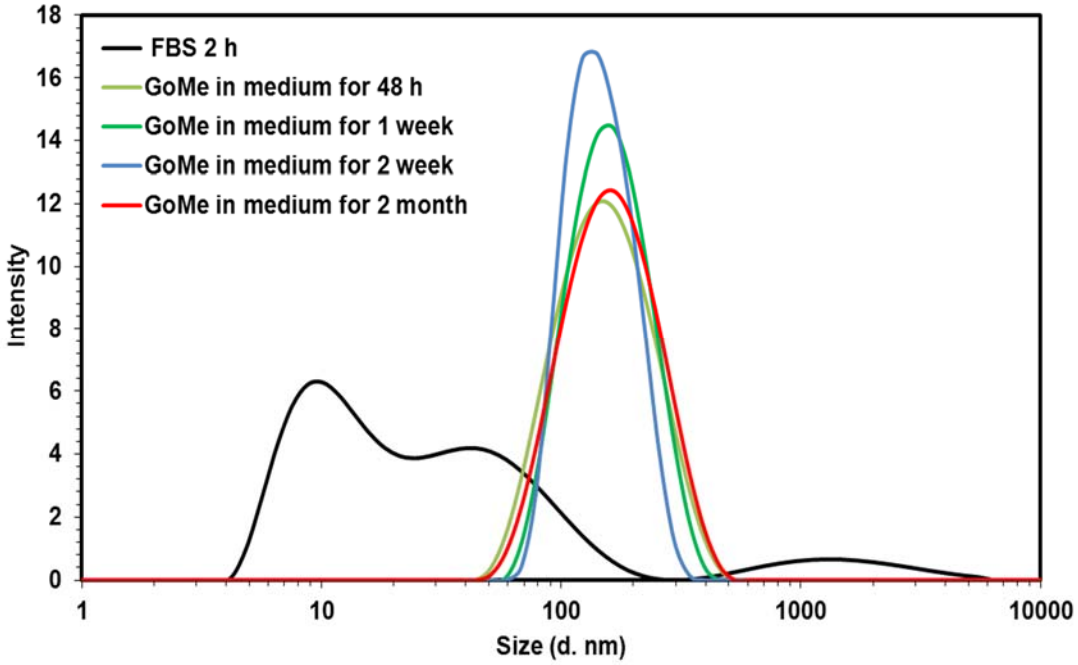

Figure 2.7 Size distribution of GoMe in 10% FBS.

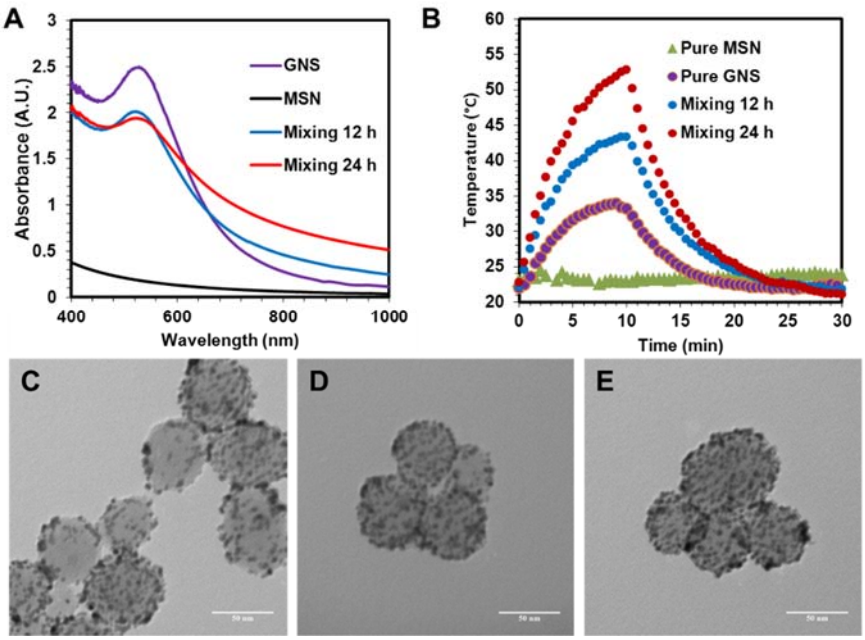

Figure 2.8 Reaction monitoring of GNS conjugation to MSN with UV and TEM. The UV-Vis spectra of GNS, MSN, and their mixture after 12 and 24 h of reaction (A), as well as their photothermal heating curves upon 10 min of 808 nm laser irradiation (2.83 W/cm^2) (B). TEM images of GoMe formed after 2 h (C), 12 (D), and 24 h (E) of mixing GNS and MSN. Scale bars are 50 nm in (C), (D), and (E).

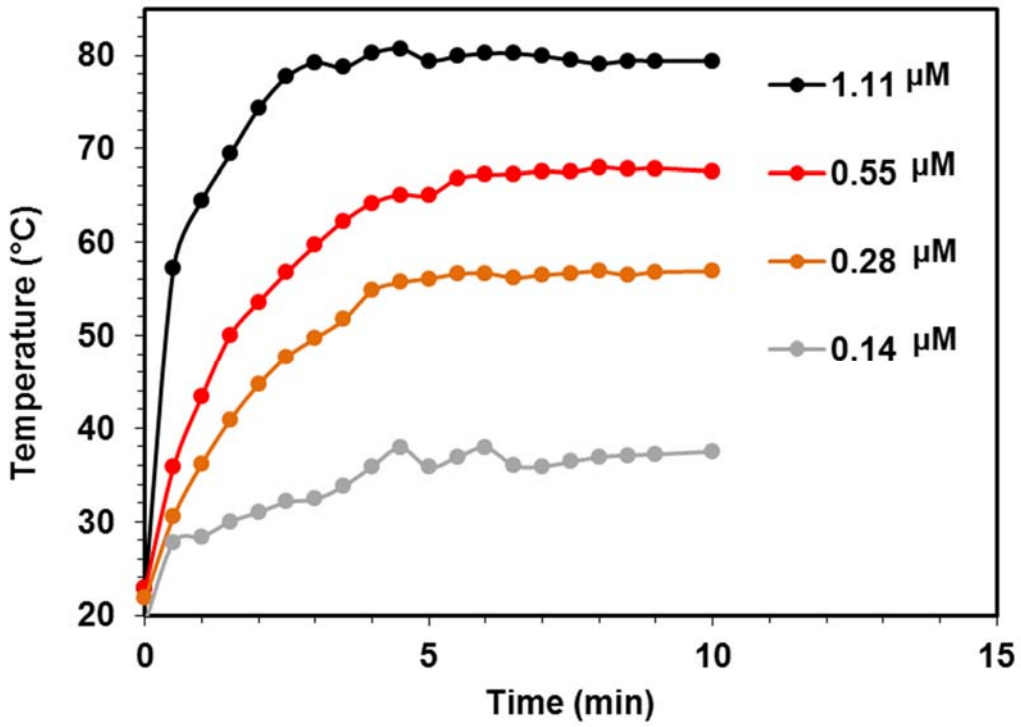

Figure 2.9 The photothermal effect of GoMe at different concentrations. Nano-suspension of GoMe was irradiated by the 808 nm laser (2.83 W/cm^2).

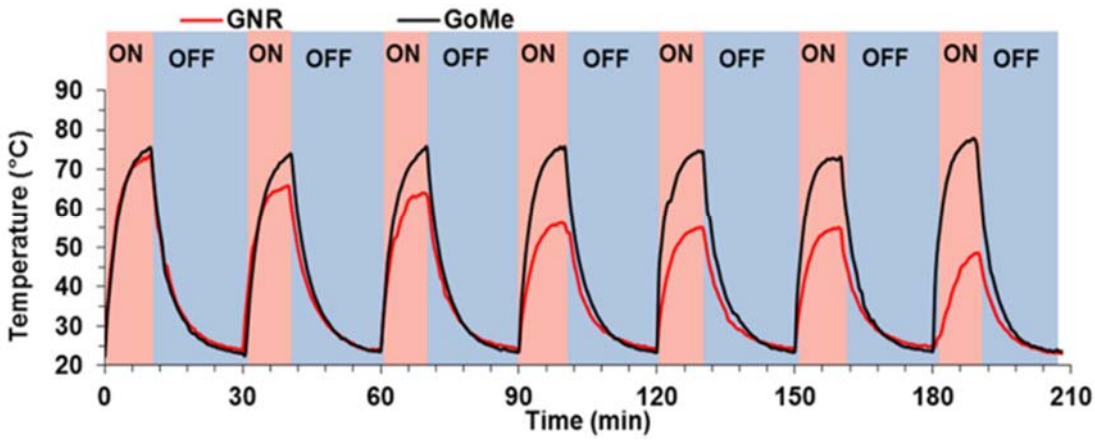

Figure 2.10 Real-time temperature elevation of GoMe and GNR nano-suspensions during 7 cycles of NIR irradiation. GoMe and GNR were irradiated with an 808 nm NIR laser for 10 min (2.83 W/cm^2) and then cooled down for 20 min. The last cycle was carried out 24 h after the 6th cycle.

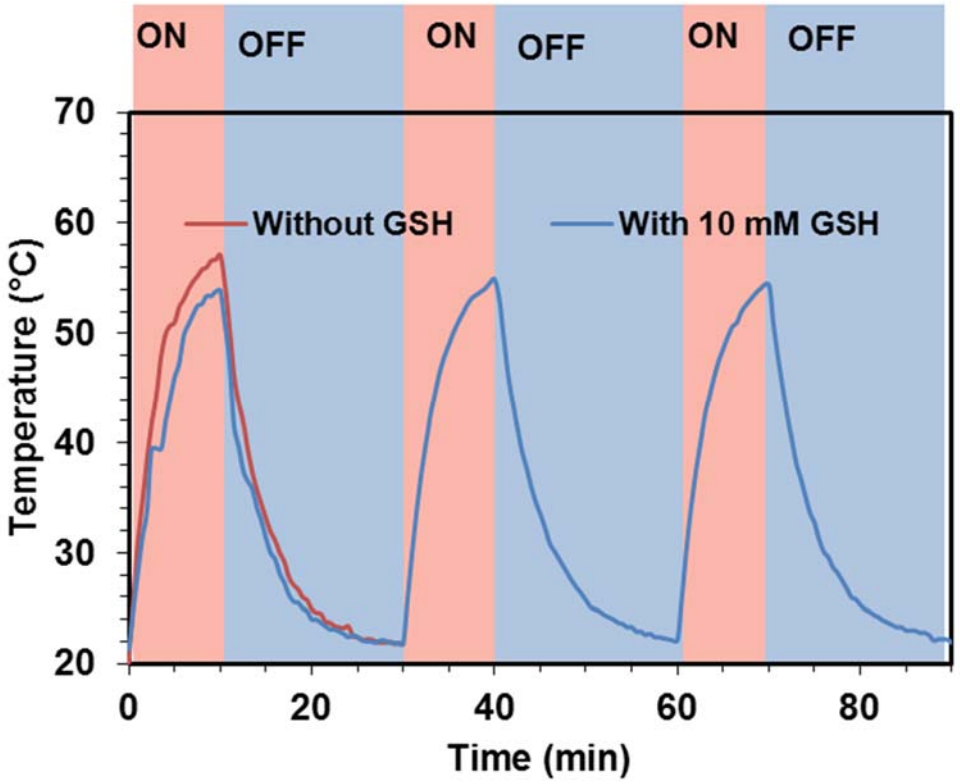

Figure 2.11 The photothermal effect of GoMe in medium with or without GSH. Nano-suspension of GoMe was irradiated by the 808 nm laser (2.83 W/cm^2, 10 min on and 20 min off).

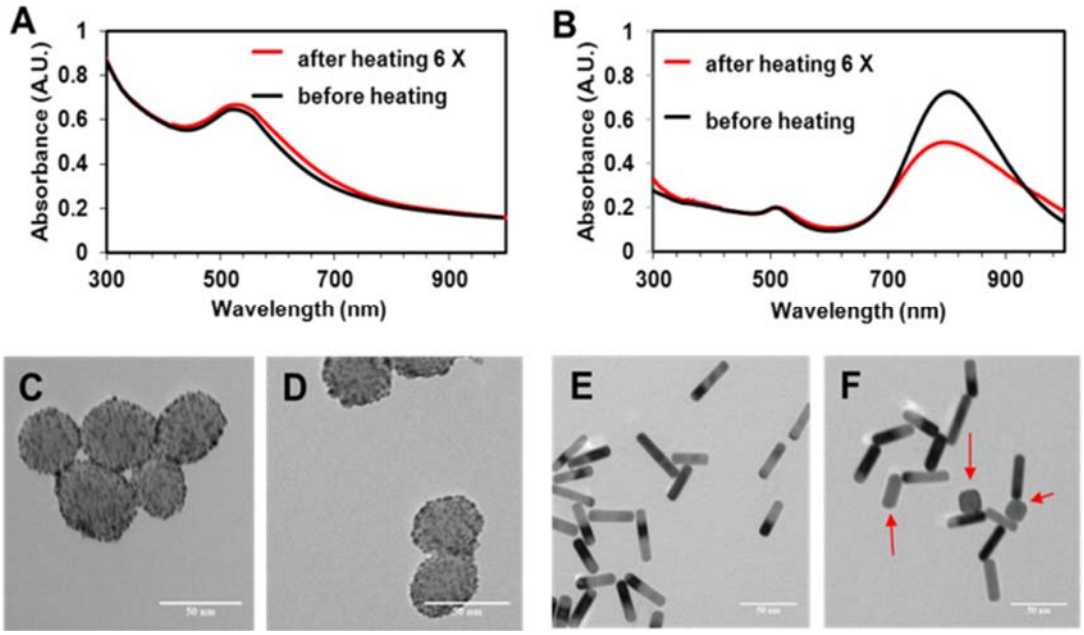

Figure 2.12 The UV-Vis spectra and TEM images of GoMe and GNR changed due to repeated photoirradiation. The UV-Vis spectra (A) and TEM images of GoMe (C, D), and the UV-Vis spectra (B) and TEM images of GNR (E, F). TEM images of GoMe before laser irradiation (C) and after 5 cycles of irradiation induced heating/cooling (D). TEM images of GNR before laser irradiation (E) and after 5 cycles of irradiation induced heating/cooling (F). Red arrows indicate those GNRs changed to round shape (F). Scale bars are 50 nm in all images.

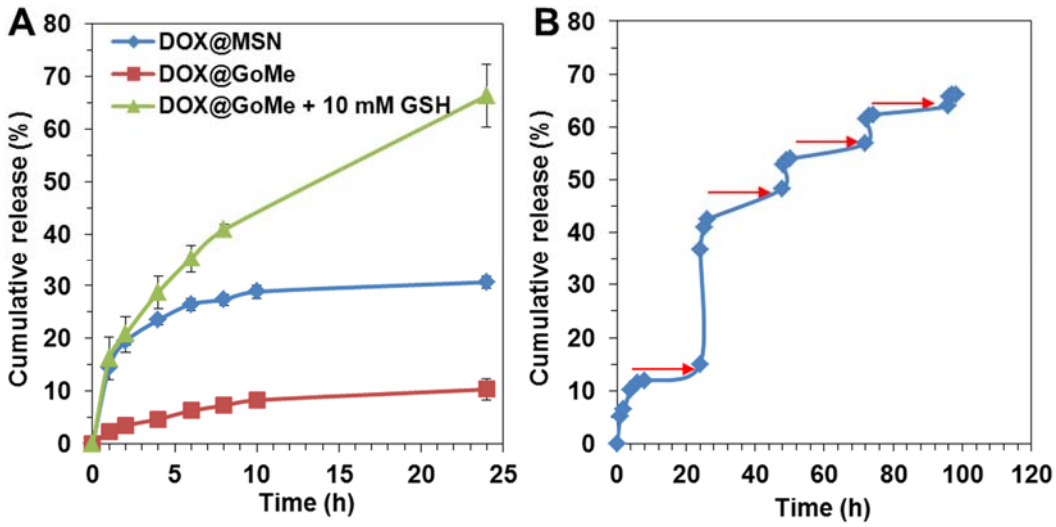

Figure 2.13 The release kinetics of GoMe in different conditions. In plain PBS or PBS supplemented with GSH (A) and under the trigger of NIR irradiation (B). The red arrows indicate the time points when the irradiation (10 min, 2.83 W/cm^2) was applied.

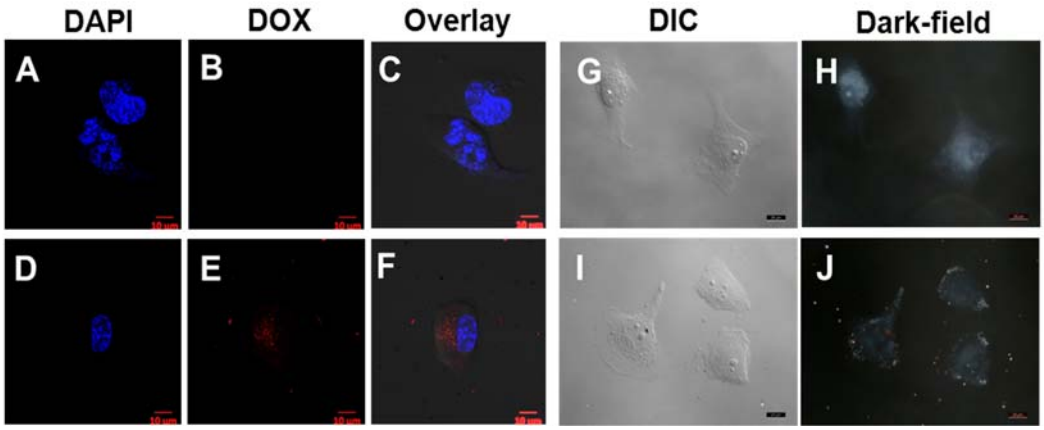

Figure 2.14 The uptake of DOX@GoMe by confocal and dark-field microscopy. The confocal (A-F) and dark-field (G-J) images of A2058 cells co-cultured with DOX@GoMe. Cells in A-C, and G-H were control. Cells in D-F, and I-J were treated with DOX@GoMe. Images H and J were collected in dark-field mode. Scale bars in A-J are 10 μm.

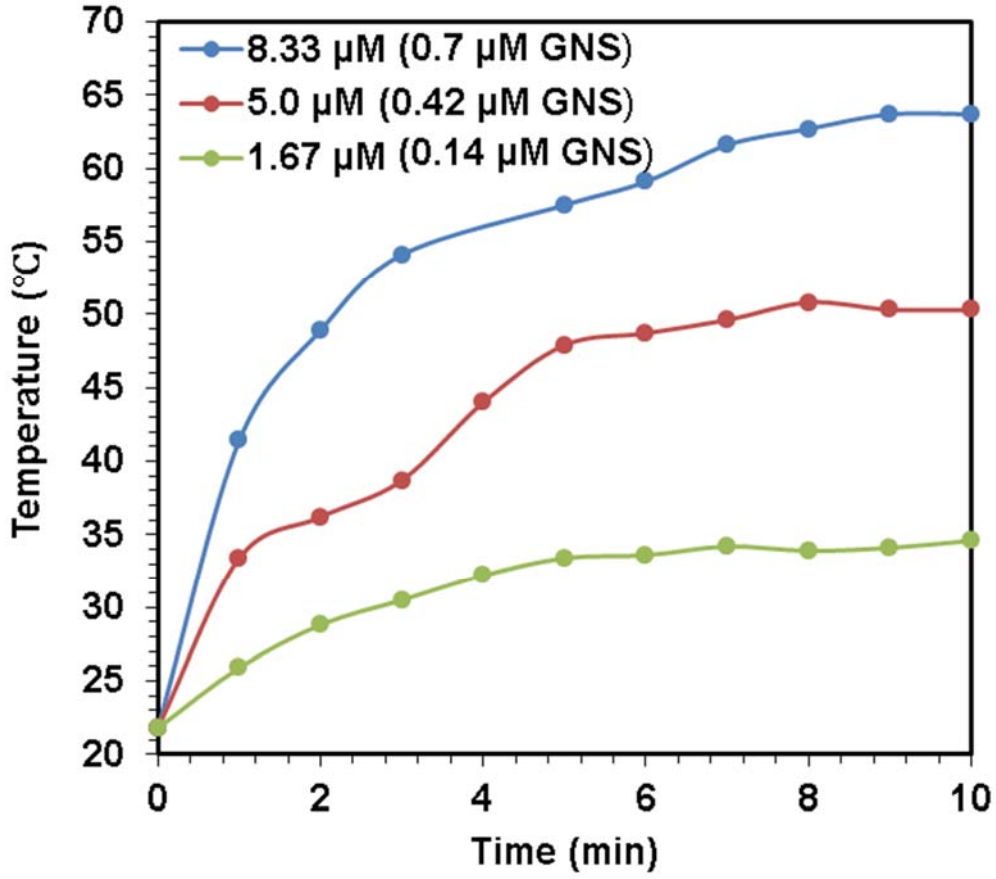

Figure 2.15 The real-time medium temperature during NIR laser irradiation of different GoMe concentrations. GoMe concentration was calculated based on corresponding DOX concentration.

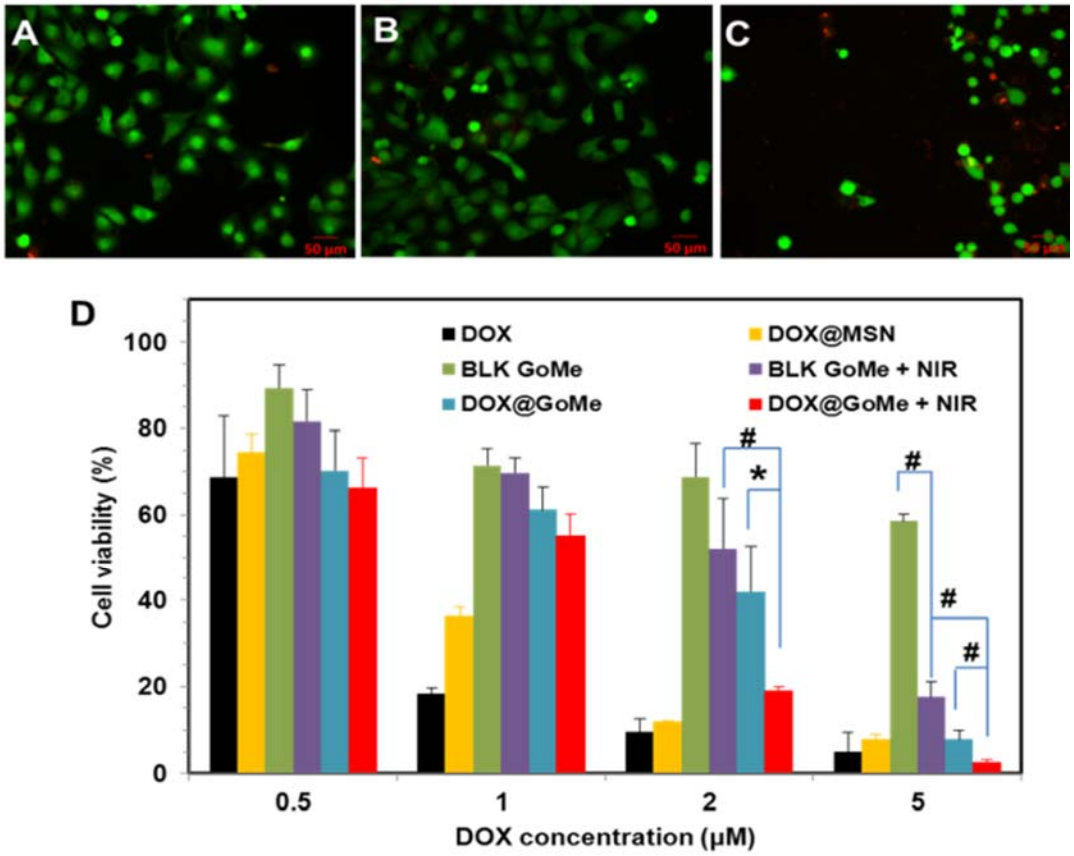

Figure 2.16 Cytotoxicity of DOX@GoMe coupled with NIR irradiation. The fluorescent images of live/dead cell assay (A-C) after NIR irradiation and the cytotoxicity of DOX@GoMe coupled with NIR irradiation (10 min, 2.83 W/cm^2) (mean ± SD, $P < 0.05$ *; $P < 0.01$ #). Cells in A, B, and C were treated with blank medium, blank GoMe, and GoMe coupled with NIR irradiation, respectively. Scale bars in A-C are 50 μm. (D) Cytotoxicity of various treatment in UMSCC 22A cells.

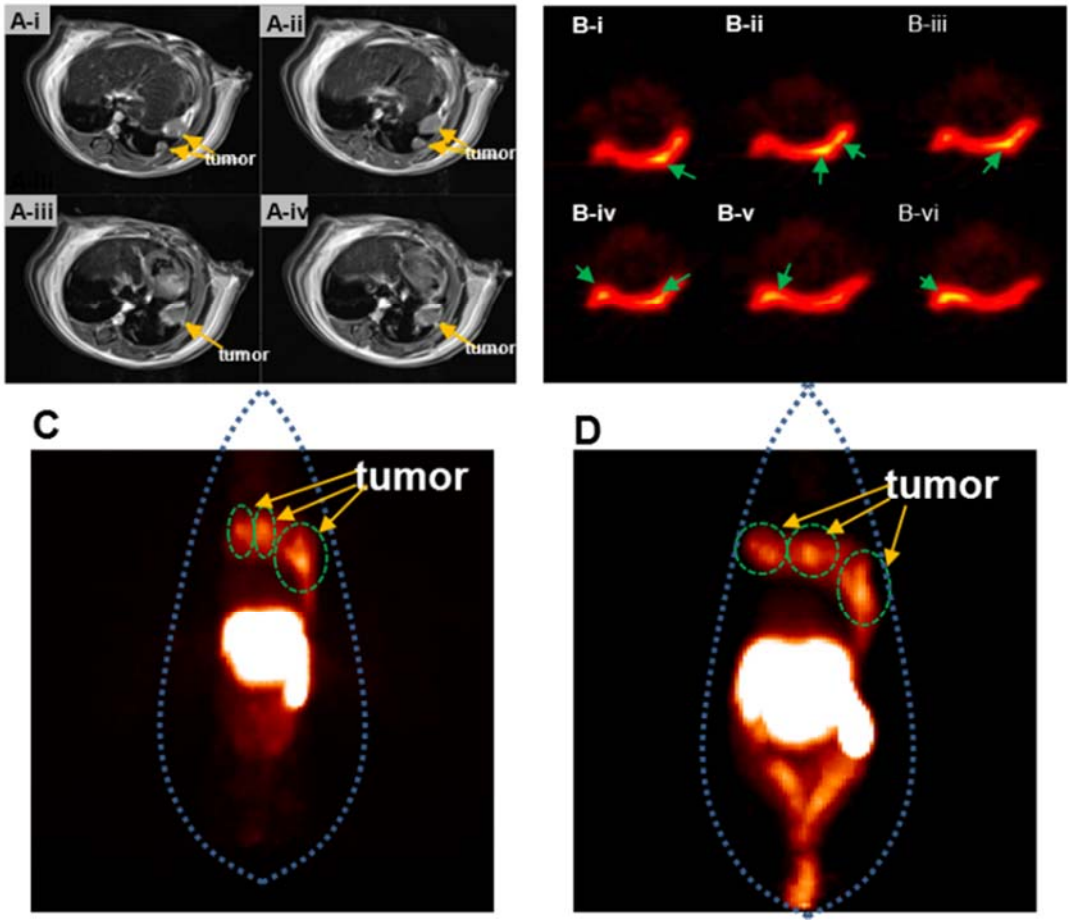

Figure 2.17 MRI and PET animal imaging. (A) Four contiguous MRI transverse images, (B-D) PET images of 3 tumors in the lung of mouse received radiolabeled GoMe. Tumors are indicated by yellow arrows in (A). (B) PET images of contiguous slices in transverse acquired 6 h post administration. Tumors are indicated by green arrows in (B). Whole body PET images acquired 6 h (C) and 20 h (D) post administration.

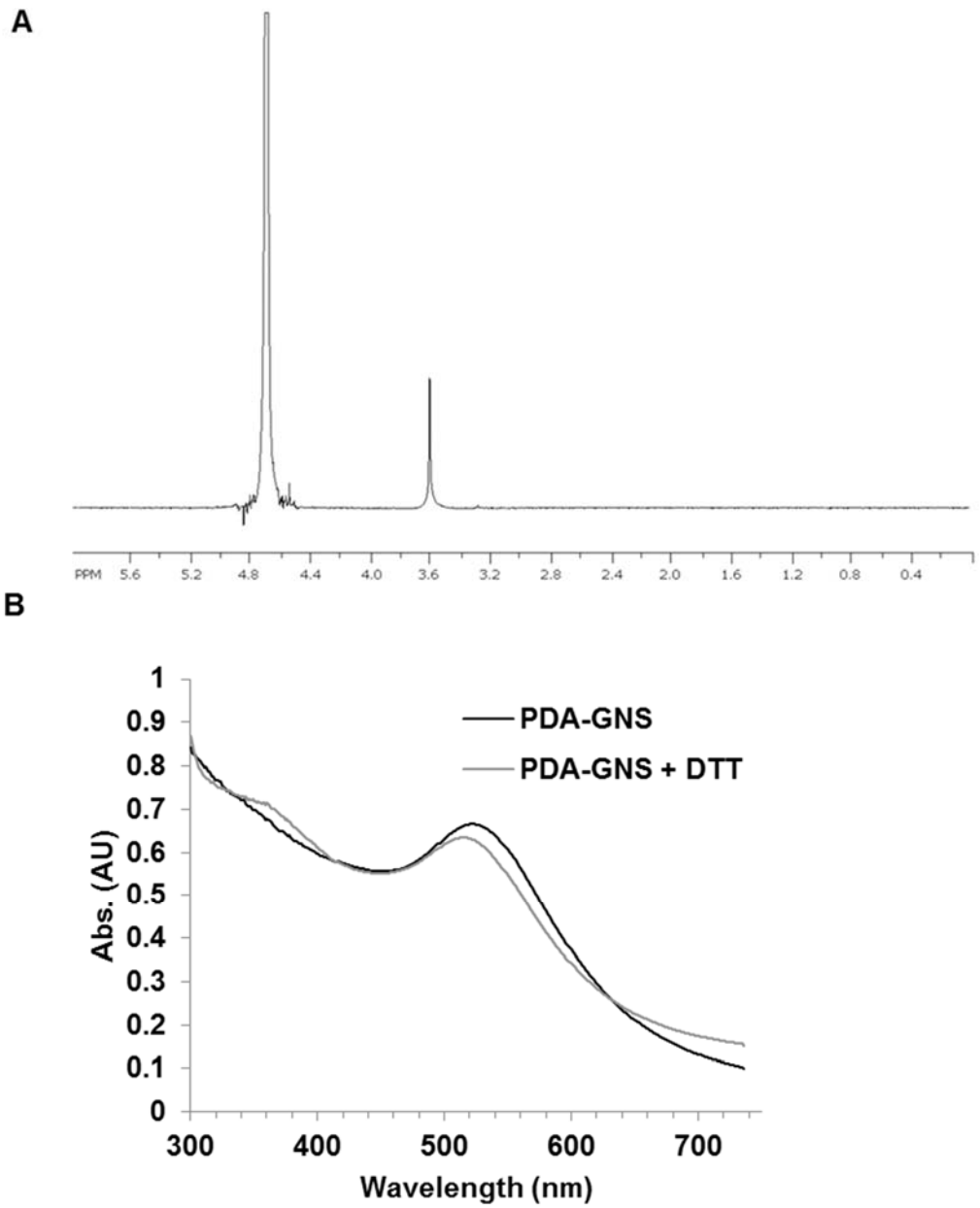

Figure 2.18 ^{1}H-NMR of PEG-GNS and the UV-Vis spectra of PDAGNS. (A) ^{1}H-NMR of PEG-GNS in D_2O. (B) The UV-Vis spectra of PDA-GNS.

CHAPTER 3

Sigma receptors targeted GoMe for cancer photothermal therapy and photodynamic therapy

ABSTRACT

Although various nanocarriers have been developed to treat cancer, how to use a multifunctional nano-carrier to treat cancer patients more efficiently and personalized remains to be a challenge. Here, we present a gold nanoparticle conjugated mesoporous silica nanoparticles hybrid (GoMe) as a carrier for Pc 4. The results show that GoMe actively targets sigma 2 receptors overexpressing cancer cells, and rapidly releases Pc 4 inside cancer cells upon the high reducing intracellular environment or external laser irradiation. Pc 4 coupled with 660 nm laser irradiation generates singlet oxygen in the mitochondria of oxygen-rich tumor tissues and initiates the subsequent cell apoptosis or necrosis, and the remaining tumor cells in hypoxia regions are killed immediately upon subsequent 808 nm laser irradiation toward GoMe. Our study shows that GoMe is superior in inhibiting cross-resistance with any other chemotherapy, and more importantly, it is highly efficient in eradicating tumors in UMSCC 22A xenograft mice model. Our design can serve as the site specific anti-cancer therapy and be a promising candidate for clinical use.

INTRODUCTION

Photodynamic therapy (PDT) is a clinically approved effective strategy against various malignant cells.[59] Three elements are essential in the application of PDT, light, photosensitizer (PS) and oxygen. It's a two-stage reaction process: Firstly, PS is applied in the disease foci and exposed to light at a specific wavelength corresponding to the type of PS. Then, energy transferred from the light by PS will initiate a series of consequences at the presence of oxygen which will eventually cause the cell apoptosis or necrosis, systemic immune reaction and destruction of microvasculature. The major advantage of PDT is its unique oxygen-dependent tumor cells eradiation mechanism, which is unlikely to generate cross-resistance with other therapies.[60] It is especially beneficial for the tumor that is inoperable. Another advantage of PDT relies on its boosting systemic immunity function.[61] Until now, there are over 200 clinical trials using PDT in the field of skin melanoma, head and neck, non-small lung, bladder, ovarian, and brain cancers.[62]

However, the application of PDT in anticancer is greatly impaired by the requirement for the rich oxygen environment, which is not always available in solid tumor microenvironment. A solid tumor is composed with mild to severe hypoxia regions as well as re-oxygenation regions. With the dynamic oxygen flow occurring within these tumor areas through the chaos position of newly generating vasculatures, it can greatly reduce therapeutic potential of PDT.[63] In addition, PDT induced the destruction of tumor vasculature will cause oxygen depletion and increase hypoxia areas. In order to maximize the efficacy of PDT,

it's crucial to deliver and maintain a therapeutic level of PS in all tumors and to reduce its liability on the oxygen level.

Abundant trials have been performed by either modulating the light delivery or applying an excessive oxygen during PDT.[64] In order to achieve a higher oxygen level in tumor foci, patients who were receiving PDT were maintained under the hyperbaric oxygen condition. The combination of PDT and hyperbaric oxygen supply elongates the mean survival time for patients with squamous cell carcinoma or adenocarcinoma.[64c] Instead of continuous illumination, disrupting illumination in two fractions with refractory interval was practiced on the rats bearing U87 human primary glioblastoma tumor and results showed a severe necrosis in tumor tissue, indicating a better therapeutic effect.[64b] Nanomedicine was developed to overcome these challenges, and polymer based nanoparticles,[65] carbon nanodots,[66] and superparamagnetic iron oxide nanoparticle[67] were good candidates to deliver PDT. More recently, a co-doped nanoparticle was developed to co-deliver PS H_2TPyP and chemotherapeutic agent curcumin to treat A549 human alveolar adenocarcinoma xenograft mice model. They successfully reduced the tumor volume by 74% through daily injection of the nanoparticle.[68]

Here we developed a new nanocarrier that combined PDT and (photothermal therapy) PTT by loading Pc 4 into gold nanoparticle-mesoporous silica nanoparticle hybrid (GoMe). The GoMe was able to efficiently and specifically enter cancer cell through sigma 2 receptor mediated endocytosis and maintain a stable and controlled dose of Pc 4 required for PDT in the tumor foci,

and completely eradicate cancer cells with minimized side effects. Intracellular GSH level or low pH environment in lysosome would trigger the release of Pc 4, and upon the irradiation of a 660 nm laser, cells containing Pc 4 were killed through either ROS induced cell apoptosis or necrosis. Cells in the hypoxia areas survived from PDT were immediately burned by 808 nm photoirradiation. We first tested the physical properties and biocompatibility of GoMe in physiological environment, and examined the dual responsiveness of Pc 4 GoMe to intracellular high redox potential environment and external photoirradiation. Secondly, we elucidated the subcellular targets of MBA Pc 4 GoMe and its mechanism of producing reactive oxygen species. Last, we validated the synergistic efficacy of PDT and PTT of these nanoparticles in UMSCC 22A head and neck bearing xenograft mice.

Results and discussion

Synthesis of MBA PC 4 GoMe

Silicon phthalocyanine Pc 4 is used to treat squamous cell carcinoma and skin cancer in various clinical trials. Pc 4 GoMe was prepared by conjugating Pc 4 loaded MSN with gold nanospheres. Pc 4 loaded MSN was evenly covered by PEG-SH (Mw=3400) stabilized gold nanosphere.[69] TEM revealed that the final diameter of GoMe reached 50 nm (**Figure 3.2B**). The UV absorbance of Pc 4, PC 4 MSN or Pc 4 GoMe appeared at 680 nm (**Figure 3.2F**), suggesting that the efficient Pc 4 based PDT should occur upon a 660 nm laser irradiation.

To conjugate targeting moiety to Pc 4 GoMe, 4-methoxybenzoic acid (MBA) modified PEG was synthesized through the EDC/NHS reaction between

the amine in polymer NH_2-PEG-Mal and the carboxylate group of MBA as shown in **Figure 3.1B**. The successful conjugation of MBA to SH-PEG-Mal was confirmed by ^{1}H-NMR as shown in **Figure 3.2E**, where the existence of MBA was evidenced by the peak at 7.8 ppm (2H). The quantification of MBA conjugation efficiency was tested by TNBSA assay. By comparing the available free amine in MBA-polymer PEG-Mal to that in NH_2-PEG-Mal, we concluded that 85.62% of the free amine in NH_2-PEG-Mal was replaced by MBA.

MBA-Pc 4 GoMe didn't exhibit an increased size comparing to Pc 4 GoMe according to TEM and SEM, but DLS showed a slight increase (about 24 nm) (**Figure 3.2B-D and 3.3A**). Comparing with Pc 4 GoMe, the surface charge of MBA-Pc 4 GoMe was decreased from -1.13 mV to -2.93 mV (**Figure 3.3A**).

Photothermal response of Pc 4 GoMe

To evaluate the photothermal response of Pc 4 GoMe, we tested the photothermal capacity of Pc 4 GoMe at different concentrations. The absorbance at 450 nm was used to represent Pc 4 GoMe concentration, as it is an indicator for the density of gold on the surface of MSN.[70] As shown in **Figure 3.3B**, the absorbance at 450 nm positively correlated with the concentration of Pc 4 GoMe. When the OD at 450 nm was at 0.08, it was enough to generate the energy that can heat the surrounding aqueous solution up for 14.2 °C, while with the OD increasing to 0.65, it was able to reach 63 °C after 10 min irradiation (**Figure 3.3C**). The heat transducing efficiency was 28% based on **Figure 3.3D**. Neither water, MSN, nor gold nanoparticle themselves were able to generate enough heat to reach comparable temperature elevation (data not shown). PC 4 GoMe,

as we previously proved, is a thermal stable nano-carrier that can maintain its integrity upon intensive and repetitive irradiation.[69] If the cancer cells have not been completely eradicated in any scenario, a repeatable PTT can be applied without any additional dose.

Colloidal stability and release behaviors of Pc 4 GoMe

The strong advantages of this system lie in its colloid stability during circulation and responsiveness to intracellular signal and external NIR irradiation. The premature release of Pc 4 in blood circulation or in the undesirable tissue would lead to decreased bioavailability for target site and increased skin sensitivity toward light.[71] Our design can avoid this risk by sealing the Pc 4 inside the pore channels of MSN during circulation. Once it enters the targeting cancer cells, Pc 4 can be released by two mechanisms: firstly, intracellular high redox potential partially cleaves the disulfide bond and loosen gold on the surface of MSN, which induces release of Pc 4. Second, Pc 4 release can also be switched on by NIR irradiation at 808 nm on GoMe, where an intensive heat will be generated and followed by Pc 4 release. **Figure 3.4A** showed that with the addition of 10 mM GSH in medium, Pc 4 GoMe doubled its release at the first hour of incubation and released over 50% of its loading by the end of 24 h. In addition, it was confirmed that Pc 4 GoMe showed a complete release of Pc 4 after laser irradiation at 808 nm for 10 mins, indicating that Pc 4 is able to completely escape from the hybrid nanoparticle structure after PTT (**Figure 3.4B**).

Colloidal stability is an important indicator for the destiny of administered NPs *in vivo*, in which aggregated nanoparticles will alter drug pharmacokinetics, toxicity and biodistribution. We used several media to estimate Pc4 GoMe stability, including different concentrations of serum containing DMEM media and PBS considering of the potential effects of ion strength and protein adsorption. Pc 4 GoMe at the concentration of 100 μg/mL in 10% FBS containing DMEM media showed no significantly increase in hydrodynamic size for up to one week (**Figure 3.4D**). Meanwhile, we also investigated the release of Pc 4 during this period and found that in 10% serum containing medium at 37 °C, Pc 4 only released less than 10% of its loading by the end of 48 h. In 50% serum medium, Pc 4 would only release around 30% at the end of 48 h incubation (**Figure 3.4C**). Therefore, Pc 4 GoMe was not prone to aggregate in circulation and showed an excellent serum compatibility.

Reactive oxygen species

PS can produce ROS through type I and type II reaction. For Pc 4, it mainly goes through the type II reaction. Instead of directly producing hydroxyl and superoxide radicals, it reacts with tissue oxygen and produces singlet oxygen upon excitation.[72] We evaluated the capability of PC 4 GoMe in generating singlet oxygen using both 9,10-dimethylanthracene (DMA) and SOSG assays.[73]

DMA reacts with $^1O_2$ (singlet oxygen) and forms non-fluorescent 9,10-endoperoxide.[74] **Figure 3.5A** revealed that the fluorescence of DMA decreased with the co-incubation of Pc 4, Pc 4 GoMe or Pc 4 GoMe with GSH. The

decrease of DMA fluorescence at 432 nm was proportional to the photoirradiation duration. Longer co-incubation with GSH (16 h) was able to diminish the fluorescent intensity by 61.4%, almost reaching the activity of free Pc 4.

To further study the singlet oxygen generating capacity of the nanoparticle, fluorescently-quiescent SOSG which can react specifically with singlet oxygen and produce a fluorescent SOSG-endoperoxide molecules was employed. **Figure 3.5B-E** showed the Pc 4 generated the highest singlet oxygen level after photoirradiation, and Pc 4 GoMe generated 73% of singlet oxygen compared with free Pc 4. However, 24 h of GSH pretreatment boosted the singlet oxygen generating capacity of Pc 4 GoMe to 90% of that of free Pc 4.

As evidenced from the above *in vitro* results, Pc 4 GoMe was nearly as effective as free Pc 4 in generating singlet oxygen after GSH treatment. We further evaluated the intracellular oxygen species levels induced by Pc 4 GoMe. As we discussed earlier, the intracellular GSH level is significantly higher than that of the extracellular matrix. It is expected that after the internalization of nanoparticles, GSH would trigger the release of Pc 4, which can generate singlet oxygen upon photoirradiation. Since SOSG itself is a weak photosensitizer, various controls were employed to exclude the effect of either SOSG, NIR or Pc 4 themselves. Without NIR, neither Pc 4 nor Pc 4 GoMe could generate detectable signals of oxidized SOSG. In response to NIR, they generated a strong green fluorescence indicating the abundant existence of intracellular singlet oxygen. In addition, there was no significant difference among the Pc 4, Pc 4 GoMe and MBA Pc 4 GoMe groups (**Figure 3.6**).

Cellular uptake of MBA Pc 4 GoMe

Sigma 2 receptors were overexpressed in UMSCC 22A cells. Therefore, MBA with high affinity to sigma 2 receptors was chosen as the targeting moiety for UMSCC 22A cells.[32b, 75] In our study, the targeting moiety MBA was conjugated on the surface of nanoparticles, which ensures its availability when nanoparticle was exposed to cells. To investigate the internalization efficiency of MBA Pc 4 GoMe, UMSCC 22A cells were treated with free drug or GoMe or MBA GoMe and examined with FACS and confocal microscopy. **Figure 3.7A** showed that longer co-incubation led to an increased internalization of Pc 4 into cells at 37 °C. Both Pc 4 GoMe and MBA Pc 4 GoMe treatments showed a better uptake than free Pc 4. MBA Pc 4 GoMe showed the highest uptake, where over 40% of Pc 4 was internalized inside cells compared with free Pc 4 (**Figure 3.7A-C**).

Previous research showed that hydrophobic PS enters cells by the incorporation into lipoproteins such as low density lipoproteins (LDL) and followed by LDL-receptors dependent endocytosis[76] and MBA Pc4 GoMe enters cell through sigma 2 receptor mediated endocytosis. Since the endocytosis is an energy dependent process, a lower temperature would reduce the uptake of Pc 4 or Pc 4 GoMe.[77] We compared the uptake behaviors of these nanoparticles at 4 °C and observed a significantly decrease of Pc 4 uptake (**Figure 3.7D-F**). The uptake of MBA Pc 4 GoMe group was reduced mostly by the lower temperature, suggesting that the internalization of MBA Pc 4 GoMe relied on endocytosis mostly.

Confocal microscopy was employed to study the role of MBA in MBA Pc 4 GoMe internalization. As shown in **Figure 3.7G**, with the addition of free MBA, the total Pc 4 uptake was significantly inhibited. It is suggested that the free MBA was able to partially block the accessibility of sigma 2 receptors, which subsequently interfered the interaction of MBA Pc 4 GoMe with the cells and negatively impacted its uptake.

Characterize PDT of Pc 4 GoMe for UMSCC 22A cells

We have shown that MBA Pc 4 GoMe enters the cells more efficiently than Pc 4 GoMe and Pc 4. We then tested whether enhanced uptake of Pc 4 resulted in better photodynamic therapy. After Pc 4 entered cells, it primarily located in the mitochondria 2 h after treatment.[78] PC 4 PDT induces cell apoptosis and necrosis by photodamaging two antiapoptotic proteins Bcl-2 and Bcl-Xl. These proteins interacts with mitochondrial permeability transition pore complex and governs mitochondrial death pathway partially through controlling cytochrome C release. To test whether Pc 4 GoMe can enter mitochondria, confocal microscopy was applied to track Pc 4 intracellularly (**Figure 3.8A**). We compared the overlap of Pc 4 and mitochondria channels in the treatment of Pc 4, Pc 4 GoMe or MBA Pc 4 GoMe, and found that the orange signals in both Pc 4 GoMe and MBA Pc 4 GoMe were significantly stronger than that in free Pc 4 treated cells. Among these groups, MBA Pc 4 GoMe showed the highest accumulation in mitochondria. Since the loss of mitochondrial membrane potential ($\Delta\Psi m$) is a critical step for cytochrome C release,[79] we monitored the $\Delta\Psi m$ change quantitatively with JC-1 dye by measuring the ratio of the red

fluorescent intensity to green fluorescence intensity. JC-1 dye can selectively enter mitochondria, and exist in either aggregation or monomer form depending on the health status of mitochondria: If the mitochondria are in the healthy form, mitochondrial membrane potential will maintain a high level and JC-1 stays in aggregation form and displays red fluorescence; otherwise, JC-1 will be in form of monomer and show green fluorescence. After PDT for cells treated with 1 μM Pc 4, the ratio of JC-1 aggregation form to JC-1 monomer form decreased from 14.81 to 5.64 in free Pc 4 treated cells, while this ratio for cells treated with Pc 4 GoMe dropped to 9.84, indicating that mitochondria was damaged in response to PDT (**Figure 3.8B and C**).

Synergistic effects of PDT and PTT on the viability of cancer cells

To validate the direct cytotoxic effect of PTT and PDT, a live/dead staining assay was carried out on cells after exposure to PDT, PTT, or the combination of PDT and PTT. The ethidium homodimer-1 in the kit, an indicator of loss of plasma membrane integrity, can distinguish between dead (Red) and living (Green) cells. **Figure 3.9A-H** represented the acute consequence of PDT and PTT on UMSCC 22A cells that had been incubated with Pc 4, Pc 4 GoMe or MBA Pc 4 GoMe for 3 h. The PDT and PTT were administered by irradiating cells with a 660 nm laser and the 808 nm laser, respectively. Neither control cells nor free Pc 4 treated cells show noticeably cell death in response to the PDT or the combination of PDT and PTT (**Figure 3.9A and B)**. Pc 4 GoMe and MBA Pc 4 GoMe treated groups also did not increase the cell death in response to PDT (**Figure 3.9C-F**). It might be because a short period after PDT is not sufficient to

generate enough pro-apoptotic factors.[80] PTT can kill cancer cells more rapidly as shown in **Figure 3.9G and H**. Pc 4 free drug did not show dual laser induced cytotoxicity, while GoMe eradicated cancer cells more efficiently in response to dual laser suggesting a PTT and GoMe dependent mechanism for cell killing.

To further evaluate the synergistic effects of PDT and PTT in Pc 4 GoMe, we tested the PDT/PTT effect on UMSCC 22A and A 2058 cells using MTT cell viability assay. In this experiment, skin cancer and head and neck cancer cells were chosen due to the practical clinical application of Pc 4 as mentioned earlier. The cytotoxicity of Pc 4 GoMe or MBA Pc 4 GoMe on A 2058 or UMSCC 22A without any photoirradiation was negligible at Pc 4 concentration ranging from 25 to 500 nM, suggesting low side effects and high compatibility (data not shown). With the PDT alone, Pc 4 killed 64% UMSCC 22A cells and 59% of A 2058 cells at 500 nM under 200 mJ/cm^2 laser irradiation. At the same Pc 4 concentration, Pc 4 GoMe killed about 30% cells, which was less effective compared to free Pc 4. MBA Pc 4 GoMe showed similar cell killing effect to free Pc 4 in UMSCC 22A (**Figure 3.9I**) and A 2058 cells **(Figure 3.9K)**. Taking together the enhanced cellular uptake of MBA Pc 4 GoMe, we can conclude that MBA induced the accumulation of MBA Pc 4 GoMe inside sigma 2 overexpressing cancer cells and led to stronger PDT effect.

Next, we tested if the combination of PDT and PTT shows synergistic effect and if the sequence of two therapies matters in killing cancer cells. **Figure 3.9J** showed that at low concentration, Pc 4 GoMe treated cells showed almost no cell killing if applied PTT first followed by PDT, while MBA Pc 4 GoMe was

able to kill 38% of cancer cells. But if PDT was applied first and followed by PTT, Pc 4 GoMe dramatically increased its efficacy. Surprisingly, MBA Pc 4 GoMe was able to kill around 95% of cells even at low concentration if cells were first receiving PDT followed by PTT (**Figure 3.9J)**. In A 2058 cells, we only test the PTT followed by the PDT therapy **(Figure 3.9L)**. With this combination MBA Pc 4 GoMe was able to achieve an 83% of cell death, which was superior to Pc 4 GoMe or Pc 4. Such cytotoxicity results clearly proved the advantages of combination of PDT and PTT in treating various cancer cells, especially at the sequence of application with PDT followed by PTT. We speculate that when applying PTT first, GoMe generates high temperature that may exclude some oxygen out of the cancer cell environment, thus greatly reduces of PDT effect. The sequence that PDT followed by PTT can cause remarkable cell death due to the direct interaction of heat with PDT affected the tumor cells. In addition, if applied *in vivo*, it is expecting that the sequence is more important as severe tumor hemorrhage would occur due to the initial heat from PTT which hampers the efficacy of PDT.

***In vivo* antitumor efficacy**

To evaluate the *in vivo* antitumor effect of GoMe, we divided UMSCC 22A bearing nude mice into 6 groups: saline, Pc 4 with PDT, Pc 4 GoMe with PDT, MBA Pc 4 GoMe with PDT, Pc 4 GoMe with dual photoirradiation and MBA Pc 4 GoMe with dual photoirradiation. All the treatments were well tolerated as mice bodyweight remained the same throughout the whole period (**Figure 3.10A**). Tumors in control group increased by 15 times compared to their sizes at the

beginning of the treatment. Comparing to the control, the mice treated with Pc 4 GoMe or MBA Pc 4 GoMe alone with PDT slowed the growth of tumor, indicating an inhibited tumor progression **(Figure 3.10 B-E**). It has been reported that tumor that survived from PDT will start to regrow in 4-5 days after PDT or 6-7 days after the combined PDT and hyperthermia therapy.[81] Surprisingly, Pc 4 GoMe or MBA Pc 4 GoMe coupled with dual laser irradiation completely eradicated the tumor, and tumors failed to recur over 28 days post treatment, (**Figure 3.10B and C**). There were no significant difference between MBA Pc 4 GoMe and Pc 4 GoMe after dual laser irradiation. **Figure 3.10C** showed that Pc 4 alone with PDT, MBA-Pc 4 GoMe with PDT, and Pc 4 GoMe with PDT achieved 64.4%, 91.04%, and 58.56% tumor growth inhibitory effect, respectively. In contrast, MBA-Pc 4 GoMe coupled with dual laser treatment achieved over 99% tumor growth inhibitory effect.

Histology were carried out on the tumors (**Figure 3.11A**) and livers (**Figure 3.11B**) of the mice with different therapies. Tumor tissues were isolated and examined with H&E staining. There was clear necrosis or apoptosis sign in the tumor tissues from the dual laser treatment compared to the control, and we did not observe liver damage or inflammation lesion, suggesting the liver function was not hampered by MBA Pc 4 GoMe.

CONCLUSION

For currently available cancer therapy, PDT is widely used as an auxiliary strategy to enhance chemotherapy or radiotherapy. As early as 1988, there are abundant studies reported that the combination of chemotherapy and PDT

together would lead to an enhanced antitumor effect in murine model.[82] However the drawbacks of PDT in heavily relying on oxygen level and inability to eradicate cancerous cells failed to prevent the recurrence of tumor. Recently studies have been practiced to combined PDT with PTT using various nanocarriers to achieve higher potency against cancer cells. The synergistic combination can be achieved by co-administering gold nanoshell together with porphyrin,[83] or by combination of chlorin e6 and poly(dopamine).[84] Despite of the progress, more effects are needed to enhance the synergistic effect of PDT and PTT. In this study, we have developed a sigma 2 receptor targeted Pc 4-loaded nano-carrier for photodynamic therapy and photothermal therapy. The PDT effect can be enhanced by regulating the PS distribution and accumulation inside cancerous cells. With the combination of PTT, the cancer cells were killed over 95% *in vitro* and *in vivo* experiment showed complete cancer cell eradiation after the dual laser therapy. Additionally, the active targeting to sigma 2 receptor overexpressing cancer cells further amplify the therapeutic effect. This nano-carrier is good in relieving the heavy burden of PDT on oxygen levels and will not confer any cross-resistance if any other adjuvant therapy is applied.

MATERIALS AND METHODS

Materials

Terraethylorthosilicate (TEOS), (3-mercaptopropyl)trimethoxysilan) (MPTMS), hexadecyltrimethyl ammonium bromide (CTAB), sodium hydroxide (NaOH), pluronic®F-127, 9,10-dimethylanthracene (DMA), tween-80, Ammonium nitrate, methanol, gold chloride trihydrate, cysteamine hydrochloride, 2,2-dipyridyl

disulfide, triethylamine (TEA), glutathione (GSH), 4-mercaptobenzoic acid (MBA), thiazolyl blue tetrazolium bromide (MTT) and sodium borohydride ($NaBH_4$) were purchased from Sigma-Aldrich. PEG2000-SH was purchased from Laysan Bio. Maleimide -PEG-NH_2 (Mw=3400) was purchased from Creative PEGworks. Ethanol and acetic acid were acquired from Fisher Scientific. Silicon phthalocyanine Pc 4 was obtained from NIH. Live and dead staining kit, SOSG was obtained from Thermofisher Scientific. JC-1 Mitochondrial Membrane Potential Assay Kit was purchased from Cayman chemical.

Transmission Electron Microscopy (TEM) was conducted on a Hitachi H8000 at an acceleration voltage of 200 KV. Scanning electron microscopy (SEM) was conducted on a Zeiss Ultra plus FESEM at 6 KV. UV-vis spectrum was obtained with a DU UV/Vis 650 (Beckman). ^{1}H-NMR was conducted in a Bruker Avance III HD 300. Fluorescent Microscopy images were obtained with an Olympus IX81 fluorescence microscopy. Confocal microscopy images were obtained with a Carl Zeiss LSM 700. Flow cytometry was conducted in a Beckman coulter FC500 flow cytometer.

Synthesis of PC 4 loaded GOME

MSN and gold nanoparticles were synthesized as described.[69] Pc 4 was dissolved in DMSO at 10 mg/ml and mixed with MSN at 5/100 weight ratio. After the overnight stirring, un-encapsulated Pc 4 was removed by centrifugation and followed by twice washing with H_2O. To conjugate Au nanosphere to MSN, 800 µg of Pc 4 MSN was reacted with 2 nmol AU-PDA through thiol-disulfide bond exchange reaction for 24 h and Pc 4 loaded GoMe was purified by washing with

H_2O twice. PC 4 loading content was determined by fluorescent plate reader (M2, Molecular device) with excitation at 630 nm and emission 670 nm. The total loading P4 amount was determined by triple washing in DMSO to completely dissolve the encapsulated drugs with extensively sonicating.

Synthesis of polymer SH-PEG-MBA

MBA was conjugated with Mal-PEG-NH_2 through EDC/NHS reaction. MBA (5 mg in 0.4 mL DMSO) was added to EDC/NHS solution (2 equiv of MBA, 0.1 M MES pH 6) and allowed for activation at r.t for 30 mins. Mal-PEG-NH_2 (20 mg, 5.71 μM) was dissolved in DMSO/ pH 7.4 buffer. MBA activated solution (1.74 mg) was added to Mal-PEG-NH_2 solution above. The reaction was carried out at r.t for 24 h. Crude product was purified by dialysis for 24 h in DMSO followed by dialysis in ddH_2O for 24 h with a dialysis membrane (MWCO=1000 Da). The final product was collected through lyophilization and stored at -20 ºC until use. Polymer conjugation was confirmed by ^{1}H-NMR using $CDCl_3$ as the solvent and the reaction yield was quantified with TNBSA assay by calculating the reduced amine in the polymer.

Preparation of PC 4 GOME coated with SH-PEG-MBA

PC 4 GoMe was well dispersed in ddH_2O at 1 mg/ml. SH-PEG-MBA was dissolved in H_2O at the concentration of 2 mg/ml and mixed with PC 4 GoMe (1:2, w/w). The mixture was stirred and reacted for 24 h at r.t. MBA conjugated PC 4 GoMe (MBA-PC 4 GoMe) was isolated from unreacted SH-PEG-MBA by centrifugation followed by washing with H_2O twice. Final product was dispersed in PBS or H_2O at 1 mg/ml and stored at -4 °C prior for use.

Characterization of MBA PC 4 GoMe

GoMe was diluted at the concentration of 20 µg/ml in H_2O and 3 drops of the suspension was loaded onto a 200-mesh copper grid coated with formvar. Air-dry the grid and analyzed with TEM (Hitachi) using 200 K acceleration voltage. GoMe was suspended in ethanol and drop on the silicon wafer. Air-dry the wafer and analyzed with SEM with 6 KV under 200,000X magnification. The UV/vis spectrum was recorded with a DU650. The size was determined with dynamic light scattering and surface charge was recorded with a Malvern Nano-ZS Zeta Sizer.

Photothermal response

Pc 4 GoMe was diluted to a serial of concentrations with PBS and their UV-Vis spectra were recorded. The Pc 4 GoMe suspension with the volume of 200 µL in 1.5 mL eppendorf tube was irradiated with an 808 nm laser for 10 min (Scorpius D-700 laser, 2.83 W/cm^2). The temperature of the suspension was monitored simultaneously with a FLIR i7 thermal imaging camera and recorded every 30 sec. The cool period followed by irradiation was recorded up to 20 mins or until it completely decreased to r.t.

In vitro release of Pc 4 from Pc 4 GoMe

To test the responsiveness of Pc 4 GoMe to intracellular high reducing environment, PBS plus 10 mM GSH were employed. Due to the solubility limitation of Pc 4, 1% tween was added to above solutions. Two hundred microliter of Pc 4 GoMe (at 1 mg/mL MSN) was loaded to 1.5 mL eppendorf tube and diluted with 1 mL PBS or GSH supplemented PBS. At each time point,

samples were centrifugal at 16000 rcf for 10 mins and all the supernatant was transferred out and 1 mL of fresh media was supplemented in.

To stimulate the laser trigger of Pc 4 GoMe, Pc 4 GoMe suspension was photoirradiated by NIR 808 nm laser for 10 mins after 24 h suspension in serum containing PBS buffer at 37 °C. The release of Pc 4 GoMe was continued to be monitored for another 24 h. At pre-determined time point, GoMe was centrifuged and all the supernatant was collected. The concentration of Pc 4 was determined by fluorescent plate reader, using the same release buffer as diluting buffer when preparing standard curves for Pc 4.

Stability testing of Pc 4 GoMe

Nanoparticles at the final concentration of MSN at 100 μg/mL were suspended in Dulbecco's Modified Eagle Medium (DMEM) with 10% fetal bovine serum (FBS) at 37 °C. The size of nanoparticles was measured with DLS. To further investigate the integrity of GoMe during the circulation in physiological environment, the release behaviors of Pc 4 GoMe was tested in two release media. GoMe were incubated with PBS containing 10% or 50% of FBS at 37 °C via rotation (Thermoscientific tube revolver, 10 rpm) for different time points varies from 1 h to 48 h. At each time points, the released Pc 4 were collected through centrifugation and determined by a fluorescent plate reader.

Quantification of cellular uptake of GoMe

Cellular uptake of Pc 4 GoMe or MBA Pc 4 GoMe was quantified by flow cytometry and confocal microscopy. Cells were seeded in 12 well plates at 200,000 cells per well and treated with Pc 4, Pc 4 GoMe or MBA Pc 4 GoMe at

the concentration of 1 μM for 0.5 h, 1 h or 2 h. Cells were incubated at 4 °C or 37 °C, respectively. At each time point, cells were washed 3 times with cold PBS to remove un-bounded Pc 4 or Pc 4 GoMe. Cells were collected and fixed in 4% formaldehyde, and examined by FACS.

To further investigate the role of MBA in facilitating the uptake of nanoparticles, the competition assay was carried out and the results were obtained with confocal microscopy. UMSCC 22A cells were pre-incubated with MBA (0.1 mg/mL) for 1 h. Different treatment groups were then added into each petri dish and reached the final Pc 4 concentration of 1 μM. After the co-incubation of 3 h, cells were washed for 3 times and images were taken with Zeiss 710 LM at Pc 4, DAPI and DIC channels.

Subcellular trafficking of Pc 4 GoMe

Subcellular localization of NPs affects the efficacy of a photosensitizer, especially when mitochondria are the critical targets of Pc 4-PDT. Here we used confocal microscopy to investigate the subcellular location of Pc 4 in UMSCC 22A cells. Cells were seeded in 10 mm petri dishes at 200,000 cells per dish, and were allowed to grow overnight. Cells were treated with Pc 4, Pc 4 GoMe or MBA Pc 4 GoMe at the Pc 4 concentration of 500 nM and incubated for 3 h. Cells were washed with PBS for three times and incubated with Mitotracker red FM (100 nM) for 30 mins. Cells were then washed with PBS twice and incubated with Hoechst 33342 (1 μg/mL) for 10 mins. Images were taken immediately with confocal microscopy.

Singlet oxygen detection *in vitro*

In order to investigate the singlet oxygen level upon laser irradiation, two fluorescent dyes N,N-dimethylacrylamide (DMA) and singlet oxygen sensor green (SOSG) were employed. Briefly, Pc 4 or Pc 4 GoMe at the concentration of 112 nM was dispersed in PBS or PBS supplemented with 10 nm GSH, respectively. To create a sink condition, the above media were supplemented with 0.5% tween 80. Stock solution of DMA was prepared in DMF at concentration of the 250 μM. Three milliliter Pc 4 or Pc 4 GoMe was mixed with DMA at the final concentration of 16.7 μM and kept stirring at r.t. The mixture was kept in vial with a cap opened and was irradiated with a 660 nm laser continuously for 10 mins. Two hundred microliter was sampled out every minute. The fluorescent intensity decay of DMA was analyzed (ex: 375 nm, em: 435 nm). Fluorescent intensity at 0 mins was defined as the mixture of Pc 4 with DMA without NIR irradiation.

Fluorescent dye singlet oxygen sensor green (SOSG, Thermofisher scientific) were also applied to determine the singlet oxygen level. Briefly, Pc 4 or Pc 4 GoMe at the Pc 4 concentration of 1 μM was suspended in PBS containing 1% tween 80. One hundred microliter suspension was added to a black 96 well plate (Costar), followed by the addition of 20 μl SOSG solution (stock solution prepared in methanol and diluted with HBSS buffer with a final concentration at 50 μM). Each plate was irradiated with a 660 nm laser (18 mW/cm^2) for 2, 6, 8 or 10 mins and the control group was employed with the same amount of nanoparticles or Pc 4 without laser irradiation. The oxidized SOSG was

determined by measuring the fluorescent intensity at 525 nm upon the excitation at 504 nm. The full spectrum was recorded from 500 nm to 600 nm when excited at 490 nm with cutting off at 515 nm. SOSG assay was further employed to examine the Pc 4 responsiveness to GSH triggering. Pc 4 GoMe was incubated with 10 mM GSH for 3 h prior to NIR irradiation, and the fluorescent intensity at 525 nm and full spectrum were recorded as described above. All experiments were carried out in triplicate.

SOSG assay was also employed to investigate the intracellular singlet oxygen production. UMSCC 22A cells were seed in 12 well plate. When cell reach nearly confluence, Pc 4 GoMe, MBA Pc 4 GoMe or Pc 4 at the Pc 4 concentration of 1 μM was added to each well and allowed to incubated for 16 h. Cells was then washed with PBS twice and incubated with SOSG solution for 2 h (HBSS solution at concentration of 1 μM). Cells were irradiated for 10 mins (660 nm, 18 mW/cm^2), followed by imaging with fluorescent microscope with the GFP channel and DIC channel.

Measurement of mitochondrial membrane potential

Changes of ΔΨm were monitored with JC-1 dye. Cells were seeded in 96 well with a black 96 well plate and allowed to reach the confluence of 80% before the experiment. Cells were co-incubated with Pc 4, Pc 4 GoMe at the Pc 4 concentration of 200 nM or 1 μM for 16 h. Media was then replaced and cells were irradiated with a 660nm laser at 200 mJ/cm^2. After 5 h incubation, cells were stained with JC-1 dye diluted media (10 μg/mL) for 30 mins. Afterwards, cells were washed twice with assay buffer and the fluorescent intensities at the

excitation of 485 nm and the emission of 525 nm as well as the excitation at 535 nm and emission of 590 nm was recorded. Control plate was prepared in the same method except without receiving laser irradiation.

Cell viability upon PDT and PTT treatment

To visualize the direct cytotoxicity effect of PTT or the combination of PDT and PTT on cancer cells, a live/dead staining kit was employed. UMSCC 22A were seeded in a 24 well plate at the density of 200,000 cell per well and allowed for overnight incubation. Cells were treated with Pc 4, Pc 4 GoMe or MBA Pc 4 GoMe containing media (at the Pc 4 concentration of at 100 nM) for 3 h. After the treatment, the old media were replaced by fresh media. Subsequently, cells received different photoirradiation treatments including: 1) 660 nm PDT at 200 mJ/cm^2, 2) 808 nm PTT for 10 mins, 3) firstly irradiated with PDT followed by PTT. Media were removed and cells were stained with live/dead staining kit in PBS for 30 mins according to manufacturer's instruction. Images were taken immediately with a fluorescent microscope with FITC, Texas red and DIC channels.

Cell viability after receiving PDT and PTT treatment was quantitatively evaluated by MTT assay. UMSCC 22A and A2058 cells were seeded at density of 20,000 per well in 96 well plates with either transparent or black wells and incubated at 37 °C under 5% CO_2 overnight. Pc 4, Pc 4 GoMe or MBA Pc 4 GoMe at various concentration were incubated with cells in dark for 3 h. After twice washing with PBS, cells received photoirradiation accordingly. For PDT treatment groups, cells were seeded in black well clear bottom 96 well plates and

irradiated under the laser (λ=660 nm, 200 mJ/cm^2). For PTT treatment groups, cells were seeded in clear 96 well plates and irradiated under the laser (λ=808 nm, t=10 mins). For the combination therapy of PDT and PTT, cells were either first receiving PDT followed immediately with PTT, or first receiving PTT followed by PDT. After the photoirradiation, cells were further incubated in dark for 48 h. Afterwards, the old media were replaced with 100 μL fresh media containing 1 mg/mL MTT reagent and continued to incubate for 4 h. The formed MTT crystal was dissolved with a stop solution and the finally optical density of the medium was measured using a microplate reader (ELX808, Bio-Tech Instrument, Inc) at λ = 595 nm.

Combination therapy *in vivo*

All animal experiments were conducted in accordance with NIH regulations and approved by the Institutional Animal Care and Use Committee of the University of South Carolina. Female athymic mice at 6 to 8 weeks (nu/nu) were obtained from Jackson laboratory. UMSCC 22A cells were injected subcutaneously into both flanks of mice (2 million cells per implant). The tumor volume was measured by a digital capillary and calculated according to the following formula: Tumor volume = (tumor length) × (tumor width) ^{2}/2. When the tumor reached to 50 mm^3, mice were divided into 6 groups: (1) saline; (2) Pc 4 with PDT laser at the dose of 50 J/cm^2, (3) Pc 4 GoMe was injected into tumor. After the injection of 1 h, mice were treated with PDT at the dose of 50 J/cm^2 for the duration of 25 mins. (4) Pc 4 GoMe were injected into tumor. After the injection of 1 h, mice were treated with PDT at the dose of 50 J/cm^2. Immediately,

the mice were then anesthetized and received PTT for 2 mins (808 nm, 2.8 W/cm^2). (5) MBA Pc 4 GoMe was injected into tumor. After the injection of 1 h, mice were treated with PDT at the dose of 50 J/cm^2 (6) MBA Pc 4 GoMe was injected into tumor. After the injection of 1 h, mice were treated with PDT at the dose of 50 J/cm^2. Immediately, the mice were anesthetized and received PTT for 2 mins (808 nm, 2.8 W/cm^2). Pc 4 dose was kept at 0.5 mg/kg mice. At the end of 28 days, mice were sacrificed and tumors were harvested and weighed. The isolated tumors were fixed in 10% neutralized formalin solution and changed to a gradient of sucrose solutions until they sink down in the sucrose solution before embedding with OCT. Tumor was sliced into 10 μm thickness and followed with standard H&E staining protocol. The inhibition effect of tumor growth was calculated based on the following equation: inhibition effect I (%) = (tumors weight in the groups of saline - tumors weight in the treatment group)/ tumors weight in the groups of saline × 100%.

Acute cytotoxicity of Pc 4 GoMe was evaluated in UMSCC 22A bearing mice. After injection of the dose of Pc 4 GoMe or MBA Pc 4 GoMe, mice were sacrificed in the next 24 hours. All the organs were collected and evaluated through H&E stain histology for tissue sections.

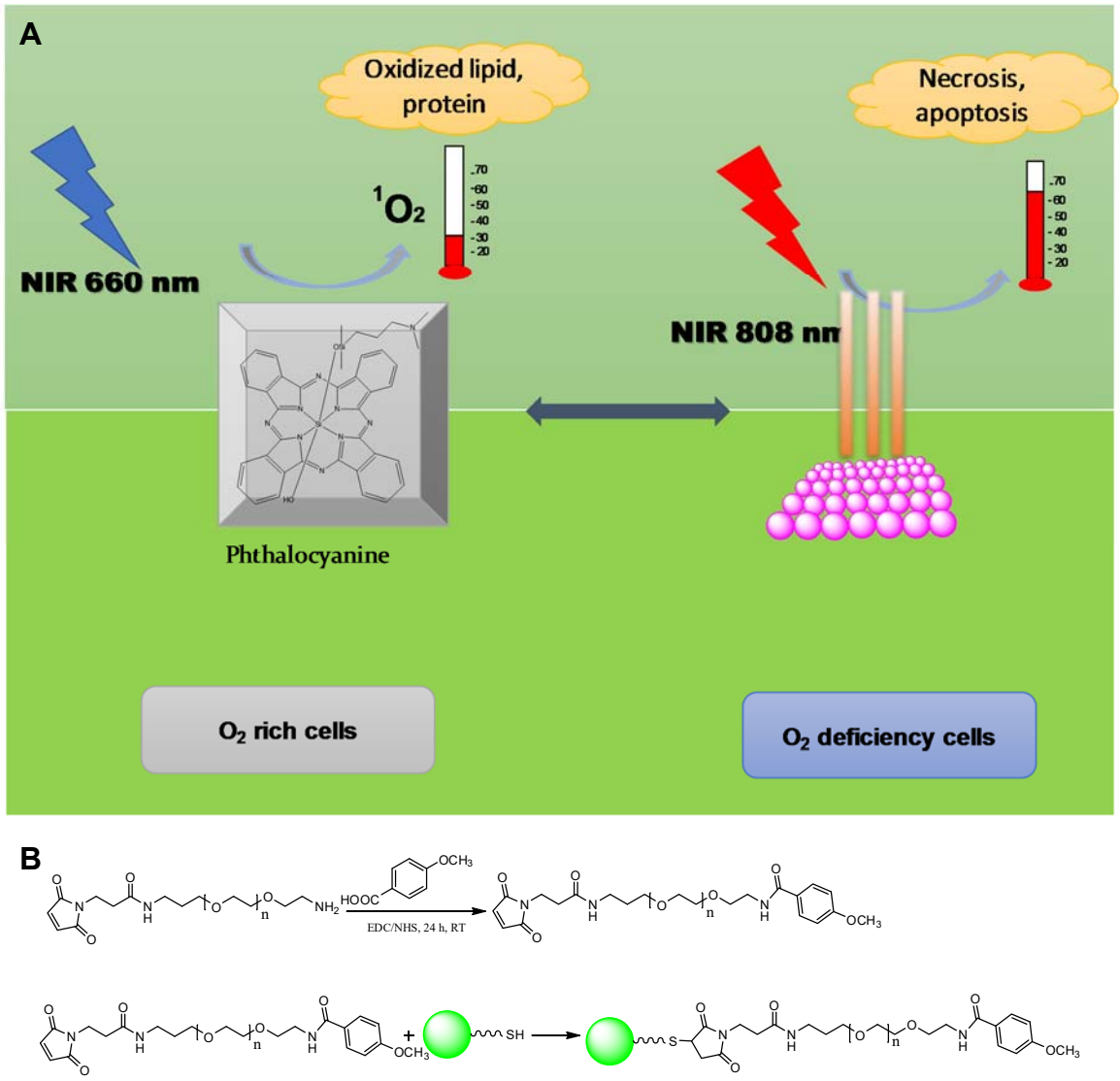

Figure 3.1 The scheme for the combination therapy of PDT and PTT using MBA PC 4 GoMe (A) and the synthesis process of conjugating MBA to GoMe (B) (Green ball-GoMe).

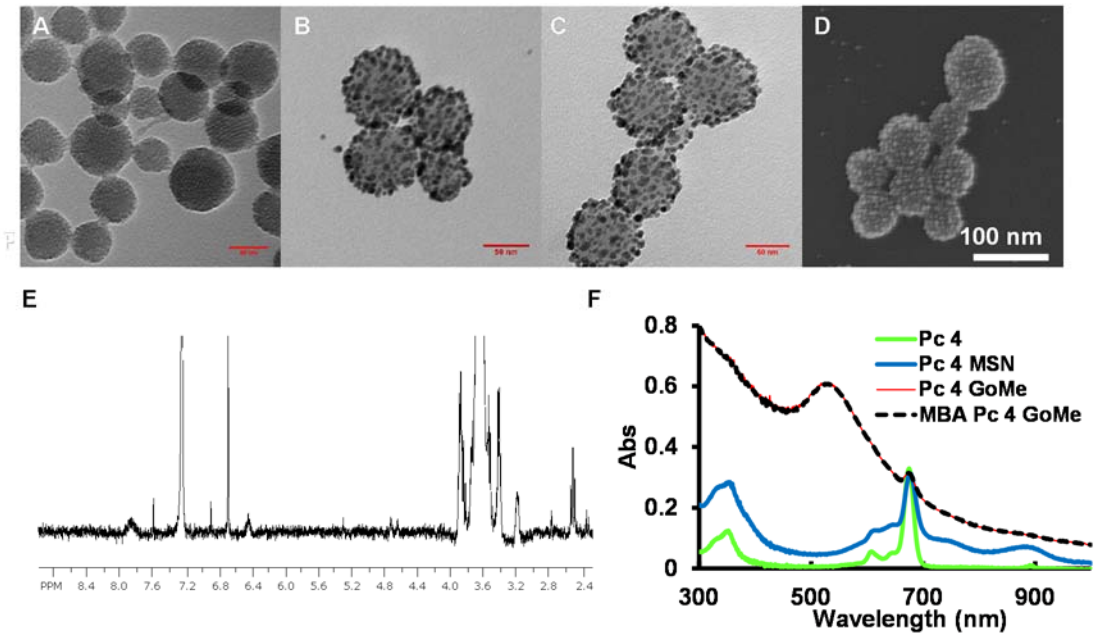

Figure 3.2 Physical characterization of MBA Pc 4 GoMe. Transmission electron microscope images of Pc 4-MSN (A), Pc 4 GoMe (B), MBA Pc 4 GoMe (C), Scanning electron microscope image of PC 4 GoMe (D). (E) ^{1}H-NMR of Mal-PEG-MBA in $CDCl_3$. (F) The UV-Spectra of Pc 4, Pc 4-MSN, PC 4 GoMe and MBA-Pc 4 GoMe.

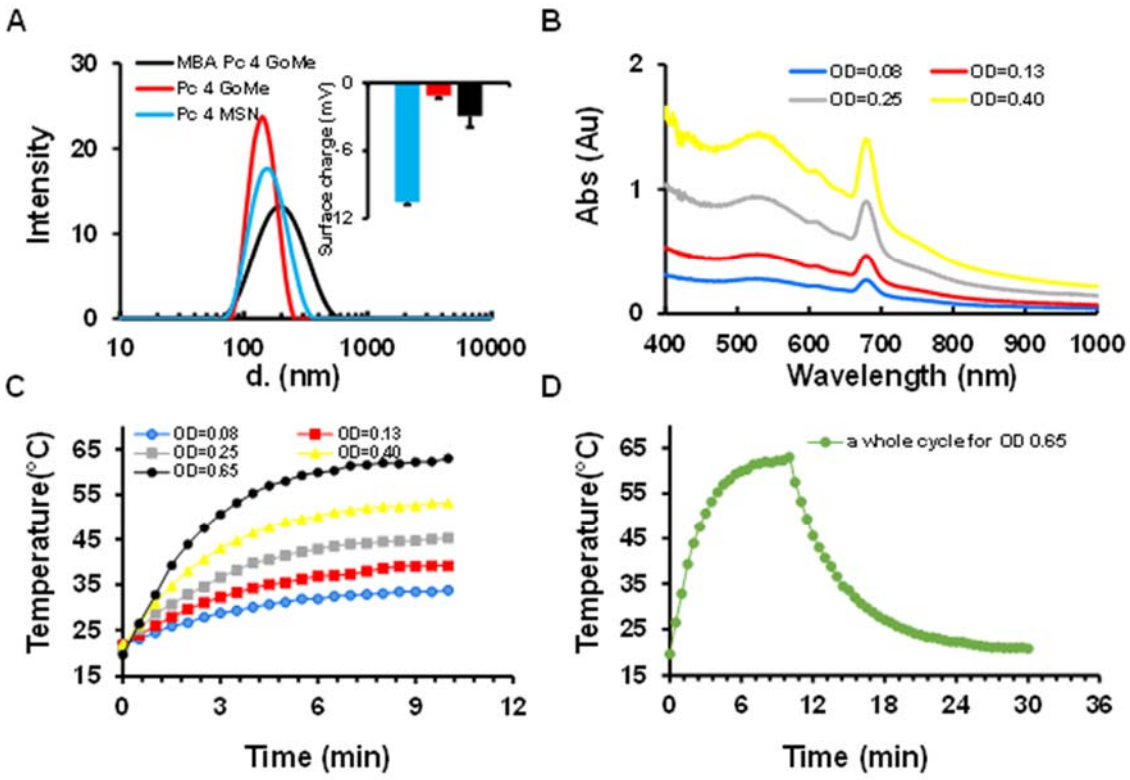

Figure 3.3 Hydrodynamic size and surface charge of Pc 4 GoMe and its photothermal response. (A) Hydrodynamic size of MBA Pc 4 GoMe was determined by dynamic light scattering, and surface charge was monitored by Malvern nano sizer. (B) UV-Vis spectra of PC 4 GoMe at different concentrations. (C) Photothermal response of Pc 4 GoMe at different concentrations coupled with the 808 nm laser. (D) A heating and cooling cycle of PC 4 GoMe at OD = 0.65 in PBS.

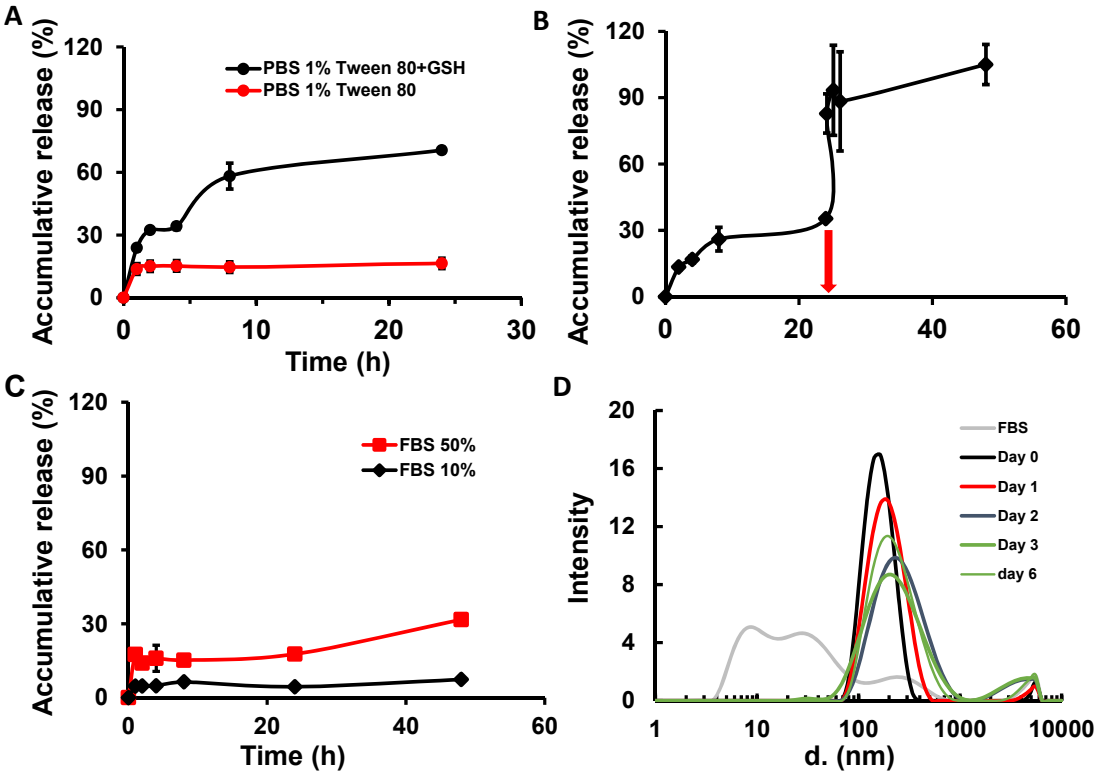

Figure 3.4 Pc 4 GoMe release and colloid stability. (A) The Pc 4 release kinetics of Pc 4 GoMe. (B) The release of Pc 4 was in response to laser irradiation at 808 nm. Arrow represents the time point when the laser was applied. (C) Stability of Pc 4 GoMe in serum containing media. (D) Hydrodynamic size changes of Pc 4 GoMe after incubated with 10% FBS for up to one week at 37 ºC.

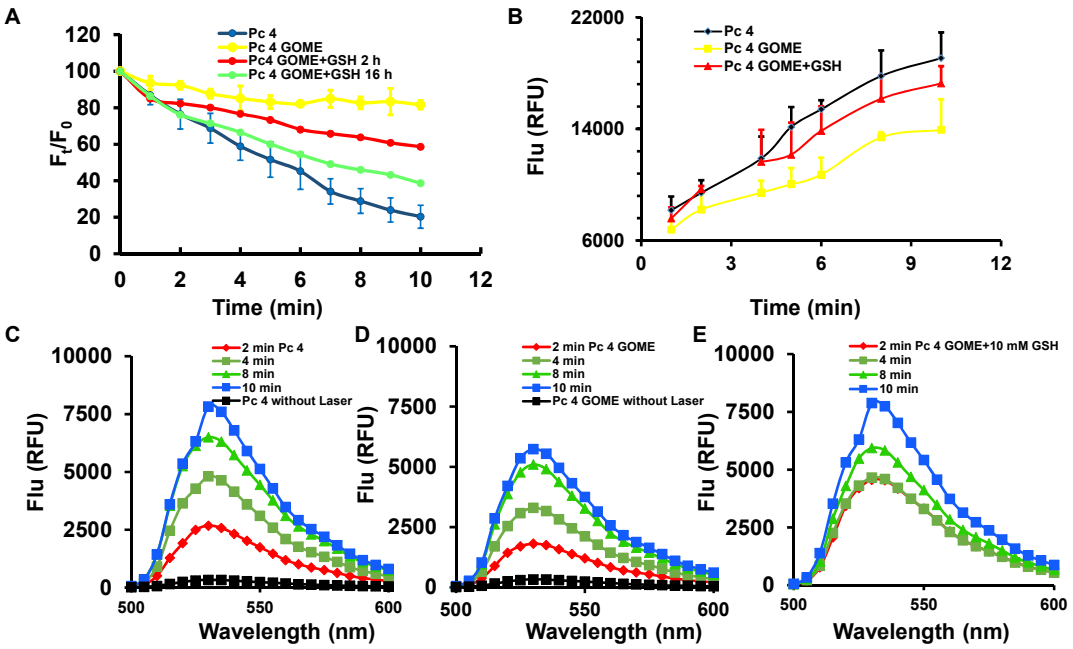

Figure 3.5 Determination of singlet oxygen generation upon NIR 660 nm irradiation. (A) DMA was used to determine the generation of singlet oxygen from Pc 4 GoMe after the co-incubation with GSH 10 mM. (B) The fluorescence intensity change of SOSG was used to determine the release of Pc 4 from Pc 4 GoMe after the co-incubation with GSH 10 mM. (C) The spectra of SOSG in solution with Pc 4 with photoirradiation over time. (D) The spectra of SOSG in solution with Pc 4 GoMe with photoirradiation over time. (E) The spectra of SOSG in solution with Pc 4 GoMe supplemented with 10 mM GSH after photoirradiation over time. Both Pc 4 and Pc 4 GoMe solution mixed with SOSG without photoirradiation were served as control.

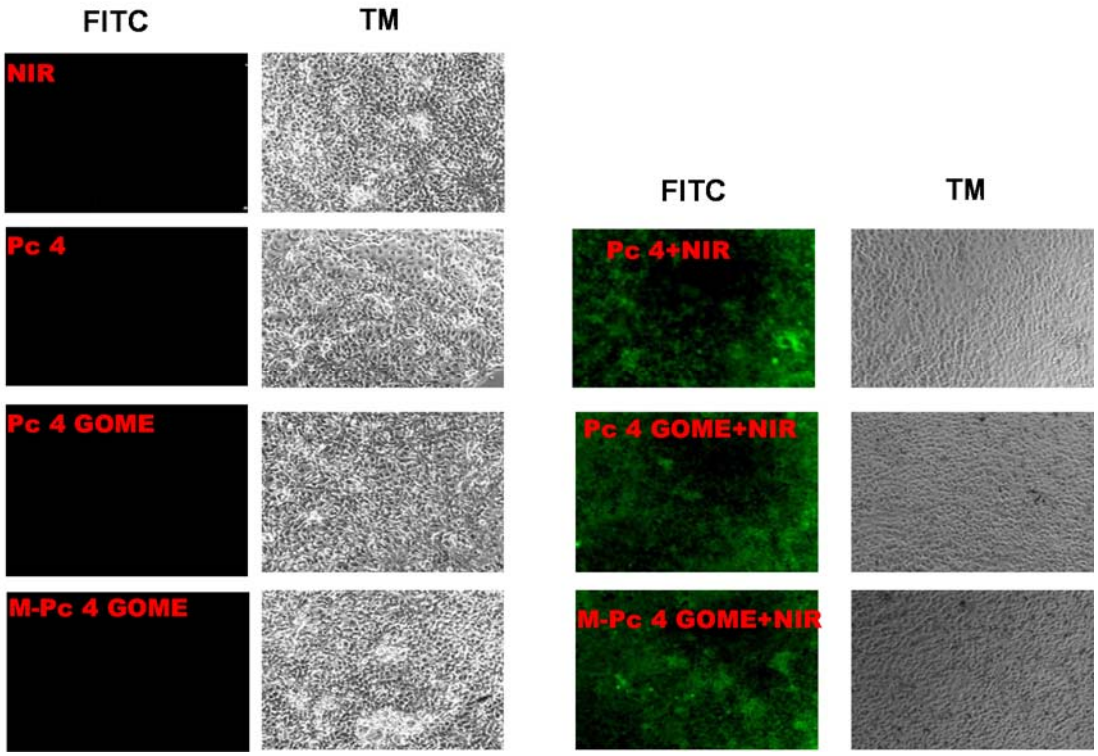

Figure 3.6 SOSG singlet oxygen detection in UMSCC 22A cells treating with Pc 4, Pc 4 GoMe and MBA-Pc 4 GoMe with or without a 660 nm laser irradiation (Green-the fluorescence of SOSG after reacted with $^1O_2$).

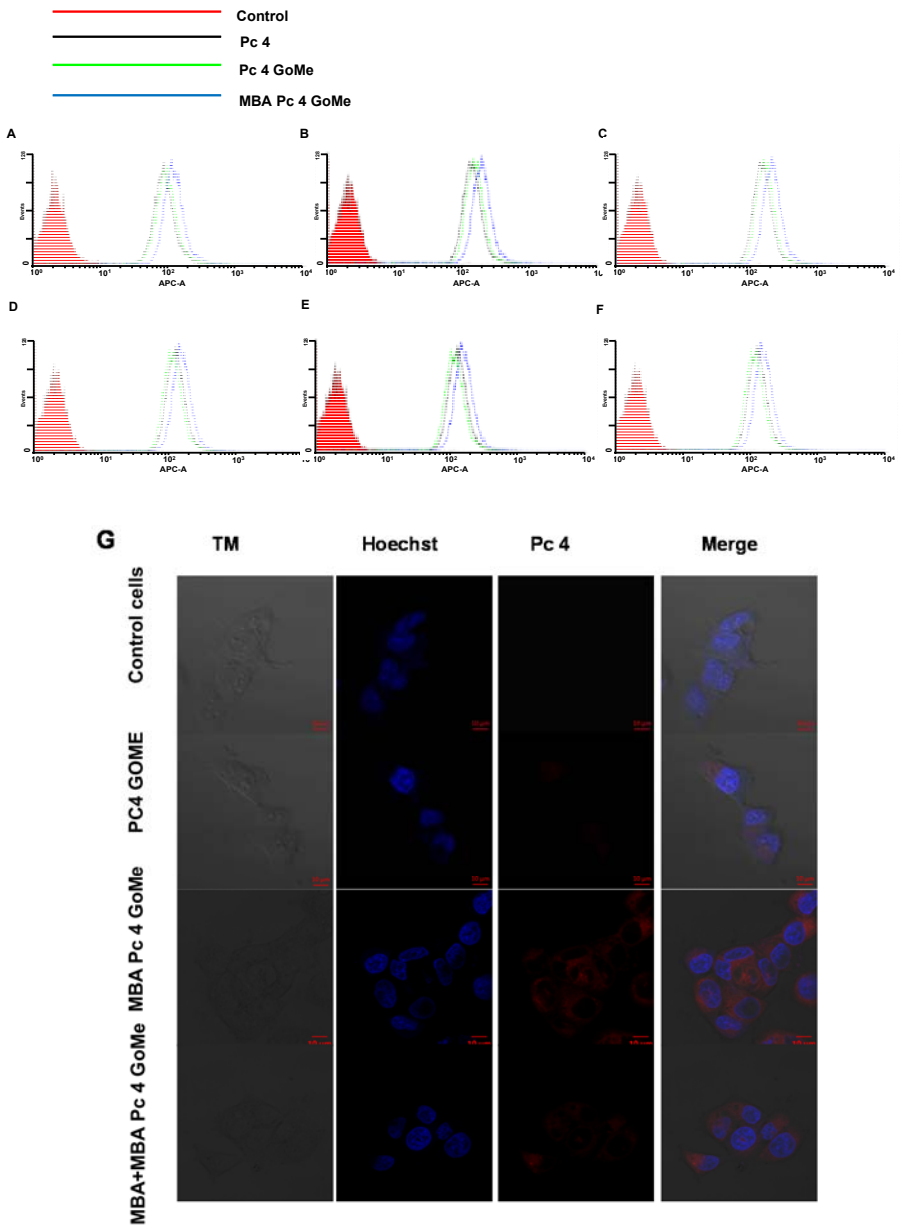

Figure 3.7 The uptake of nanoparticles in UMSCC 22A cells. FACS of UMSCC 22A cells treated with free Pc 4, Pc 4 GoMe and MBA Pc 4 GoMe at 37 °C for 0.5 h (A), 1 h (B), and 2 h (C). FACS of UMSCC 22A cells treated with free Pc 4, Pc 4 GoMe and MBA Pc 4 GoMe at 4 °C for 0.5 h (D), 1 h (E), and 2 h (F). (G) Confocal microscopy images of Pc 4, Pc 4 GoMe or MBA-Pc 4 GoMe in UMSCC 22A cells. Hoechst 33342 (blue), Pc 4 (red).

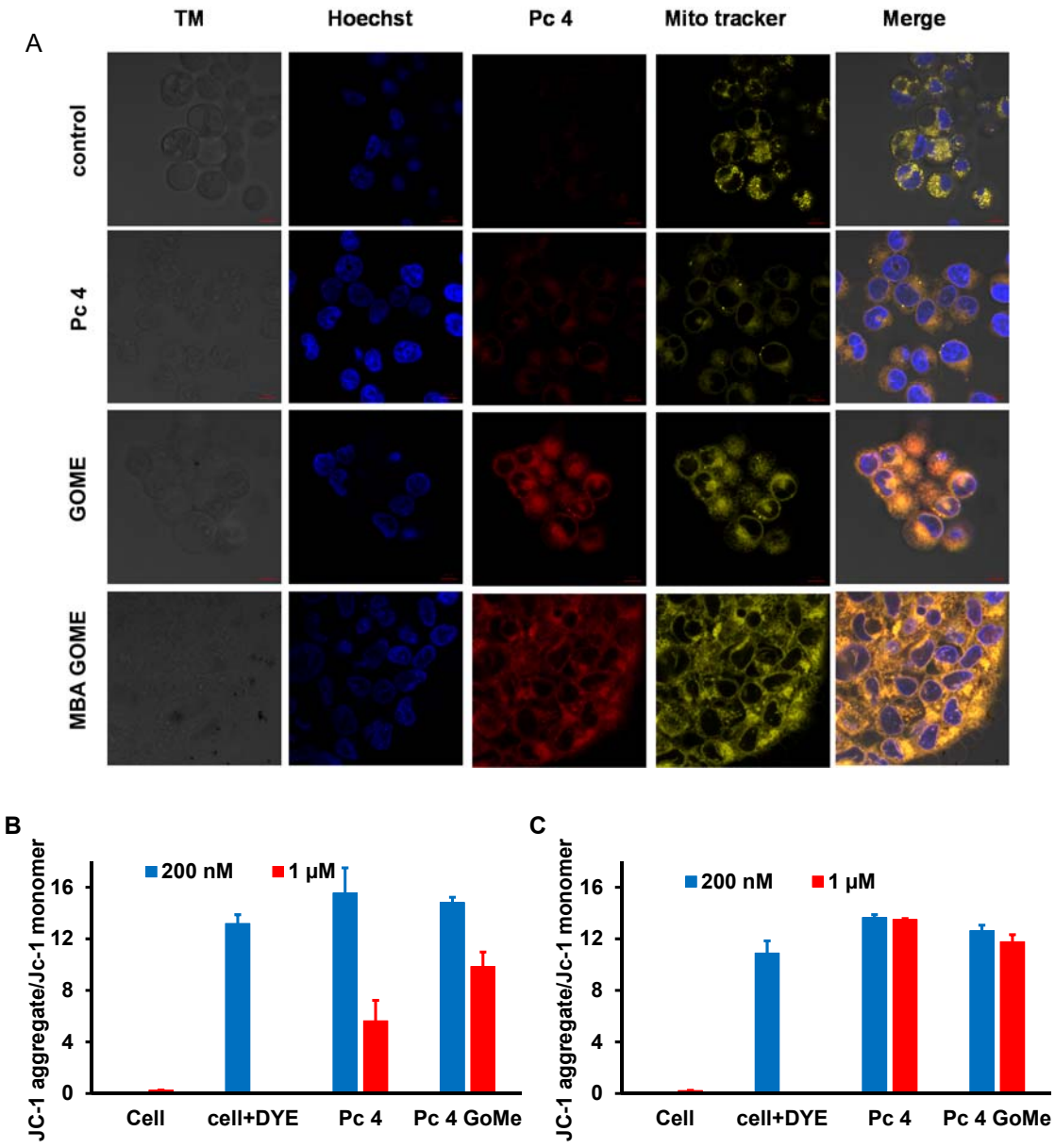

Figure 3.8 Pc 4 GoMe localized in the mitochondria and caused its membrane potential change. (A) Confocal microscope images of UMSCC 22A incubated with Pc 4, Pc 4 GoMe and MBA Pc 4 GoMe at 1 μM and stained with Hoechst 33342 (blue), Mito tracker FM (yellow), Pc 4 (red). (B) JC-1 staining of UMSCC 22A cells treated with Pc 4, Pc 4 GoMe followed by PDT (200 mJ/cm^2). (C) JC-1 staining UMSCC 22A cells treated with Pc 4, Pc 4 GoMe without photoirradiation.

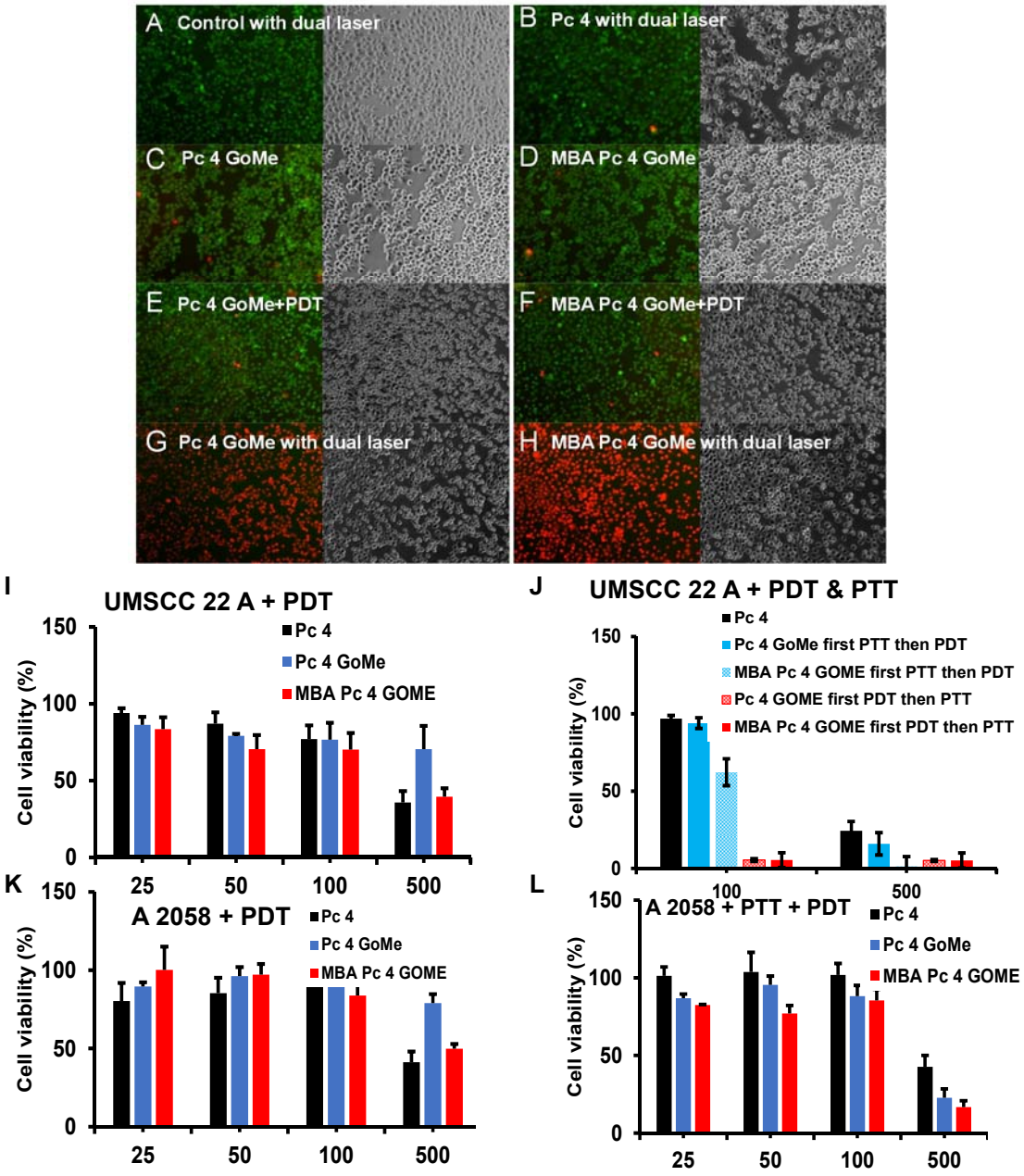

Figure 3.9 Cytotoxic effect of MBA Pc 4 GoMe coupled with PDT and PTT. (A-H) Live/dead staining of UMSCC 22A cells after photoirradiation of PDT (200 mJ/cm^2) or PDT+PTT (2.8 W/cm^2, 10 mins). Cytotoxicity of different treatments coupled with PDT in UMSCC 22A (I) and A 2058 (K). Cytotoxicity of different treatments coupled with PTT and PDT with different sequences in UMSCC 22A (J) and in A 2058 with the sequence of first apply PTT and then PDT (L).

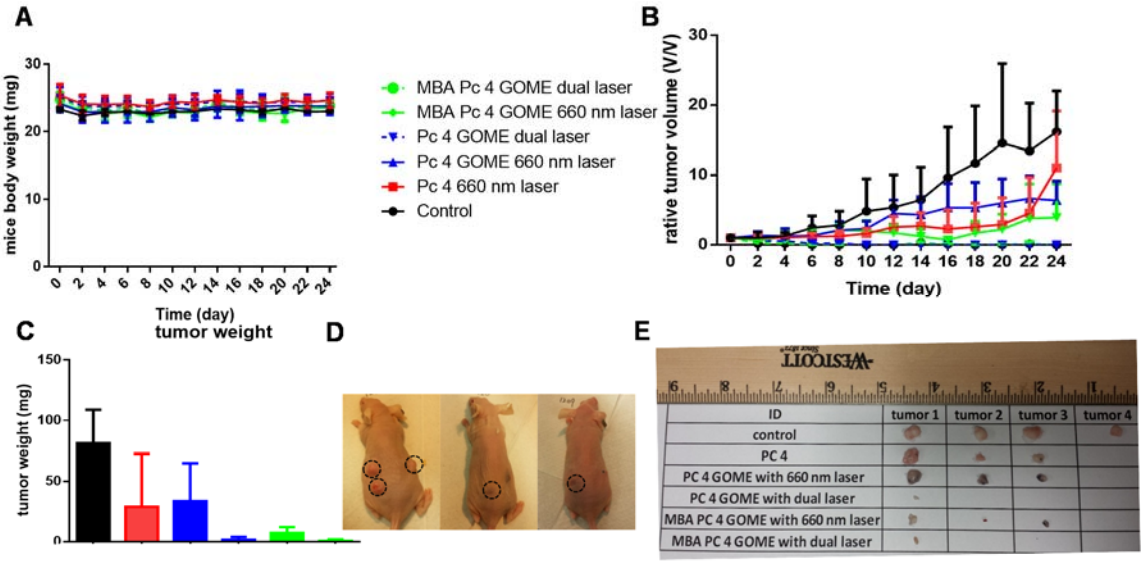

Figure 3.10 Combination therapy of PTT and PDT for UMSCC 22A head and neck cancer *in vivo*. (A) Bodyweight change curves. (B) Tumor volumes change curves. (C) Average weight of tumors in all treatments. (D) Photographs of control mice (left mice), Pc 4 GoMe with dual laser (middle mice), MBA Pc 4 GoMe with dual laser (right mice). (E) Photos of tumors for the 6 treatment groups.

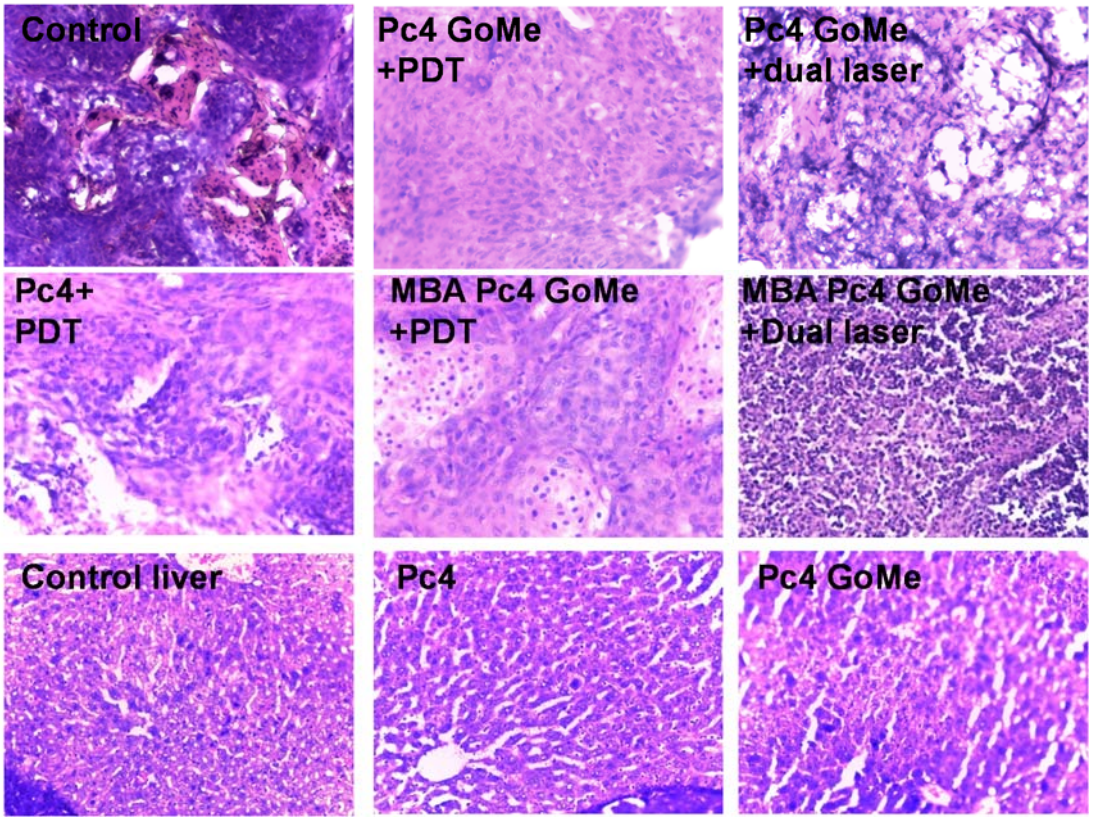

Figure 3.11 Histology analysis of liver and tumor of mice. (A) H&E staining of tumor section of the mice treated with saline, Pc4 + PDT, Pc 4 GoMe + PDT, Pc 4 GoMe + dual laser, MBA Pc 4 GoMe + PDT, MBA Pc 4 GoMe + dual Laser. (B) Liver H&E staining of liver section of mice with different treatments.

CHAPTER 4

Glycol chitosan mediated co-delivery of suramin and doxorubicin for the treatment of breast cancer metastasis

ABSTRACT

Suramin (SM), an anti-angiogenesis agent, has been evaluated in various clinical trials for cancer therapy. However, it was eventually withdrawn due to its narrow therapeutic window and the side effects associated with multiple targets. In this work, we developed a simple but effective system by using a non-toxic dose of suramin together with a chemotherapeutic agents for the treatment of metastatic triple negative breast cancer. Suramin and doxorubicin (DOX) were encapsulated into nanoparticles by gentle gelation with glycol chitosan (GCS) through one step preparation. The formed nanoparticles were small size and uniform range, exhibiting a surprisingly high loading capacity of suramin. *In vitro* experiments proved the effectiveness of nanoparticles in inhibiting cell migration and invasion. The intravenous (i.v) injection of nanoparticles significantly extends the survive rate of animals with breast cancer lung metastasis and greatly reduces the cardiotoxicity compared to the combination of free drugs.

INTRODUCTION

Breast cancer is the most common cancer in women worldwide, while metastasis is the major cause of human cancer death.[85] Metastasis is a complex process that involves the cell invasion from the primary tumor, intravasation and

extravasation in circulation system, and angiogenesis and growth in the distant location.[86] Perhaps the most effective way of treating metastatic cancer is to kill cancer cells before the dissemination from primary foci. However, the clinical deficiency in accurately detecting small tumor mass is a limiting factor for curable cancer treatment. When a breast cancer patient is diagnosed with distant metastasis, the five-year relative survival rate drops from 98.6% to 23.4%.[87] Currently, various treatments are available for patients with different stages of metastasis. There is barely any FDA approved treatment other than prophylactic and vaccination before the diagnosis of circulating tumor cells (CTC). Once a patient is diagnosed with CTC, or even micro-metastasis, surgery or radiation plus systemic therapy will be applied. For high risk patients, metronomic chemotherapy and anti-angiogenesis might be necessary.[86]

Angiogenesis, a hallmark of malignant disease, is a process to form new blood vessels based on the original ones, which is critical for tumor progression. CTCs up-regulate several pro-angiogenic factors, such as vascular endothelial growth factor (VEGF) and basic fibroblast growth factor (bFGF), to adapt to the new tumor microenvironments.[88] The combination of bevacizumab, an inhibitor of VEGF, with paclitaxel/carboplatin significantly increased the median survival month of patients diagnosed with metastatic colorectal cancer or advanced NSCLC in a phase III trial.[89] However, for patients with the late stage of breast cancer, the best treatment so far only provides survival advantages of a few months.[90]

One of the major targets for anti-angiogenesis is the FGF family. FGFs and their receptors play crucial roles in many fundamental processes from embryogenesis to adult life, such as proliferation, differentiation, migration, angiogenesis and wounding healing.[91] Like many other mitogens, FGFs act like a double-edged sword and deregulation of the signaling causes various types of human cancer that arises in different tissues including lung, breast, ovarian and prostate.[91a, 92] Therefore, FGF/FGFRs have been extensively studied as a potential target for cancer treatment. Many selective or non-selective pharmaceutical inhibitors for FGFs and FGFRs have been developed for cancer treatment.[93]

Suramin, a polysulfonated naphthylurea that inhibits VEGF and bFGF, is reported as an anti-angiogenesis agent.[94] Suramin reversed the FGF induced drug resistance at the concentration of 1-17 μM in human prostate PC3 cells in the presence of doxorubicin (DOX).[94f] The combination of suramin and various chemotherapeutic agents have proven effective in various mice models and entered clinical trials. The combination of suramin and paclitaxel inhibited the brain metastatic cancer by injecting suramin at 10 mg/kg and PTX at 10 mg/ml.[94h] The nontoxic dose of suramin with DOX were suggested for the treatment of prostate cancer.[94f, 95] The co-delivery of suramin enhanced the activity of DOX in dogs with spontaneous cancers.[96] In the xenograft prostate mouse model, the addition of suramin to DOX inhibited tumor growth by 60%.[94f] Although suramin has a direct effect on cancer cells, high dose of suramin not only cause cytotoxic effects but also initiate tolerance response.[97] A recent study

showed that chemical conjugates of low molecular weight heparin and suramin which had a higher affinity to the heparin binding domain of $VEGF_{165}$, which significantly inhibited the tumor progression in a SCC-7 tumor bearing mouse model.[94c] However, this mouse model was a xenograft primary tumor model.

In this study, a simple yet effective nanoparticle system is carried out for breast cancer lung metastasis therapy. Suramin and glycol chitosan (GCS) forms the nanoparticle system by electrostatistic effect, and DOX is encapsulated inside. Both suramin and GCS showed inhibitory effect on the migration and invasion of MDA-MB-231 breast cancer cell migration. Suramin at a non-toxic dose was able to enhance the anticancer efficacy of DOX both *in vitro* and *in vivo*. In addition, all of the components in this system are highly biocompatible, easy for large scale fabrication, which make this system very translatable for the metastatic breast cancer treatment.

RESULTS

DOX encapsulated glycol chitosan/suramin (GCS-SM/DOX) NP synthesis

It has been reported that chitosan can form hydrogels with tripolyphosphate (TPP)[98] and alginate.[99] Many factors can affect the size of nanoparticles, especially the TPP to chitosan ratio, pH of the buffer and the ionic strength of the dissolution medium.[98b, 100] As anionic and cationic compounds account for the majority weight of the delivery system, the loading capacity of therapeutic agents will be greatly reduced if they are not an active pharmaceutical ingredient. Moreover, a few reports showed that chitosan was able to form the hydrogel with sodium lauryl sulfate.[101] We came up with the idea

of creating GCS-SM NPs through the gelation process between the sulfate groups on suramin and amine groups on glycol chitosan, where suramin acted as an anionic compartment and glycol chitosan acted as a cationic compartment (**Figure 4.1)**. The relationships among particle size, suramin content in the final formulation, pH of the buffer, as well as the concentration of suramin were shown in **Figure 4.2A-D**. In order to examine the effect of suramin concentration on the nanoparticle size, we fixed the glycol chitosan concentration at 2.5 mg/mL in PBS buffer. With the suramin concentration varying from 25% to 5% (weight ratio to glycol chitosan), the hydrodynamic size of nanoparticle was increased from 220 nm to 277 nm along with the increased PDI (polydispersity index). Next step, we varied the pH of the buffer from 6 to 7.4. The size of nanoparticles was maintained at 210 nm level at pH 6. The particle size increased to 298 nm when the buffer pH was adjusted to 7.4. Furthermore, we found that too low or too high pH inhibited the formation of nanoparticles. In addition, within the range of 0.1 to 0.5 mg/mL, the concentration of SM did not have significant effect on nanoparticle size. However, when the concentration of SM reached 1 mg/ mL, nanoparticle had a final size over 600 nm with a PDI of 0.25 (**Figure 4.2C**). The loading of DOX had no significantly impact on final hydrodynamic size of the nanoparticle. With DOX loading content from 1% to 10% of chitosan, the size of nanoparticles only slightly shifted from 186 nm to 219 nm (**Figure 4.2D**).

Characterization of GCS-SM/DOX NP

With the above optimized condition, we synthesized nanoparticle with SM to chitosan ratio at 16% in pH 7.0 20 mM PBS buffer at the SM concentration of

0.5 mg/mL SM. The final hydrodynamic size of nanoparticle was 186 nm, with a slightly positive surface charge as shown in **Figure 4.3A**. Transmission electron microscopy revealed that these nanoparticles were spherical with the average size of 49.09±11.52 nm (**Figure 4.3B)**. We reasoned that the highly swelling and hydrated glycol chitosan caused the dramatically increased size of nanoparticles in aqueous solution.

Figure 4.3C showed the release behaviors of suramin and DOX from the nanoparticles. It was revealed that DOX and suramin shared a similar release pattern, in which after 8 h of incubation in PBS 7.4, both the DOX and suramin had reached the platform at around 80%. The simultaneously release pattern for DOX and suramin ascertained the optimized ratio between two drugs to maintain the same from the point of the preparation to the *in vivo* release process. Since the complex was slightly positive, there is a concern about the colloid stability of nanoparticles. The stability of nanoparticles was evaluated through the long-term incubation of NPs in PBS and short term incubation of NPs supplemented with FBS. **Figure 4.3D** showed that these NPs were stable and did not aggregate in 10% serum containing media. NPs were very stable in PBS environment as evidenced by no size increase after two weeks incubation at 37ºC (**Figure 4.3E**).

GCS-SM/DOX NP inhibits cell migration and invasion

To investigate the effect of suramin or suramin nanoparticles on breast cancer cell migration, wound healing assay and transwell invasion assay were carried out. In the wound healing assay, effects of different treatments on cell migration were analyzed by live cell imaging (**Figure 4.4).**

The average speed for cell migration was measured by the wound distance divided by the time consumed to completely heal. **Figure 4.4 A and B** showed that suramin significantly inhibited cell migration and the effect was enhanced by GCS-SM nanoparticle (Control group had an average speed of 28.17 μm/h, which was twice as fast as the group treated with suramin **(Figure 4.4C).** Interestingly, glycol chitosan also showed an obviously inhibiting effect on cell migration with an average speed of 18.17 μm/h. A study showed that 100 μg/mL glycated chitosan significantly inhibited the migration of 4T1 and MDA-MB-231 cells, and reasoned the cause of the inhibition was that glycated chitosan up-regulated E-cadherin and down-regulated slug and twist 1.[102] Based on the structural similarity, we postulate that GCS has a similar (if not the same) function as glycated chitosan. Next, we tested whether the effect of suramin and suramin nanoparticle on cell migration was due to its cytotoxic effect. We found that neither suramin nor GCS-SM NP inhibited cell proliferation at the concentration up to 200 μM after 24 h treatment (**Figure 4.4D)**, which indicates that the inhibition of cell migration is not towing to the cytotoxic effect.

To investigate the inhibition effect of SM and GCS-SM NPs on cell invasion, we performed a transwell invasion assay. **Figure 4.5** showed that the invaded cell number per view area was significantly decreased from 951.75 in the control group to 718 in the group treated with 40 μM SM. GCS-SM NPs further decreased the number to 483. Thus, we proved that SM or GCS-SM NPs inhibited both cell migration and invasion without causing noticeable cytotoxic effect.

Cellular uptake of GCS-SM/DOX NPs

To measure GCS-SM/DOX NPs uptake efficiency *in vitro*, we treated MDA-MB-231 cells with free drugs, free-drug combinations, and GCS-SM/DOX NPs. After 1, 3, and 6 h of incubation, cells were analyzed by the flow cytometry (FACS) and confocal microscopy**. Figure 4.6A** showed that free DOX entered cells much slower than GCS-SM/DOX NPs: after 1h of treatment, NPs treatment exhibited a much stronger red fluorescence signal inside cell than free DOX; after 3h, almost all of DOX that delivered by NPs was in nuclei while a lot of DOX from free DOX treatment still stayed in cytosol. We next compared the cellular uptake behaviors of free DOX or GCS-SM/DOX NPs at 3 h and 6 h in presence or absence of a/b FGF using FACS (**Figure 4.6B**). In presence of a/b FGF, GCS-SM/DOX NPs treatment showed a much better DOX uptake compared to free DOX. Without a/b FGF treatment, no significant difference in uptake was observed between free DOX and GCS-SM/DOX NPs treatments at 3 h and 6 h. It's an interesting phenomenon that a/b FGF causes the differences in DOX uptake between GCS-SM/DOX NPs and free DOX, we reason that FGF might induced chemo-resistance[103] while suramin could sensitizer those drug resistant cells.

Suramin and DOX have synergistic growth inhibitory effect of MDA-MB-231 cells

Suramin showed biphasic effects on the proliferation of cancer cells.[104] On one hand, as a non-specific growth factor inhibitor, it inhibits angiogenesis of the cancer cells. On the other hand, high concentration of suramin kills cancer cells

directly. Although it has been reported that suramin kills cancer cells in a dose- and time-dependent manner,[94d, 94g, 105] the cell killing mechanism is still not fully understood.

Since SM was reported to induce the drug cross resistance against doxorubicin and amsacrine at high concentration,[106] it is crucial to find out the ratio that keeps the combination of DOX and suramin achieving synergistic effect while not inducing side effects. After 24 h treatment of 200 μM SM in form of either free SM or SM NPs, no cytotoxicity was observed. However, after 48 h of treatment, the IC50 of SM and SM NPs was 200 μM and 62.97 μM, respectively (**Figure 4.7B**). In this study we decided to test SM at nontoxic dose (10 μM, 20 μM and 100 μM) when combined with doxorubicin. We first investigated whether free-drug combinations at a non-toxic dose of suramin increased DOX cytotoxicity in presence of a/b FGF or not. **Figure 4.7A** showed that the cytotoxicity of DOX was greatly enhanced by the addition of 10 μM SM, but further increase of SM concentration (20 μM or 100 μM) did not further enhance its cytotoxicity (**Figure 4.7A)**

SM was reported to enter human micro vascular endothelial cells through an active process involving caveolae system,[107] where the zwitterionic nanoparticle may enter cell membrane through membrane penetration.[108] We reasoned that the synergistic effect was caused by the delivery of SM. To optimize the synergistic effect, different ratios of GCS-SM NPs to DOX were tested in MDA-MB-231 cells. The results in **Figure 4.7C** showed that synergistic growth inhibitory effects were observed at relatively low ratio of suramin to DOX

(Additive effect with CI = 1, synergism with CI < 1, and antagonism with CI > 1).[49] We further created a profile of synergistic growth inhibition of MDA-MB-231 cells under different concentrations of SM at 3 GCS-SM/DOX ratios (**Figure 4.7D**).

GCS-SM/DOX NP inhibits proliferation and metastasis of cancer cells in a tumor-bearing mouse model

Based on the *in vitro* results, we further tested the anti-metastatic efficacy of GSC-SM/DOX NP in a breast cancer lung metastasis model in nude mice. There are two mostly used methods to generate breast cancer lung metastasis animal models, either by orthotropic implantation of cancer cells in the mammary gland or tail vein injection of cancer cells. We applied the tail vein injection not only because it was faster but also produced tumors mainly in lung tissue with the similar genetic profiles.[109] It was previously reported that if the treatment was started on the first day of the cell implantation, the number of metastasis would be greatly inhibited by the combination of chemotherapy and suramin.[94h] To allow cancer cells to adapt to the new environment, we started the treatment on the second day after cancer cell inoculation. The effect of combination treatment on the breast cancer lung metastasis was evaluated by bioluminescence for ventral images. **Figure 4.8B** showed that the high sensitivity of luminescence imaging system and that the signal was highly correlated with cell number in the range of 125 and 8000 cells/well.

The whole body photoemission rate was measured to indicate the cell proliferation and the progression of metastasis over the next 6 weeks (**Figure 4.8.A)**. The results showed that in the control group MDA-MB-231 cells was

accumulated at the stem of tail for 4 weeks and the signal for lung metastasis was dramatically increased after week 5. For the free SM or SM-NPs treatment, both the proliferation of cancer cells and metastasis were slowed down compared to the control. For the free drug combination treatment, the proliferation of cancer cells was dramatically inhibited and no detectable lung metastasis was observed during the experimental period, while SM/DOX NPs completely eradicated the cancer cells from it treated mice. Furthermore, the injection of free SM, free DOX/suramin, SM NPs and GCS-SM/DOX NPs did not cause significant weight loss (**Figure 4.8C**).

Kaplan-Meier survival analysis was carried out for 12 weeks (**Figure 4.9A**). The saline treated group showed a 100% lethal by 68 days. SM and SM NPs treatments had moderately increased survival rates. The median survival time for control mice was 64.5 days while for SM treatment alone reached 76.5 days. For the free combination group and GCS-SM/DOX nanoparticle group, the median survival time was significantly improved (P=0.0038 and 0.021 respectively). The median survival time was extended to 81.5 days for free drug combination treatment group, and for GCS-SM/DOX nanoparticle treatment group the time was extended to higher than 85 days. After weeks 12, the free drug combination group has the survival rate of 50% while GCS-SM/DOX NPs group achieved 60%. As the metastatic site formed a colony instead of the formation of discrete tumors using the method of tail vein injection,[110] we further evaluated the metastatic status of each group by measuring the lung weight (**Figure 4.9B**). Neither SM nor SM NPs group showed any significant effect on

lung weight compared to the control, while the free drug combination and the nanoparticle combination treatments reduced lung weight by 53% (P=0.0218) and 56% (P=0.0089), respectively.

At the end of experiment, an ex vivo organ images were obtained by injecting luciferin i.v. to mice before they were sacrificed (**Figure 4.10**). Images of the control group were taken separately due to the fact that no mice was survived at the end of the whole experiment, but the same imaging protocol was carried out throughout all groups. Compared to control group, other mice that were survived till the end of the experiment showed no significantly visible luminescence, indicating that the metastasis was highly inhibited in these mice (**Figure 4.10A and B)**. As injected MDA-MB-231 cells were constitutively expressing both GFP and luciferase proteins, we were able to directly visualize the metastatic cancer cells in the lung in GFP channel. It was found out that the GFP expression was positively correlated with the luminescent signal shown above, and GCS-SM/DOX NP treated mice showed the least GFP signal in the lung (**Figure 4.10C**).

Evaluation of GCS-SM/DOX NP treatment by pathology analysis

DOX is an effective anticancer drug with notorious cardiotoxic effects.[111] It is suggested that the cardiotoxic effects primarily come from iron accumulation in mitochondria and the production of ROS. The DOX-dependent cardiac damage often results in irregular-aligned mitochondria and reduced perivascular fibrosis and detectable by transmission electron microscopy (TEM) images.[111-112] Analysis of the cardiovascular pathology by TEM revealed that the free drug

combination treated group exhibited misaligned mitochondria (**Figure 4.9C**), indicating the result of cardiotoxicity. However, no abnormal mitochondria alignment was detected in the co-delivery of suramin and DOX by nanoformulation.

Histologic analysis of lung and liver from each treatment was shown in **Figure 4.11**. Based on the boundary between the normal and tumor tissue, we found that the lung in control group was almost fully covered by cancer cells, and that both free SM and SM NPs treated groups have a mild reduction in the occupied area ratio between tumor and normal tissue size. In the free drug combination and the GCS-SM/DOX NP groups, no visible tumor was found in their tissue sections. There was no significant difference in histology among the livers from all groups.

CONLCUSION

In summary, we have successfully designed an efficient tool for co-loading anti-metastasis drug suramin and chemotherapeutic drug DOX with high loading content. At non-toxic dose of suramin, GCS-SM NPs were able to reduce the migration speed as well as invaded cells by half. *In vivo* experiment showed GCS-SM/DOX nanoparticle can greatly inhibit breast cancer lung metastases and improve the survival time for mice without causing cardiotoxicity.

MATERIALS AND METHODS

Materials

Glycol chitosan, suramin sodium salt, doxorubicin hydrochloride and eosin Y were purchased from Sigma. Acidic fibroblast growth factor (aFGF) and basic fibroblast factor were purchased from Peprotech. Nuclei Isolation Kit: nuclei EZ

prep was obtained from Sigma. Bradford protein assay kit was purchased from Bio-Rad. Luciferin was obtained from Merck Millipore. Gill's Hematoxylin No.2 was purchased from VWR.

Preparation of GCS-SM NPs

GCS-SM NPs were prepared by the mild ionic gelation technique between the sulfate groups in suramin and amine group in glycol chitosan. Different suramin concentration or amount, gelation solution pH, and doxorubicin were investigated, respectively. Typically, glycol chitosan was dissolved in PBS pH 7.0 buffer with an ionic strength at 20 mM to achieve the concentration of 2.4 mg/mL. Suramin was dissolved in the same buffer at the concentration of 0.5 mg/mL. Doxorubicin hydrochloride was dissolved in ddH_2O at 1 mg/mL. One and a half milliliter of suramin solution prepared above was mixing with doxorubicin solution first, and then injected slowly to 2.5 mL glycol chitosan solution at 0.2 mL/min with a microinjection pump (Harvard apparatus) under stirring (400 rpm) at room temperature. The mixture was stirred for 30 mins to allow the formation of nanoparticles. Afterwards, the mixture was centrifuged at 3000 rpm for 5 mins and large aggregates were removed. Nanoparticles were lyophilized with 1% trehalose (w/w) and stored at 4ºC prior to use.

The size and surface charge (ξ-potential) of the complexes were measured using a Zetasizer Nano-ZS (Malvern, UK) at pH 7.4. The morphology of the GCS-SM NPs was observed by transmission electron microscopy (Hitachi H-800 TEM) using a formvar/carbon coated Copper Grids (Electron Microscopy Science). The original complexes solution was dropped on a grid, washed with

ddH_2O (3 ×) to remove the remaining salt, and dried with a tissue paper. Doxorubicin concentration and suramin concentration were determined by UV-Vis spectrometer (Beckman, DU650) at 480 nm and 312 nm respectively.

Release kinetics and colloid stability of GCS-SM NPs

Two milliliter of GCS-SM NPs were loaded in the dialysis bags (MWCO: 6-8 KDa, Spectrum laboratories) and were put into 25 mL of pH 7.4,100 mM PBS at 37 °C under continually stirring. At predesigned time, 1 mL sample was taken and supplemented with 1 mL corresponding fresh medium. Samples were determined by UV-Vis spectrometer. All experiments were carried out in triplicate independently.

Nanoparticles were suspended in PBS 7.4 supplemented with different amounts of fetal bovine serum (FBS), ranging from 10% to 50% of FBS, at the final concentration of suramin at 100 μM at 37 °C. Nanoparticles size was measured at pre-determined time points with DLS.

Quantification of cellular uptake of GCS-SM NPs

Cellular uptake of GCS-SM NPs was quantified by flow cytometry and confocal microscopy. MDA-MB-231 cells were seeded in 12 well plates at 200,000 cells per well and treated with doxorubicin or GCS-SM/DOX NPs at the DOX concentration of 1 μM for 3 h. Afterwards, cells were washed 3 times with cold PBS to remove un-bounded doxorubicin or nanoparticles. Cells were collected and fixed in 4% formaldehyde, and examined by FACS.

To further investigate the uptake behaviors of nanoparticles, confocal microscopy was applied and used to monitor the uptake. MDA-MB-231 cells

were seeded in the petri dishes and different treatment groups were then added into each petri dish at the Dox concentration of 1 μg/mL. After 3 h co-incubation, cells were washed for 3 times and images were taken with Zeiss 710 LM.

Wound healing assay

The migration of breast cancer cell was evaluated with a wound healing assay. Living videos of cell migration in a 24 well plate were obtained with Zeiss confocal microscopy. Cells were pretreatment with a/b FGF and the wound was created by scraping the cell monolayer in a straight line with a p200 tip, and cell debris were removed by three time washing with PBS. Cells were incubated with different treatments and were allowed to grow in 37ºC chamber with 5% CO_2 condition for 24 h.

Transwell invasion assay

Cells were seeded with BD cell culture insert with the pore size of 8 μm (BD, Biosciences). The inserts were pre-coated with Matrigel at 0.2 mg/mL for 50 μL (dilution from BD Matrigel stock 10 mg/mL with coating buffer). Cells were seeded at 200,000 per 50 μL in the inserts in FBS free DMEM media. Suramin or GCS-SM NPs was then added to the inserts in 50 μL serum free medium. Lower chamber was added with 2 mL 10% FBS DMEM containing different treatments. After 16 h, the inserts were washed with PBS, fixed in 4% formaldehyde, and permeablized with methanol. Subsequently, cells were stained with hematoxylin and washed twice with PBS. The membrane in the inserts were then cut and mounted on the coverslip, and the cell number was counted with a light microscopy under 10 × magnification. Each well was imaged on 5 different fields,

and the invasion rate was expressed by the average number of cells per microscopic field.

Cell viability assay

The anticancer activities of the combination of DOX and suramin was first investigated with MTT assay. Two cell lines, MDA-MB-231 and MDA-MB-231 pre-incubated with a/b FGF, were treated with DOX, suramin and the combination of DOX with Suramin at 10 to 50 μM. Cells were seeded in 96-well plates at an initial density of 20,000 cells/well in 150 mL of DMEM medium supplemented with 100 U penicillin/streptomycin and 10% FBS. After 24 h of incubation, the medium was replaced with 150 μL of fresh medium containing different treatments and incubated for another 48 h. Afterwards, the media were replaced with 100 μL fresh media containing 1 mg/mL MTT reagent and incubated for another 4 h. The formed MTT crystal was dissolved with a stop solution and the finally optical density of the medium was measured using a microplate reader (ELX808, Bio-Tech Instrument, Inc) at λ = 595 nm.

In vivo experiment

All animal experiments were conducted in accordance with NIH regulations and approved by the Institutional Animal Care and Use Committee of the University of South Carolina. Female athymic mice at 6 to 8 weeks (nu/nu) were obtained from Jackson laboratory. MDA-MB-231-Luc-GFP cells were implanted by tail vein injecting 100 μL cell suspension (2×10^6). Mice were then randomly divided into 5 groups: 1) mice were treated with saline only; 2) Mice were treated with suramin at dose of 3.5 mg/kg once per week; 3) Mice were

treated with suramin and Doxorubicin at dose of 3.5 mg/kg of suramin and 0.5 mg/kg of Doxorubicin once per week; 4) mice were treated with GCS-SM NPs at the dose of 3.5 mg/kg once per week; 5) mice were treated with GCS-SM/DOX NPs at the equivalent dose once per week. The whole treatment procedure lasted for two months and the progression of tumor cells were monitored the luminescence with IVIS Lumia system by i.v. injection of luciferin (30 mg/mL, 50 μL) every week. Bodyweight of mice were measured every week. At the endpoint of each mouse, all the organs were isolated and lung weight was measured. Fluorescent images of lungs were also taken. Isolated organs were fixed in 10% neutralized formalin solution and embedded in paraffin. Tumor was sliced into 5 μm thickness and followed with standard H&E staining protocol.

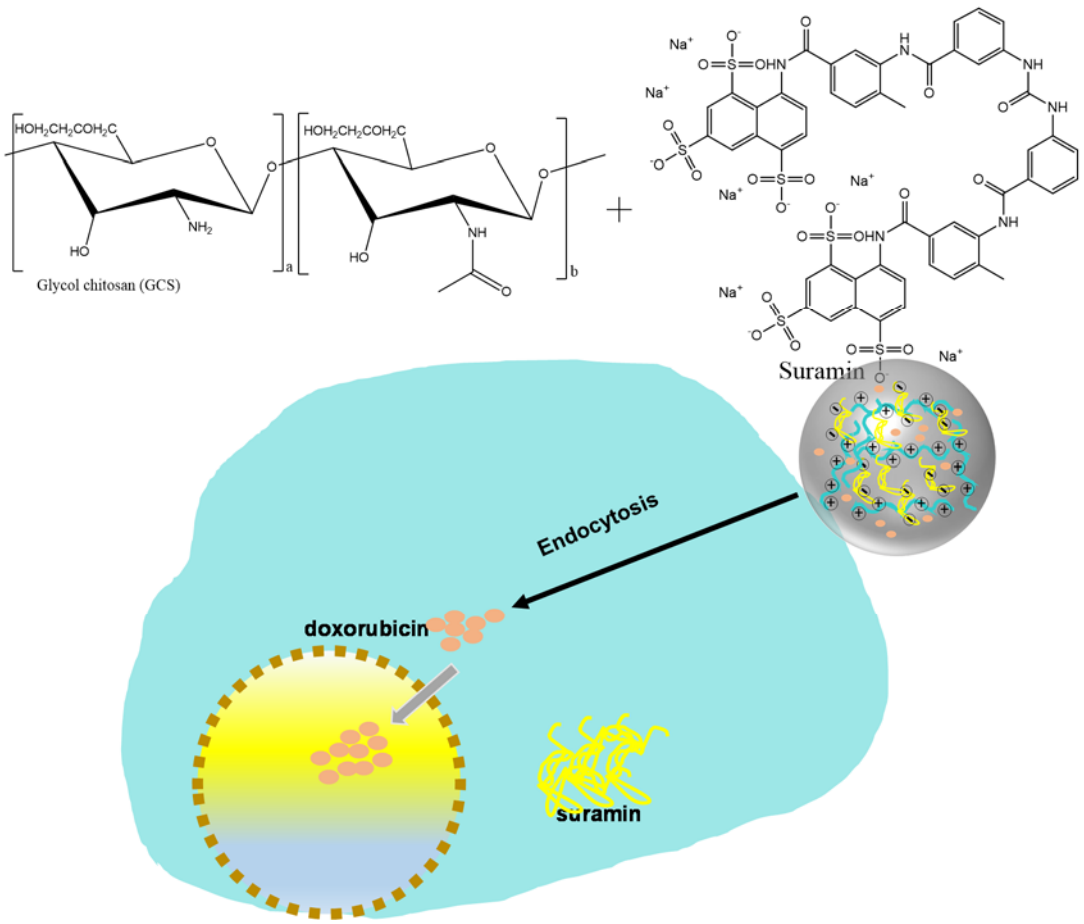

Figure 4.1 Illustration of the fabrication of GC-SM/DOX NPs.

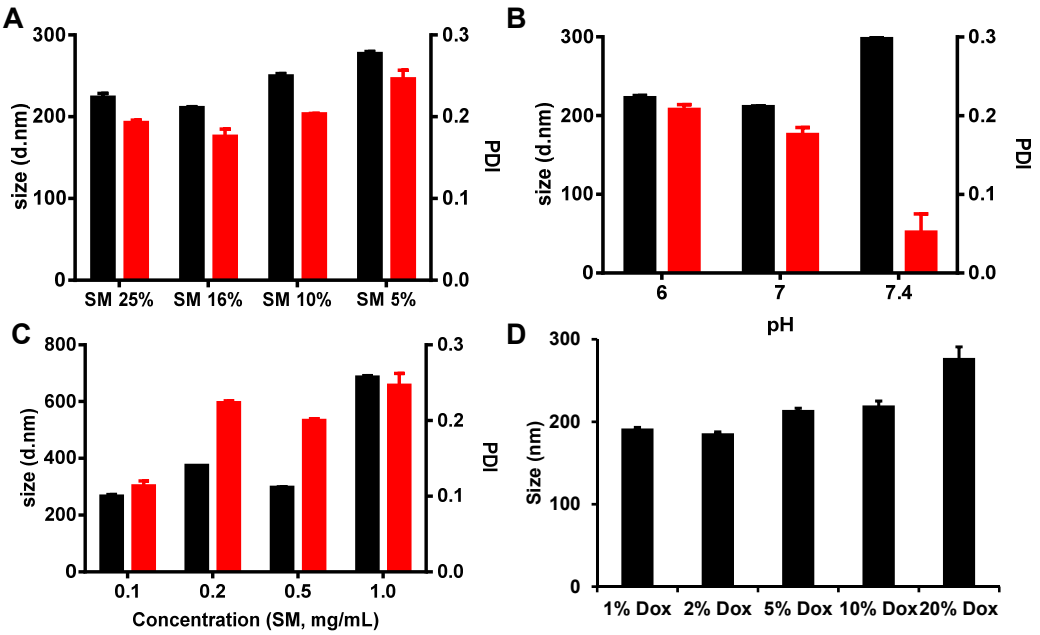

Figure 4.2 (A) The effects of SM amount, (B) pH of the buffer, (C) SM concentration, (D) and the loading content of DOX on the hydrodynamic size and PDI (Black column-hydrodynamic size, red column-PDI).

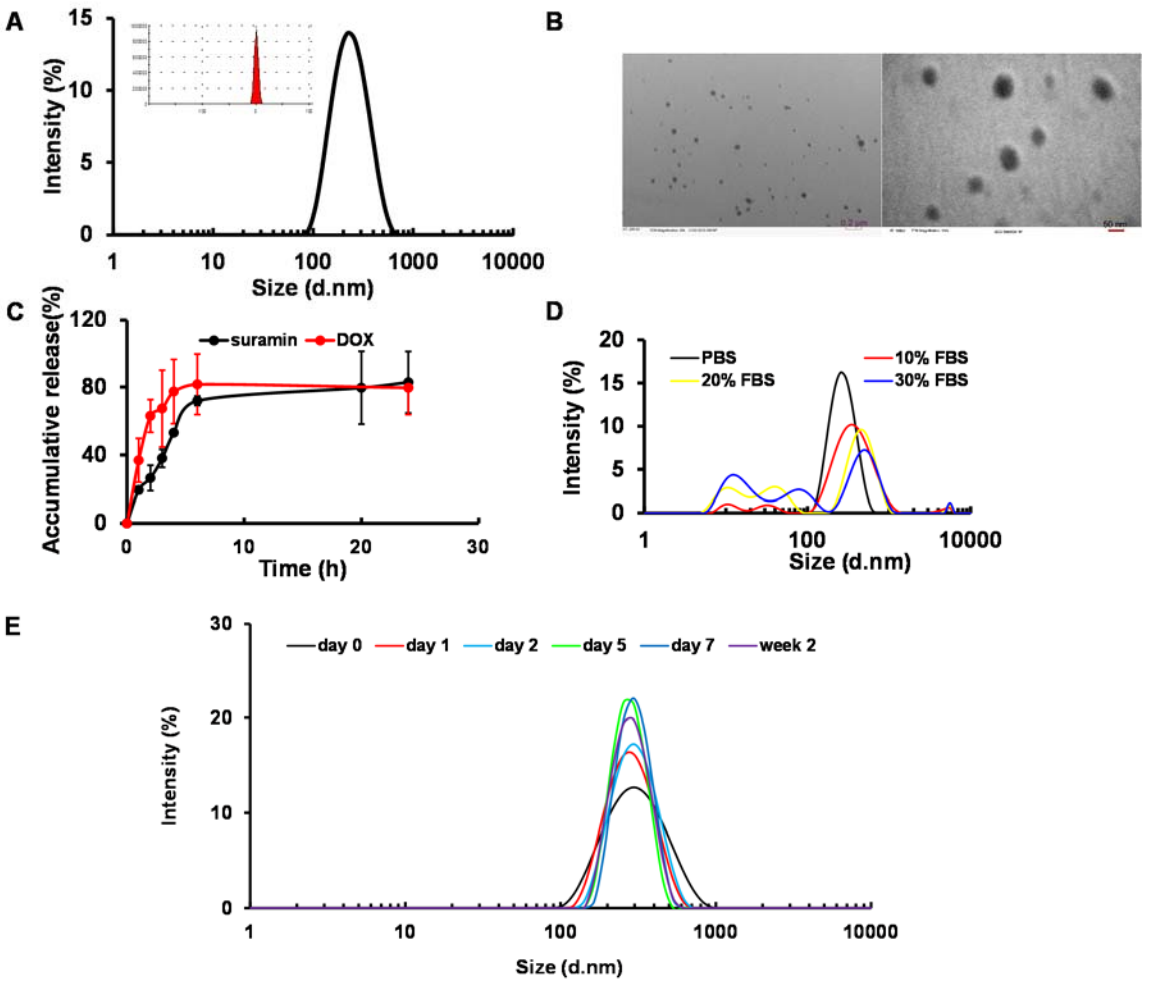

Figure 4.3 Characterization of GCS-SM NP. (A) Hydrodynamic size measure by DLS and surface charge measured by Zeta sizer. (B) Transmission electron microscopy images of GCS-SM/DOX NPs with 20 K and 100 K magnification, respectively. (Left) 20 K magnification, (Right) 100 K magnification. Scale bar: 200 nm and 50 nm. (C) *In vitro* release of suramin and doxorubicin in PBS. (D) Hydrodynamic size of GCS-SM NPs when co-incubated with 10%-30% FBS medium. (E) Long-term stability GCS-SM NPs in PBS.

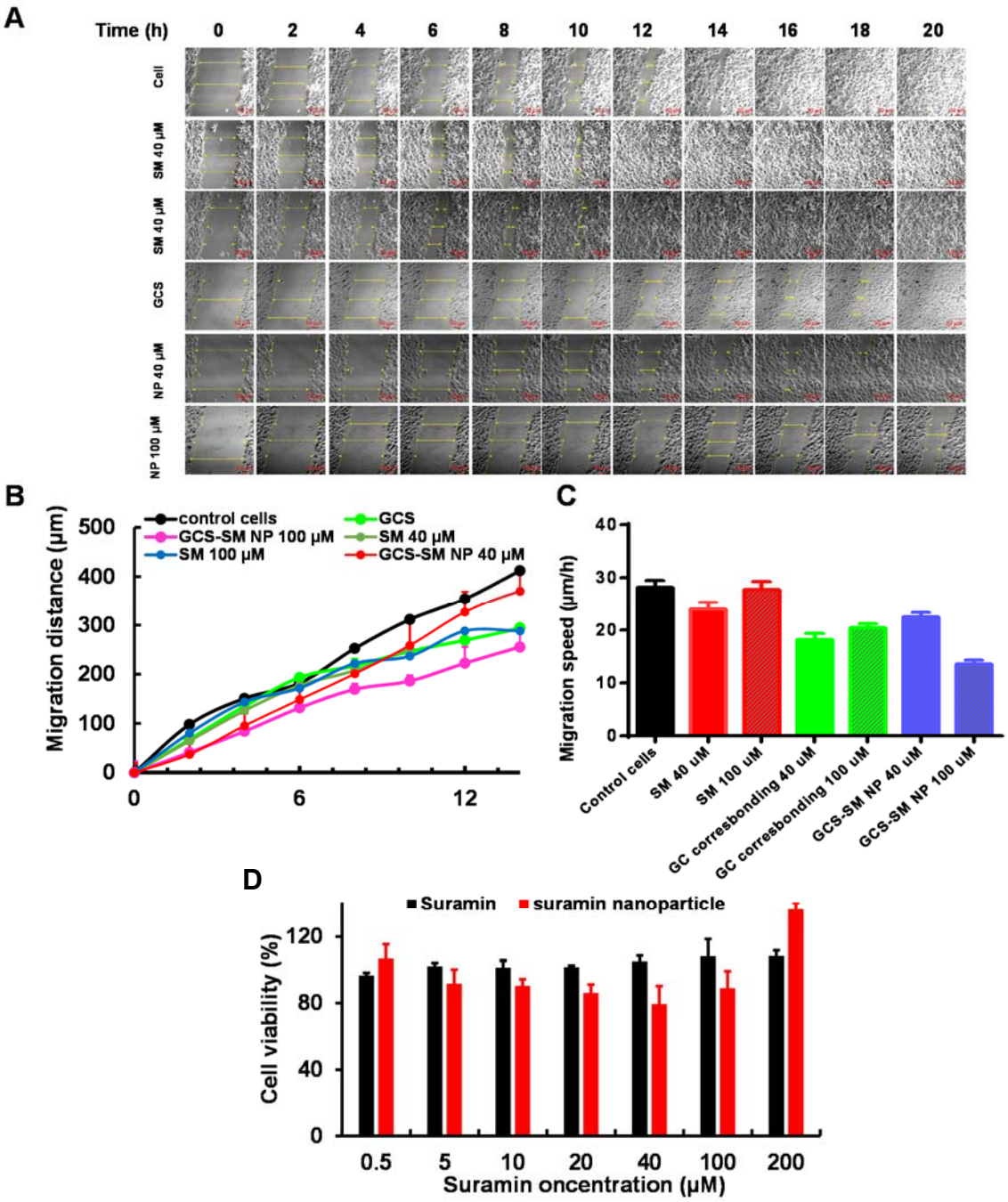

Figure 4.4 The effect of GCS-SM NP on the migration of MDA-MB-231 cells. (A) Photographs of cell migration after treated with SM, GCS or GCS-SM NP at different concentrations through a living cell imaging. Scale bar: 50 μm. (B) Quantification of migration distance of each time point. (C) Average migration speed of each treatment groups. (D) Cytotoxicity of SM or SM NPs toward MDA-MB-231 cells for 24 h.

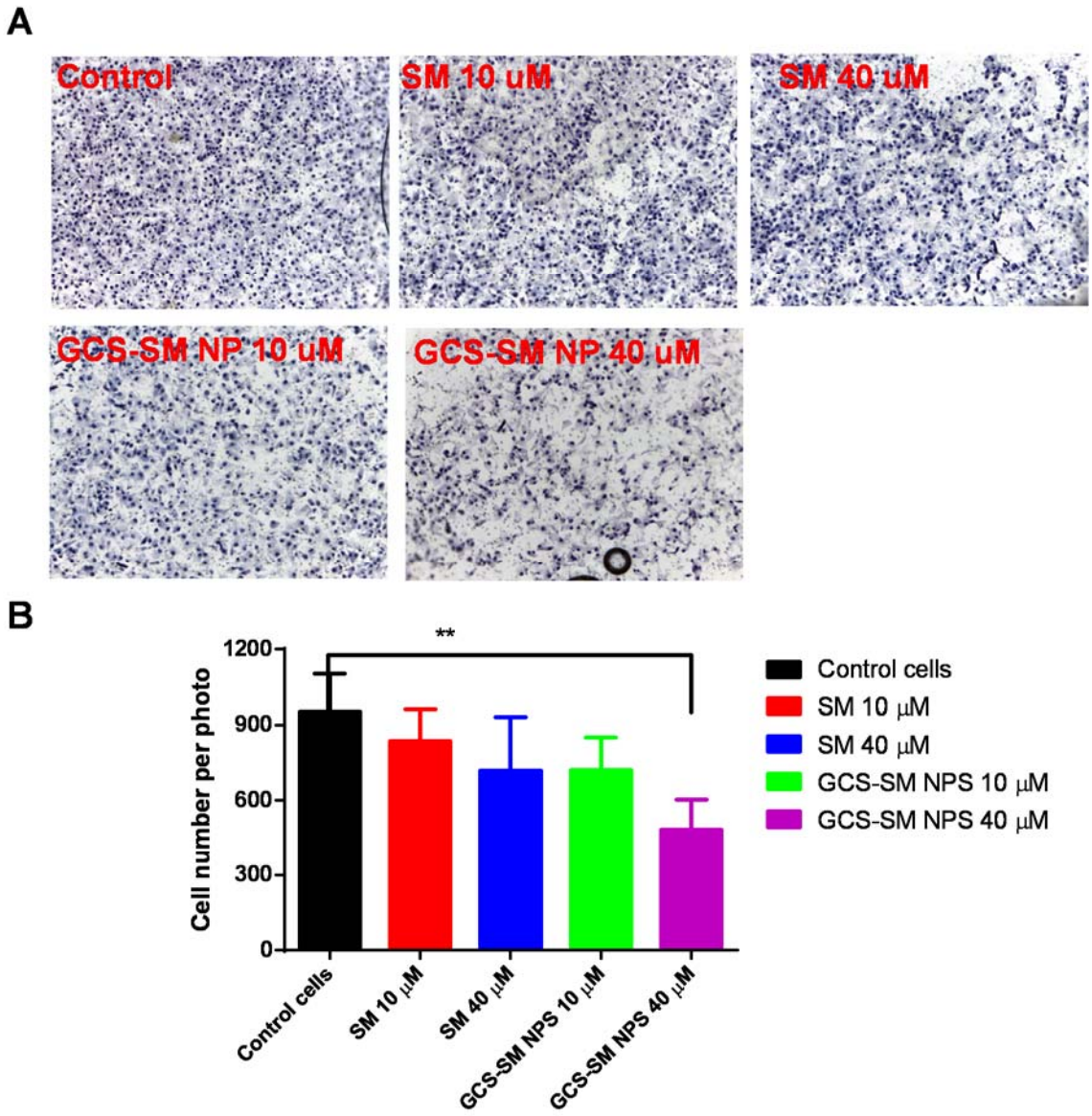

Figure 4.5 Cell invasion inhibitory effect. (A) Representative images of cells treated with SM or GCS-SM NPs at different concentrations. (B) Cell counting result after 16 h invasion study. (N=5 pictures per treatment, ** P<0.01).

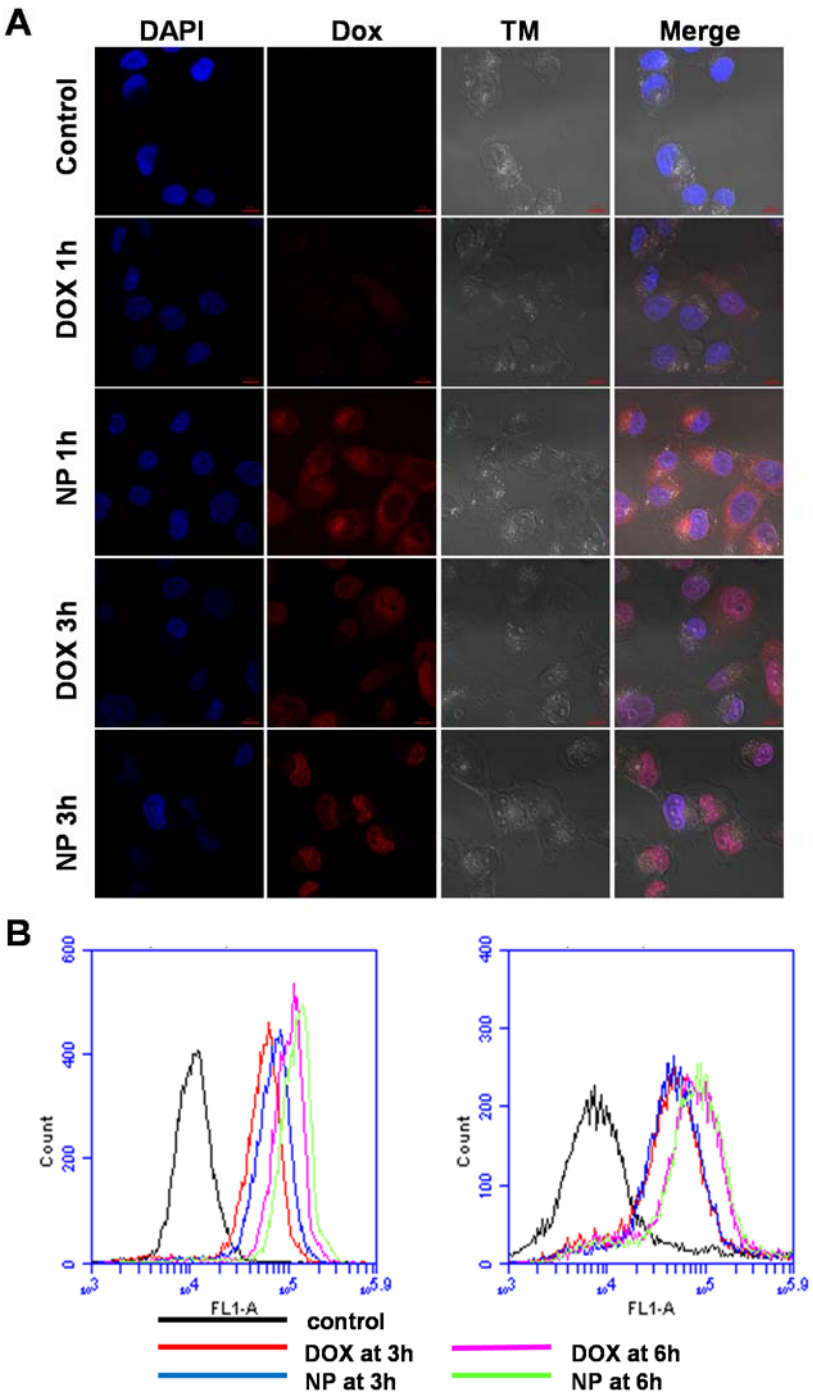

Figure 4.6 The uptake of nanoparticles in MDA-MB-231 cells. (A) Confocal microscopy images of MDA-MB-231 cells after treating with DOX or GCS-SM/DOX NP for 3 h. Blue-Hoechst 33342, red-DOX. (B) FACS of MDA-MB-231 cells treated with free DOX or GCS-SM/DOX NP for 3 h or 6 h. (Left: cells treated with a/b FGF, Right: cells without treatment of a/b FGF)

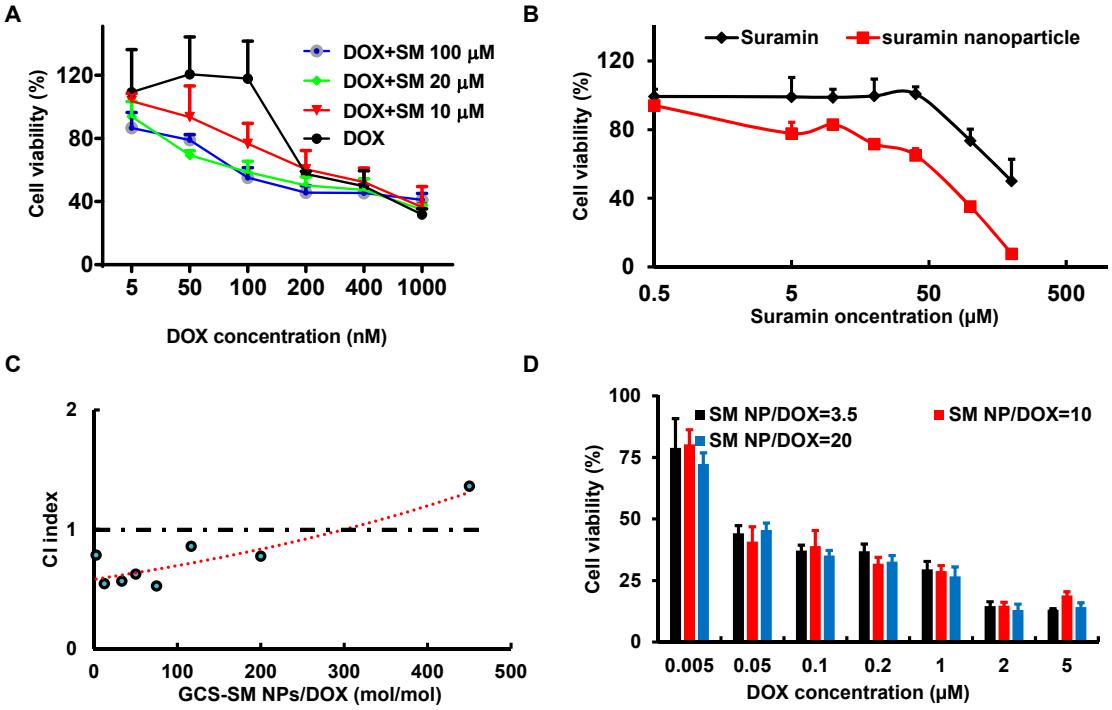

Figure 4.7 Synergistic effect of DOX and GCS-SM NPs in MDA-MB-231 cells. (A) Cell viability of DOX in combination with suramin at different concentration. (B) The cytotoxicity of Suramin and SM NP after 48 h treatment. (C) CI index calculation of DOX and GCS-SM NPs mixing at different ratio. (D) Cell viability of combinational nanoparticles at different ratio.

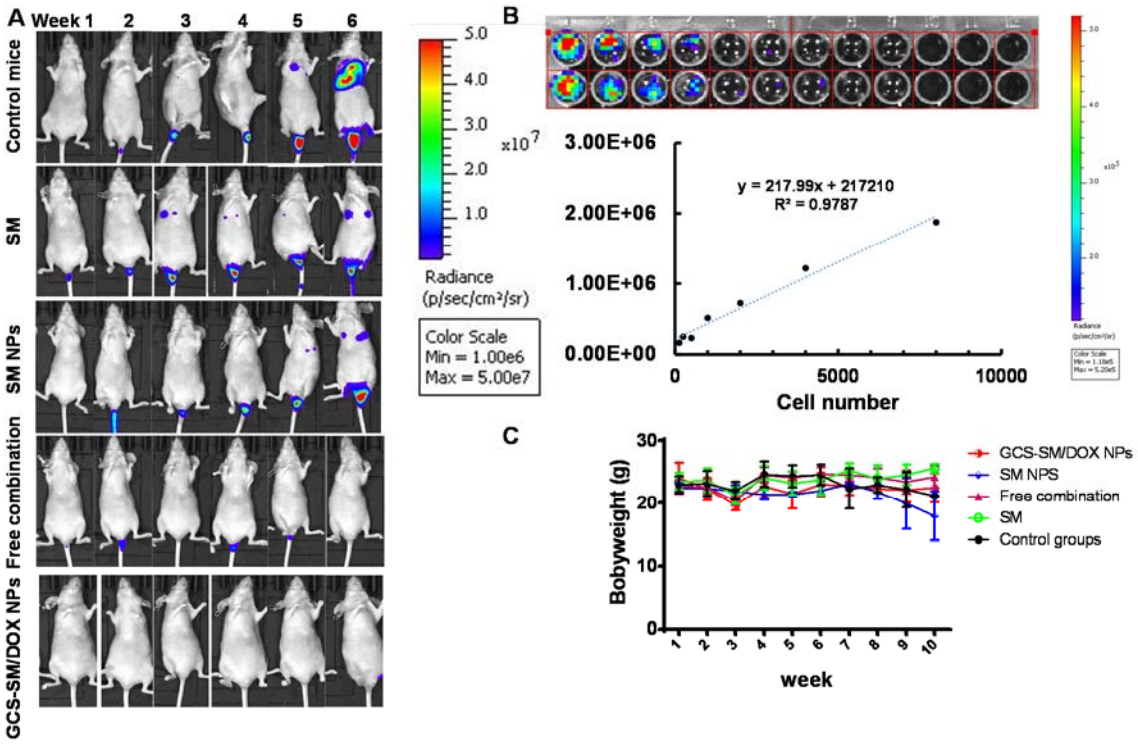

Figure 4.8 The inhibitory effect of GCS-SM/DOX NP on tumor growth *in vivo* using bioluminescence assay. (A) Luminescence images of mice in different treatments from week 1 to week 6. (B) Cell luminescence as a function of cell number. (C) Mice body weight change curves over the experiment.

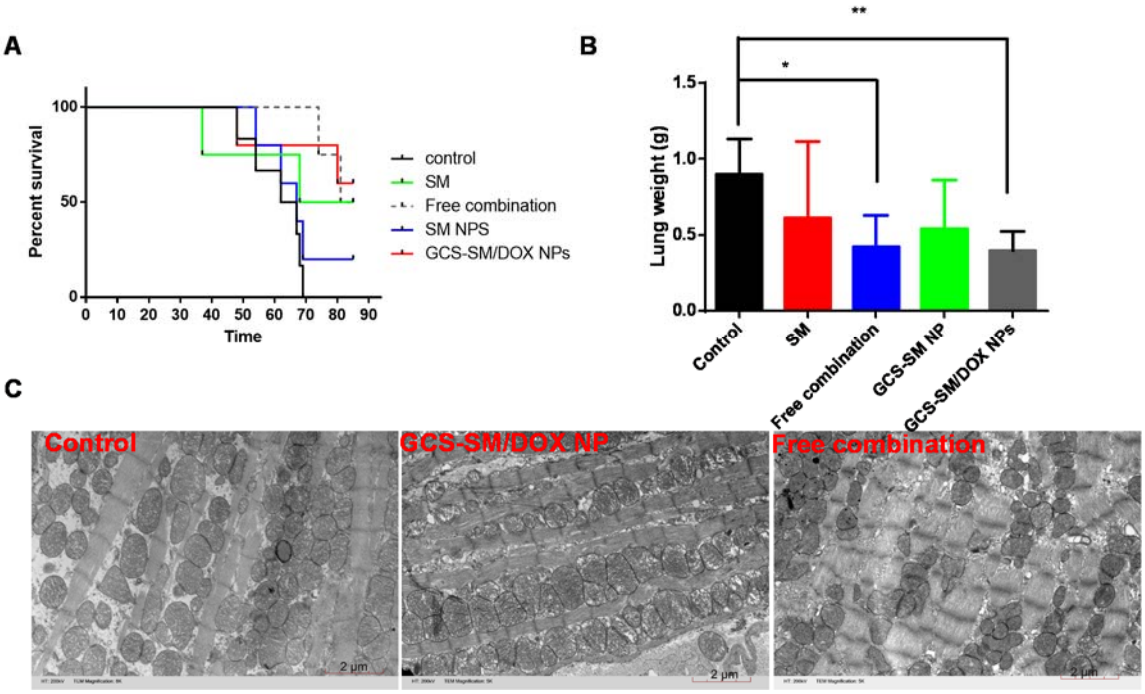

Figure 4.9 GCS-SM/DOX NP increased survival rate and reduced side effects. (A) Survive curves of different treatments, (B) lung weight in different treatments, (C) and the transmittance electron microscopy images of heart tissues from control, GCS-SM/DOX NP, and the free drug combination treatment groups. (* P<0.05, ** P<0.01)

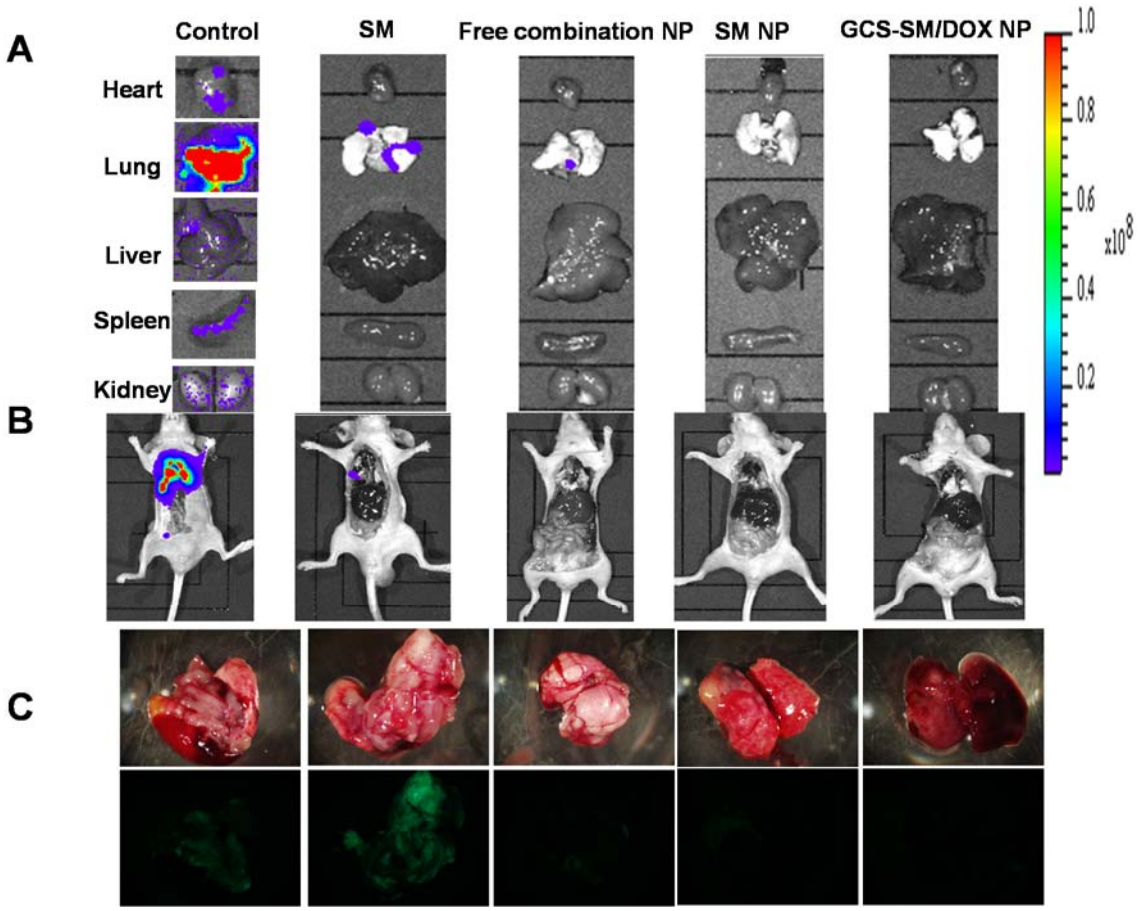

Figure 4.10 Evaluation of GCS-SM/DOX NP effect using ex vivo imaging. (A) Ex vivo images of different organs, (B) open chest mice, (C) and the fluorescent images of lungs in different treatment groups.

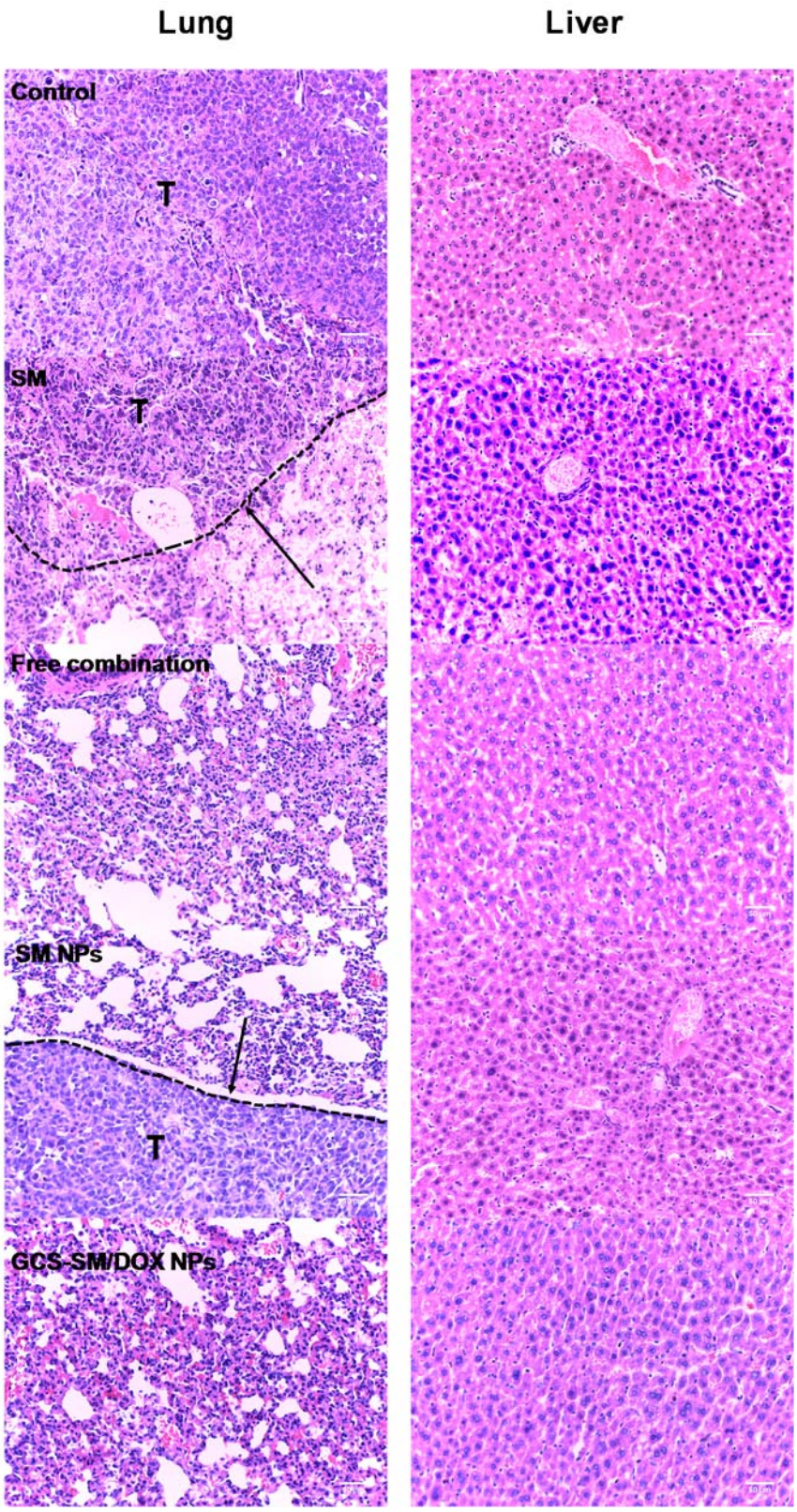

Figure 4.11 Histology analysis of lung and liver of mice. (H&E staining and arrows point at the tumor area)

CHAPTER 5

Outlook for the future development of multifunctional nanocarriers for cancer therapy

There has been a boost in developing nanocarrier-based therapies for treating cancer or other diseases during the past decades. In addition of selectively accumulating in tumors through EPR effect, nanocarriers enhance the bioavailability of poor soluble compounds. In order to fully exploit the technology and improve safety in clinical application, we developed two types of nano-carriers: 1) glycol chitosan based nanomedicine; 2) gold nanoparticles gated mesoporous silica nanoparticles.

We first developed an environment-sensitive peptide delivery system, dual secured nano-sting (DSNS), through the combination of a zwitterionic glycol chitosan and disulfide bonds. It released drug only if it went through the environment that had both acidic and reducing conditions. To further take advantage of this electrostatic system, we built the co-delivery system by which the suramin and DOX were delivered at the optimized ratio and with high loading efficiency in this nano-formulation. Suramin can act as a dual functional agent, for which it can act as a crosslinking agent as well as an angiogenesis inhibitor. The new nanoparticle was able to improve the median survival time of mice with breast cancer lung metastasis and reduced cardiocytotoxicity. To further

elaborate this combination effect *in vivo*, it will be beneficial to build an animal model where the metastasis process is induced in a different way. Instead of the tail vein injection of MDA-MB-231-GFP-Luc cells into nude mice, 4T1-Luc cells can be injected through the orthotopic implantation of in Balb/c mice. The orthotopic implantation exhibits a higher similarity with human metastasis process by controlling the direction of tumor progression from primary tumor to lung metastasis, and also makes it possible to investigate the effect of GCS-SM/DOX NP in inhibiting primary tumor.

In addition, we fabricated gold nanosphere/mesoporous silica hybrid (GoMe) nanocarriers which are suitable for encapsulating both hydrophilic and hydrophobic drugs. GoMe can release the encapsulated cargoes in response to either NIR irradiation or intracellularly elevated redox potential. DOX@GoMe coupled with NIR showed a synergistic effect compared to its components of applying either PTT alone or DOX treated cell alone. Furthermore, ^{64}Cu-labeled GoMe can successfully detect the spontaneous lung tumors in a urethane-induced lung cancer mouse model through PET imaging. However, GoMe also showed a high accumulation in liver. In order to increase the targeting efficiency and completely eradicate cancer cells, we developed the sigma 2 receptors targeted GoMe for cancer photothermal therapy and photodynamic therapy. By combining PTT and PDT, MBA Pc 4 GoMe efficiently killed UMSCC 22A and A 2058 cells. *In vivo* experiment established by subcutaneously injecting UMSCC 22A cells in nude mice proved that this targeting GoMe combining PTT and PDT was able to significantly inhibit tumor progression. For the future study, it would

be beneficial to evaluate the biodistribution of MBA Pc 4 GoMe. We expect a higher tumor selectivity of MBA Pc 4 GoMe and lower accumulation in liver after i.v injection. In addition, a systemic investigation of the structure–activity relationship of MBA and sigma 2 receptor would be valuable.

Overall, various multifunctional nanocarriers are being developed in my PhD research. By infusing the first nano-delivering system with high targeting efficacy, the function of diagnosis, higher drug-loading capacity and versatile drug-loading flexibility, our newer generation of nanocarriers promises to be more efficient and practical in the era of personalized medicine.

REFERENCES

1. DeSantis, C. E.; Lin, C. C.; Mariotto, A. B.; Siegel, R. L.; Stein, K. D.; Kramer, J. L.; Alteri, R.; Robbins, A. S.; Jemal, A., Cancer treatment and survivorship statistics, 2014. *CA: a cancer journal for clinicians* **2014,** *64* (4), 252-71.
2. (a) Twelves, C.; Jove, M.; Gombos, A.; Awada, A., Cytotoxic chemotherapy: Still the mainstay of clinical practice for all subtypes metastatic breast cancer. *Critical reviews in oncology/hematology* **2016**; (b) Spadi, R.; Brusa, F.; Ponzetti, A.; Chiappino, I.; Birocco, N.; Ciuffreda, L.; Satolli, M. A., Current therapeutic strategies for advanced pancreatic cancer: A review for clinicians. *World journal of clinical oncology* **2016,** *7* (1), 27-43.
3. Olson, L. E.; Bedja, D.; Alvey, S. J.; Cardounel, A. J.; Gabrielson, K. L.; Reeves, R. H., Protection from doxorubicin-induced cardiac toxicity in mice with a null allele of carbonyl reductase 1. *Cancer Res* **2003,** *63* (20), 6602-6.
4. Lotfi-Jam, K.; Carey, M.; Jefford, M.; Schofield, P.; Charleson, C.; Aranda, S., Nonpharmacologic strategies for managing common chemotherapy adverse effects: a systematic review. *J Clin Oncol* **2008,** *26* (34), 5618-29.
5. Debowska, K.; Debski, D.; Hardy, M.; Jakubowska, M.; Kalyanaraman, B.; Marcinek, A.; Michalski, R.; Michalowski, B.; Ouari, O.; Sikora, A.; Smulik, R.; Zielonka, J., Toward selective detection of reactive oxygen and nitrogen species with the use of fluorogenic probes--Limitations, progress, and perspectives. *Pharmacological reports : PR* **2015,** *67* (4), 756-64.
6. (a) Sun, T.; Zhang, Y. S.; Pang, B.; Hyun, D. C.; Yang, M.; Xia, Y., Engineered nanoparticles for drug delivery in cancer therapy. *Angew Chem Int Ed Engl* **2014,** *53* (46), 12320-64; (b) Wong, A. D.; Ye, M.; Ulmschneider, M. B.; Searson, P. C., Quantitative Analysis of the Enhanced Permeation and Retention (EPR) Effect. *PloS one* **2015,** *10* (5), e0123461; (c) Keereweer, S.; Mol, I. M.; Kerrebijn, J. D.; Van Driel, P. B.; Xie, B.; Baatenburg de Jong, R. J.; Vahrmeijer, A. L.; Lowik, C. W., Targeting integrins and enhanced permeability and retention (EPR) effect for optical imaging of oral cancer. *Journal of surgical oncology* **2012,** *105* (7), 714-8.
7. Weissig, V.; Pettinger, T. K.; Murdock, N., Nanopharmaceuticals (part 1): products on the market. *International journal of nanomedicine* **2014,** *9*, 4357-73.
8. O'Shaughnessy, J.; Gradishar, W. J.; Bhar, P.; Iglesias, J., Nab-paclitaxel for first-line treatment of patients with metastatic breast cancer and poor prognostic factors: a retrospective analysis. *Breast cancer research and treatment* **2013,** *138* (3), 829-37.
9. Barenholz, Y., Doxil(R)--the first FDA-approved nano-drug: lessons learned. *J Control Release* **2012,** *160* (2), 117-34.

10. Mindell, J. A., Lysosomal acidification mechanisms. *Annual review of physiology* **2012,** *74*, 69-86.
11. Go, Y. M.; Jones, D. P., Redox compartmentalization in eukaryotic cells. *Biochimica et biophysica acta* **2008,** *1780* (11), 1273-912. Xie, J.; Lee, S.; Chen, X., Nanoparticle-based theranostic agents. *Adv Drug Deliv Rev* **2010,** *62* (11), 1064-79.
13. Hu, C. M.; Aryal, S.; Zhang, L., Nanoparticle-assisted combination therapies for effective cancer treatment. *Ther Deliv* **2010,** *1* (2), 323-34.
14. Ma, J.; Waxman, D. J., Combination of antiangiogenesis with chemotherapy for more effective cancer treatment. *Mol Cancer Ther* **2008,** *7* (12), 3670-84.
15. Zhao, D.; Jiang, L.; Hahn, E. W.; Mason, R. P., Continuous low-dose (metronomic) chemotherapy on rat prostate tumors evaluated using MRI in vivo and comparison with histology. *Neoplasia* **2005,** *7* (7), 678-87.
16. (a) Hoskin, D. W.; Ramamoorthy, A., Studies on anticancer activities of antimicrobial peptides. *Biochimica et biophysica acta* **2008,** *1778* (2), 357-75; (b) Papo, N.; Shai, Y., Host defense peptides as new weapons in cancer treatment. *Cell Mol Life Sci* **2005,** *62* (7-8), 784-90.
17. (a) Yang, L.; Harroun, T. A.; Weiss, T. M.; Ding, L.; Huang, H. W., Barrel-stave model or toroidal model? A case study on melittin pores. *Biophys J* **2001,** *81* (3), 1475-85; (b) Lee, M. T.; Hung, W. C.; Chen, F. Y.; Huang, H. W., Mechanism and kinetics of pore formation in membranes by water-soluble amphipathic peptides. *Proc Natl Acad Sci U S A* **2008,** *105* (13), 5087-92.
18. Tosteson, M. T.; Tosteson, D. C., The sting. Melittin forms channels in lipid bilayers. *Biophys J* **1981,** *36* (1), 109-16.
19. (a) DeGrado, W. F.; Musso, G. F.; Lieber, M.; Kaiser, E. T.; Kezdy, F. J., Kinetics and mechanism of hemolysis induced by melittin and by a synthetic melittin analogue. *Biophys J* **1982,** *37* (1), 329-38; (b) Brogden, K. A., Antimicrobial peptides: pore formers or metabolic inhibitors in bacteria? *Nature reviews. Microbiology* **2005,** *3* (3), 238-50; (c) Popplewell, J. F.; Swann, M. J.; Freeman, N. J.; McDonnell, C.; Ford, R. C., Quantifying the effects of melittin on liposomes. *Biochimica et biophysica acta* **2007,** *1768* (1), 13-20.
20. Jo, M.; Park, M. H.; Kollipara, P. S.; An, B. J.; Song, H. S.; Han, S. B.; Kim, J. H.; Song, M. J.; Hong, J. T., Anti-cancer effect of bee venom toxin and melittin in ovarian cancer cells through induction of death receptors and inhibition of JAK2/STAT3 pathway. *Toxicol Appl Pharmacol* **2012,** *258* (1), 72-81.
21. Park, M. H.; Choi, M. S.; Kwak, D. H.; Oh, K. W.; Yoon do, Y.; Han, S. B.; Song, H. S.; Song, M. J.; Hong, J. T., Anti-cancer effect of bee venom in prostate cancer cells through activation of caspase pathway via inactivation of NF-kappaB. *Prostate* **2011,** *71* (8), 801-12.
22. Pan, H.; Soman, N. R.; Schlesinger, P. H.; Lanza, G. M.; Wickline, S. A., Cytolytic peptide nanoparticles ('NanoBees') for cancer therapy. *Wiley interdisciplinary reviews. Nanomedicine and nanobiotechnology* **2011,** *3* (3), 318-27.

23. Xu, P.; Van Kirk, E. A.; Zhan, Y.; Murdoch, W. J.; Radosz, M.; Shen, Y., Targeted charge-reversal nanoparticles for nuclear drug delivery. *Angew Chem Int Ed Engl* **2007,** *46* (26), 4999-5002.
24. (a) Huang, C.; Jin, H.; Qian, Y.; Qi, S.; Luo, H.; Luo, Q.; Zhang, Z., Hybrid melittin cytolytic Peptide-driven ultrasmall lipid nanoparticles block melanoma growth in vivo. *ACS nano* **2013,** *7* (7), 5791-800; (b) Leuschner, C.; Hansel, W., Membrane disrupting lytic peptides for cancer treatments. *Current pharmaceutical design* **2004,** *10* (19), 2299-310; (c) Hansel, W.; Leuschner, C.; Enright, F., Conjugates of lytic peptides and LHRH or betaCG target and cause necrosis of prostate cancers and metastases. *Molecular and cellular endocrinology* **2007,** *269* (1-2), 26-33; (d) Kumar, C. S.; Leuschner, C.; Doomes, E. E.; Henry, L.; Juban, M.; Hormes, J., Efficacy of lytic peptide-bound magnetite nanoparticles in destroying breast cancer cells. *J Nanosci Nanotechnol* **2004,** *4* (3), 245-9.
25. Soman, N. R.; Baldwin, S. L.; Hu, G.; Marsh, J. N.; Lanza, G. M.; Heuser, J. E.; Arbeit, J. M.; Wickline, S. A.; Schlesinger, P. H., Molecularly targeted nanocarriers deliver the cytolytic peptide melittin specifically to tumor cells in mice, reducing tumor growth. *J Clin Invest* **2009,** *119* (9), 2830-42.
26. Knight, D. K.; Shapka, S. N.; Amsden, B. G., Structure, depolymerization, and cytocompatibility evaluation of glycol chitosan. *J Biomed Mater Res A* **2007,** *83* (3), 787-98.
27. Xu, P.; Bajaj, G.; Shugg, T.; Van Alstine, W. G.; Yeo, Y., Zwitterionic chitosan derivatives for pH-sensitive stealth coating. *Biomacromolecules* **2010,** *11* (9), 2352-8.
28. Xiao, K.; Li, Y.; Luo, J.; Lee, J. S.; Xiao, W.; Gonik, A. M.; Agarwal, R. G.; Lam, K. S., The effect of surface charge on in vivo biodistribution of PEG-oligocholic acid based micellar nanoparticles. *Biomaterials* **2011,** *32* (13), 3435-46.
29. (a) Ho, Y. P.; Chen, H. H.; Leong, K. W.; Wang, T. H., Evaluating the intracellular stability and unpacking of DNA nanocomplexes by quantum dots-FRET. *J Control Release* **2006,** *116* (1), 83-9; (b) Alabi, C. A.; Love, K. T.; Sahay, G.; Stutzman, T.; Young, W. T.; Langer, R.; Anderson, D. G., FRET-labeled siRNA probes for tracking assembly and disassembly of siRNA nanocomplexes. *ACS nano* **2012,** *6* (7), 6133-41.
30. (a) Tan, Y. X.; Chen, C.; Wang, Y. L.; Lin, S.; Wang, Y.; Li, S. B.; Jin, X. P.; Gao, H. W.; Du, F. S.; Gong, F.; Ji, S. P., Truncated peptides from melittin and its analog with high lytic activity at endosomal pH enhance branched polyethylenimine-mediated gene transfection. *J Gene Med* **2012,** *14* (4), 241-50; (b) Baumhover, N. J.; Anderson, K.; Fernandez, C. A.; Rice, K. G., Synthesis and in vitro testing of new potent polyacridine-melittin gene delivery peptides. *Bioconjug Chem* **2010,** *21* (1), 74-83.
31. (a) Scudiero, D. A.; Monks, A.; Sausville, E. A., Cell line designation change: multidrug-resistant cell line in the NCI anticancer screen. *Journal of the National Cancer Institute* **1998,** *90* (11), 862; (b) Garraway, L. A.; Widlund, H. R.; Rubin, M. A.; Getz, G.; Berger, A. J.; Ramaswamy, S.; Beroukhim, R.; Milner, D. A.; Granter, S. R.; Du, J.; Lee, C.; Wagner, S. N.; Li, C.; Golub, T. R.; Rimm, D.

L.; Meyerson, M. L.; Fisher, D. E.; Sellers, W. R., Integrative genomic analyses identify MITF as a lineage survival oncogene amplified in malignant melanoma. *Nature* **2005,** *436* (7047), 117-22; (c) Lee, M. T.; Sun, T. L.; Hung, W. C.; Huang, H. W., Process of inducing pores in membranes by melittin. *Proc Natl Acad Sci U S A* **2013,** *110* (35), 14243-8.
32. (a) Yoo, H. S.; Park, T. G., Folate-receptor-targeted delivery of doxorubicin nano-aggregates stabilized by doxorubicin-PEG-folate conjugate. *J Control Release* **2004,** *100* (2), 247-56; (b) He, H.; Cattran, A. W.; Nguyen, T.; Nieminen, A. L.; Xu, P., Triple-responsive expansile nanogel for tumor and mitochondria targeted photosensitizer delivery. *Biomaterials* **2014,** *35* (35), 9546-53; (c) Yu, Z.; Schmaltz, R. M.; Bozeman, T. C.; Paul, R.; Rishel, M. J.; Tsosie, K. S.; Hecht, S. M., Selective tumor cell targeting by the disaccharide moiety of bleomycin. *J Am Chem Soc* **2013,** *135* (8), 2883-6; (d) Bhattacharya, C.; Yu, Z.; Rishel, M. J.; Hecht, S. M., The carbamoylmannose moiety of bleomycin mediates selective tumor cell targeting. *Biochemistry* **2014,** *53* (20), 3264-6.
33. (a) Khan, M. S.; Vishakante, G. D.; Siddaramaiah, H., Gold nanoparticles: a paradigm shift in biomedical applications. *Advances in colloid and interface science* **2013,** *199-200*, 44-58; (b) Skrabalak, S. E.; Au, L.; Lu, X.; Li, X.; Xia, Y., Gold nanocages for cancer detection and treatment. *Nanomedicine (Lond)* **2007,** *2* (5), 657-68.
34. (a) Alkilany, A. M.; Thompson, L. B.; Boulos, S. P.; Sisco, P. N.; Murphy, C. J., Gold nanorods: their potential for photothermal therapeutics and drug delivery, tempered by the complexity of their biological interactions. *Adv Drug Deliv Rev* **2012,** *64* (2), 190-9; (b) Stern, J. M.; Stanfield, J.; Lotan, Y.; Park, S.; Hsieh, J. T.; Cadeddu, J. A., Efficacy of laser-activated gold nanoshells in ablating prostate cancer cells in vitro. *J Endourol* **2007,** *21* (8), 939-43.
35. Huang, X.; El-Sayed, M. A., Plasmonic photo-thermal therapy (PPTT). *Alexandria Journal of Medicine* **2011,** *47* (1), 1-9.
36. (a) Kwon, K. C.; Ryu, J. H.; Lee, J. H.; Lee, E. J.; Kwon, I. C.; Kim, K.; Lee, J., Proteinticle/gold core/shell nanoparticles for targeted cancer therapy without nanotoxicity. *Advanced materials* **2014,** *26* (37), 6436-41; (b) Zhang, Z.; Wang, J.; Chen, C., Near-infrared light-mediated nanoplatforms for cancer thermo-chemotherapy and optical imaging. *Advanced materials* **2013,** *25* (28), 3869-80; (c) Skrabalak, S. E.; Chen, J.; Au, L.; Lu, X.; Li, X.; Xia, Y., Gold Nanocages for Biomedical Applications. *Advanced materials* **2007,** *19* (20), 3177-3184; (d) Dong, W.; Li, Y.; Niu, D.; Ma, Z.; Gu, J.; Chen, Y.; Zhao, W.; Liu, X.; Liu, C.; Shi, J., Facile synthesis of monodisperse superparamagnetic Fe3O4 Core@hybrid@Au shell nanocomposite for bimodal imaging and photothermal therapy. *Advanced materials* **2011,** *23* (45), 5392-7; (e) Yavuz, M. S.; Cheng, Y.; Chen, J.; Cobley, C. M.; Zhang, Q.; Rycenga, M.; Xie, J.; Kim, C.; Song, K. H.; Schwartz, A. G.; Wang, L. V.; Xia, Y., Gold nanocages covered by smart polymers for controlled release with near-infrared light. *Nature materials* **2009,** *8* (12), 935-9; (f) Dickerson, E. B.; Dreaden, E. C.; Huang, X.; El-Sayed, I. H.; Chu, H.; Pushpanketh, S.; McDonald, J. F.; El-Sayed, M. A., Gold nanorod assisted near-infrared plasmonic photothermal therapy (PPTT) of squamous cell carcinoma in mice. *Cancer Lett* **2008,** *269* (1), 57-66; (g) Loo, C.; Lin, A.; Hirsch, L.; Lee, M. H.; Barton, J.; Halas,

N.; West, J.; Drezek, R., Nanoshell-enabled photonics-based imaging and therapy of cancer. *Technology in cancer research & treatment* **2004,** *3* (1), 33-40.
37. Song, D. K.; Lenggoro, I. W.; Hayashi, Y.; Okuyama, K.; Kim, S. S., Changes in the shape and mobility of colloidal gold nanorods with electrospray and differential mobility analyzer methods. *Langmuir* **2005,** *21* (23), 10375-82.
38. (a) Chen, J.; Saeki, F.; Wiley, B. J.; Cang, H.; Cobb, M. J.; Li, Z. Y.; Au, L.; Zhang, H.; Kimmey, M. B.; Li, X.; Xia, Y., Gold nanocages: bioconjugation and their potential use as optical imaging contrast agents. *Nano letters* **2005,** *5* (3), 473-7; (b) Wu, D.; Jiang, S.; Cheng, Y.; Liu, X., Three-layered metallodielectric nanoshells: plausible meta-atoms for metamaterials with isotropic negative refractive index at visible wavelengths. *Opt Express* **2013,** *21* (1), 1076-86; (c) Chen, J.; Wiley, B.; Li, Z. Y.; Campbell, D.; Saeki, F.; Cang, H.; Au, L.; Lee, J.; Li, X.; Xia, Y., Gold Nanocages: Engineering Their Structure for Biomedical Applications. *Advanced materials* **2005,** *17* (18), 2255-2261.
39. (a) Xiao, Y.; Hong, H.; Matson, V. Z.; Javadi, A.; Xu, W.; Yang, Y.; Zhang, Y.; Engle, J. W.; Nickles, R. J.; Cai, W.; Steeber, D. A.; Gong, S., Gold Nanorods Conjugated with Doxorubicin and cRGD for Combined Anticancer Drug Delivery and PET Imaging. *Theranostics* **2012,** *2* (8), 757-68; (b) Wu, C.; Yu, C.; Chu, M., A gold nanoshell with a silica inner shell synthesized using liposome templates for doxorubicin loading and near-infrared photothermal therapy. *International journal of nanomedicine* **2011,** *6*, 807-13.
40. (a) Zhu, Y.; Meng, W.; Gao, H.; Hanagata, N., Hollow Mesoporous Silica/Poly(l-lysine) Particles for Codelivery of Drug and Gene with Enzyme-Triggered Release Property. *The Journal of Physical Chemistry C* **2011,** *115* (28), 13630-13636; (b) Zhao, W.; Zhang, H.; He, Q.; Li, Y.; Gu, J.; Li, L.; Li, H.; Shi, J., A glucose-responsive controlled release of insulin system based on enzyme multilayers-coated mesoporous silica particles. *Chem Commun (Camb)* **2011,** *47* (33), 9459-61.
41. (a) Guo, W.; Wang, J.; Lee, S. J.; Dong, F.; Park, S. S.; Ha, C. S., A general pH-responsive supramolecular nanovalve based on mesoporous organosilica hollow nanospheres. *Chemistry* **2010,** *16* (29), 8641-6; (b) Angelos, S.; Khashab, N. M.; Yang, Y. W.; Trabolsi, A.; Khatib, H. A.; Stoddart, J. F.; Zink, J. I., pH clock-operated mechanized nanoparticles. *J Am Chem Soc* **2009,** *131* (36), 12912-4; (c) Meng, H.; Xue, M.; Xia, T.; Zhao, Y. L.; Tamanoi, F.; Stoddart, J. F.; Zink, J. I.; Nel, A. E., Autonomous in vitro anticancer drug release from mesoporous silica nanoparticles by pH-sensitive nanovalves. *J Am Chem Soc* **2010,** *132* (36), 12690-7.
42. (a) Aznar, E.; Marcos, M. D.; Martinez-Manez, R.; Sancenon, F.; Soto, J.; Amoros, P.; Guillem, C., pH- and photo-switched release of guest molecules from mesoporous silica supports. *J Am Chem Soc* **2009,** *131* (19), 6833-43; (b) Vivero-Escoto, J. L.; Slowing, II; Wu, C. W.; Lin, V. S., Photoinduced intracellular controlled release drug delivery in human cells by gold-capped mesoporous silica nanosphere. *J Am Chem Soc* **2009,** *131* (10), 3462-3.
43. Jana, N. R.; Gearheart, L.; Murphy, C. J., Seeding Growth for Size Control of 5−40 nm Diameter Gold Nanoparticles. *Langmuir* **2001,** *17* (22), 6782-6786.

44. Pattani, V. P.; Tunnell, J. W., Nanoparticle-mediated photothermal therapy: a comparative study of heating for different particle types. *Lasers in surgery and medicine* **2012,** *44* (8), 675-84.
45. Jana, N. R.; Gearheart, L.; Murphy, C. J., Wet Chemical Synthesis of High Aspect Ratio Cylindrical Gold Nanorods. *The Journal of Physical Chemistry B* **2001,** *105* (19), 4065-4067.
46. (a) Ganta, S.; Devalapally, H.; Shahiwala, A.; Amiji, M., A review of stimuli-responsive nanocarriers for drug and gene delivery. *J Control Release* **2008,** *126* (3), 187-204; (b) Meng, F.; Hennink, W. E.; Zhong, Z., Reduction-sensitive polymers and bioconjugates for biomedical applications. *Biomaterials* **2009,** *30* (12), 2180-98; (c) Bae, Y.; Fukushima, S.; Harada, A.; Kataoka, K., Design of environment-sensitive supramolecular assemblies for intracellular drug delivery: polymeric micelles that are responsive to intracellular pH change. *Angew Chem Int Ed Engl* **2003,** *42* (38), 4640-3.
47. Link, S.; Burda, C.; Nikoobakht, B.; El-Sayed, M. A., Laser-Induced Shape Changes of Colloidal Gold Nanorods Using Femtosecond and Nanosecond Laser Pulses. *The Journal of Physical Chemistry B* **2000,** *104* (26), 6152-6163.
48. Lu, J.; Liong, M.; Zink, J. I.; Tamanoi, F., Mesoporous Silica Nanoparticles as a Delivery System for Hydrophobic Anticancer Drugs. *Small* **2007,** *3* (8), 1341-1346.
49. Chou, T. C., Drug combination studies and their synergy quantification using the Chou-Talalay method. *Cancer Res* **2010,** *70* (2), 440-6.
50. Lee, D.; Hong, J. W.; Park, C.; Lee, H.; Lee, J. E.; Hyeon, T.; Paik, S. R., Ca2+-dependent intracellular drug delivery system developed with "raspberry-type" particles-on-a-particle comprising mesoporous silica core and alpha-synuclein-coated gold nanoparticles. *ACS nano* **2014,** *8* (9), 8887-95.
51. Sharma, P.; Brown, S. C.; Bengtsson, N.; Zhang, Q.; Walter, G. A.; Grobmyer, S. R.; Santra, S.; Jiang, H.; Scott, E. W.; Moudgil, B. M., Gold-Speckled Multimodal Nanoparticles for Noninvasive Bioimaging. *Chem Mater* **2008,** *20* (19), 6087-6094.
52. Lin, M.; Guo, C.; Li, J.; Zhou, D.; Liu, K.; Zhang, X.; Xu, T.; Zhang, H.; Wang, L.; Yang, B., Polypyrrole-coated chainlike gold nanoparticle architectures with the 808 nm photothermal transduction efficiency up to 70%. *ACS applied materials & interfaces* **2014,** *6* (8), 5860-8.
53. Zhang, Z.; Wang, L.; Wang, J.; Jiang, X.; Li, X.; Hu, Z.; Ji, Y.; Wu, X.; Chen, C., Mesoporous silica-coated gold nanorods as a light-mediated multifunctional theranostic platform for cancer treatment. *Advanced materials* **2012,** *24* (11), 1418-23.
54. (a) Georgy Terentyuk, E. P., Vitaly Khanadeev, Daniil Chumakov, Elina Genina, Alexey Bashkatov, Valery Tuchin, Alla Bucharskaya, Galina Maslyakova, Nikolai Khlebtsov, Boris Khlebtsov, Gold nanorods with a hematoporphyrin-loaded silica shell for dual-modality photodynamic and photothermal treatment of tumors in vivo. *Nano research* **2014,** *7* (3), 12; (b) Shen, S.; Tang, H.; Zhang, X.; Ren, J.; Pang, Z.; Wang, D.; Gao, H.; Qian, Y.; Jiang, X.; Yang, W., Targeting mesoporous silica-encapsulated gold nanorods for chemo-photothermal therapy with near-infrared radiation. *Biomaterials* **2013,** *34* (12), 3150-8.

55. (a) Bahadur, K. C. R.; Xu, P., Multicompartment intracellular self-expanding nanogel for targeted delivery of drug cocktail. *Advanced materials* **2012,** *24* (48), 6479-83; (b) Shen, Y.; Zhou, Z.; Sui, M.; Tang, J.; Xu, P.; Van Kirk, E. A.; Murdoch, W. J.; Fan, M.; Radosz, M., Charge-reversal polyamidoamine dendrimer for cascade nuclear drug delivery. *Nanomedicine (Lond)* **2010,** *5* (8), 1205-17.
56. Hilgenbrink, A. R.; Low, P. S., Folate receptor-mediated drug targeting: from therapeutics to diagnostics. *Journal of pharmaceutical sciences* **2005,** *94* (10), 2135-46.
57. Yang, Y.; Hu, Y.; Wang, Y.; Li, J.; Liu, F.; Huang, L., Nanoparticle delivery of pooled siRNA for effective treatment of non-small cell lung cancer. *Molecular pharmaceutics* **2012,** *9* (8), 2280-9.
58. Locke, L. W.; Mayo, M. W.; Yoo, A. D.; Williams, M. B.; Berr, S. S., PET imaging of tumor associated macrophages using mannose coated 64Cu liposomes. *Biomaterials* **2012,** *33* (31), 7785-93.
59. (a) Cui, L.; Lin, Q.; Jin, C. S.; Jiang, W.; Huang, H.; Ding, L.; Muhanna, N.; Irish, J. C.; Wang, F.; Chen, J.; Zheng, G., A PEGylation-Free Biomimetic Porphyrin Nanoplatform for Personalized Cancer Theranostics. *ACS nano* **2015,** *9* (4), 4484-95; (b) Allison, R. R.; Moghissi, K., Oncologic photodynamic therapy: clinical strategies that modulate mechanisms of action. *Photodiagnosis Photodyn Ther* **2013,** *10* (4), 331-41.
60. (a) Hornung, R.; Walt, H.; Crompton, N. E.; Keefe, K. A.; Jentsch, B.; Perewusnyk, G.; Haller, U.; Kochli, O. R., m-THPC-mediated photodynamic therapy (PDT) does not induce resistance to chemotherapy, radiotherapy or PDT on human breast cancer cells in vitro. *Photochem Photobiol* **1998,** *68* (4), 569-74; (b) Spring, B. Q.; Rizvi, I.; Xu, N.; Hasan, T., The role of photodynamic therapy in overcoming cancer drug resistance. *Photochemical & photobiological sciences : Official journal of the European Photochemistry Association and the European Society for Photobiology* **2015,** *14* (8), 1476-91.
61. (a) Agostinis, P.; Berg, K.; Cengel, K. A.; Foster, T. H.; Girotti, A. W.; Gollnick, S. O.; Hahn, S. M.; Hamblin, M. R.; Juzeniene, A.; Kessel, D.; Korbelik, M.; Moan, J.; Mroz, P.; Nowis, D.; Piette, J.; Wilson, B. C.; Golab, J., Photodynamic therapy of cancer: an update. *CA: a cancer journal for clinicians* **2011,** *61* (4), 250-81; (b) Korbelik, M., PDT-associated host response and its role in the therapy outcome. *Lasers in surgery and medicine* **2006,** *38* (5), 500-8.
62. (a) Gao, F.; Bai, Y.; Ma, S. R.; Liu, F.; Li, Z. S., Systematic review: photodynamic therapy for unresectable cholangiocarcinoma. *Journal of hepato-biliary-pancreatic sciences* **2010,** *17* (2), 125-31; (b) Fluehler, C.; Colli, C.; Gatti, A.; Trevisan, G., Photodynamic therapy for nonmelanoma skin cancer of the genital area: our experience. *Acta dermatovenerologica Croatica : ADC* **2015,** *23* (2), 148-9; (c) Marrelli, M.; Menichini, G.; Provenzano, E.; Conforti, F., Applications of natural compounds in the photodynamic therapy of skin cancer. *Curr Med Chem* **2014,** *21* (12), 1371-90; (d) Ericson, M. B.; Wennberg, A. M.; Larko, O., Review of photodynamic therapy in actinic keratosis and basal cell carcinoma. *Therapeutics and clinical risk management* **2008,** *4* (1), 1-9; (e) Ahn, P. H.; Quon, H.; O'Malley, B. W.; Weinstein, G.; Chalian, A.; Malloy, K.; Atkins, J.

H.; Sollecito, T.; Greenberg, M.; McNulty, S.; Lin, A.; Zhu, T. C.; Finlay, J. C.; Cengel, K.; Livolsi, V.; Feldman, M.; Mick, R.; Busch, T. M., Toxicities and early outcomes in a phase 1 trial of photodynamic therapy for premalignant and early stage head and neck tumors. *Oral oncology* **2016**; (f) Rigual, N.; Shafirstein, G.; Cooper, M. T.; Baumann, H.; Bellnier, D. A.; Sunar, U.; Tracy, E. C.; Rohrbach, D. J.; Wilding, G.; Tan, W.; Sullivan, M.; Merzianu, M.; Henderson, B. W., Photodynamic therapy with 3-(1'-hexyloxyethyl) pyropheophorbide a for cancer of the oral cavity. *Clin Cancer Res* **2013,** *19* (23), 6605-13; (g) Lou, P. J.; Jager, H. R.; Jones, L.; Theodossy, T.; Bown, S. G.; Hopper, C., Interstitial photodynamic therapy as salvage treatment for recurrent head and neck cancer. *British journal of cancer* **2004,** *91* (3), 441-6; (h) Furuse, K.; Fukuoka, M.; Kato, H.; Horai, T.; Kubota, K.; Kodama, N.; Kusunoki, Y.; Takifuji, N.; Okunaka, T.; Konaka, C.; et al., A prospective phase II study on photodynamic therapy with photofrin II for centrally located early-stage lung cancer. The Japan Lung Cancer Photodynamic Therapy Study Group. *J Clin Oncol* **1993,** *11* (10), 1852-7; (i) Friedberg, J. S.; Mick, R.; Stevenson, J. P.; Zhu, T.; Busch, T. M.; Shin, D.; Smith, D.; Culligan, M.; Dimofte, A.; Glatstein, E.; Hahn, S. M., Phase II trial of pleural photodynamic therapy and surgery for patients with non-small-cell lung cancer with pleural spread. *J Clin Oncol* **2004,** *22* (11), 2192-201; (j) Bader, M. J.; Stepp, H.; Beyer, W.; Pongratz, T.; Sroka, R.; Kriegmair, M.; Zaak, D.; Welschof, M.; Tilki, D.; Stief, C. G.; Waidelich, R., Photodynamic therapy of bladder cancer - a phase I study using hexaminolevulinate (HAL). *Urologic oncology* **2013,** *31* (7), 1178-83.

63. (a) Menon, C.; Kutney, S. N.; Lehr, S. C.; Hendren, S. K.; Busch, T. M.; Hahn, S. M.; Fraker, D. L., Vascularity and uptake of photosensitizer in small human tumor nodules: implications for intraperitoneal photodynamic therapy. *Clin Cancer Res* **2001,** *7* (12), 3904-11; (b) Eales, K. L.; Hollinshead, K. E.; Tennant, D. A., Hypoxia and metabolic adaptation of cancer cells. *Oncogenesis* **2016,** *5*, e190; (c) Semenza, G. L., Hypoxia-inducible factors: mediators of cancer progression and targets for cancer therapy. *Trends in pharmacological sciences* **2012,** *33* (4), 207-14; (d) Pogue, B. W.; O'Hara, J. A.; Demidenko, E.; Wilmot, C. M.; Goodwin, I. A.; Chen, B.; Swartz, H. M.; Hasan, T., Photodynamic therapy with verteporfin in the radiation-induced fibrosarcoma-1 tumor causes enhanced radiation sensitivity. *Cancer Res* **2003,** *63* (5), 1025-33.

64. (a) Middelburg, T. A.; de Bruijn, H. S.; van der Ploeg-van den Heuvel, A.; Neumann, H. A.; Robinson, D. J., The effect of light fractionation with a 2-h dark interval on the efficacy of topical hexyl-aminolevulinate photodynamic therapy in normal mouse skin. *Photodiagnosis Photodyn Ther* **2013,** *10* (4), 703-9; (b) Tetard, M. C.; Vermandel, M.; Leroy, H. A.; Leroux, B.; Maurage, C. A.; Lejeune, J. P.; Mordon, S.; Reyns, N., Interstitial 5-ALA photodynamic therapy and glioblastoma: preclinical model development and preliminary results. *Photodiagnosis Photodyn Ther* **2015**; (c) Maier, A.; Anegg, U.; Fell, B.; Rehak, P.; Ratzenhofer, B.; Tomaselli, F.; Sankin, O.; Pinter, H.; Smolle-Juttner, F. M.; Friehs, G. B., Hyperbaric oxygen and photodynamic therapy in the treatment of advanced carcinoma of the cardia and the esophagus. *Lasers in surgery and medicine* **2000,** *26* (3), 308-15; (d) Tomaselli, F.; Maier, A.; Pinter, H.; Stranzl, H.; Smolle-Juttner, F. M., Photodynamic therapy enhanced by hyperbaric oxygen in

acute endoluminal palliation of malignant bronchial stenosis (clinical pilot study in 40 patients). *Eur J Cardiothorac Surg* **2001,** *19* (5), 549-54.
65. Wang, C.; Tao, H.; Cheng, L.; Liu, Z., Near-infrared light induced in vivo photodynamic therapy of cancer based on upconversion nanoparticles. *Biomaterials* **2011,** *32* (26), 6145-54.
66. Wang, J.; Zhang, Z.; Zha, S.; Zhu, Y.; Wu, P.; Ehrenberg, B.; Chen, J. Y., Carbon nanodots featuring efficient FRET for two-photon photodynamic cancer therapy with a low fs laser power density. *Biomaterials* **2014,** *35* (34), 9372-81.
67. Huang, W. C.; Shen, M. Y.; Chen, H. H.; Lin, S. C.; Chiang, W. H.; Wu, P. H.; Chang, C. W.; Chiang, C. S.; Chiu, H. C., Monocytic delivery of therapeutic oxygen bubbles for dual-modality treatment of tumor hypoxia. *J Control Release* **2015,** *220* (Pt B), 738-50.
68. Zhang, J.; Liang, Y. C.; Lin, X.; Zhu, X.; Yan, L.; Li, S.; Yang, X.; Zhu, G.; Rogach, A. L.; Yu, P. K.; Shi, P.; Tu, L. C.; Chang, C. C.; Zhang, X.; Chen, X.; Zhang, W.; Lee, C. S., Self-Monitoring and Self-Delivery of Photosensitizer-Doped Nanoparticles for Highly Effective Combination Cancer Therapy in Vitro and in Vivo. *ACS nano* **2015,** *9* (10), 9741-56.
69. Cheng, B. H., Huacheng; Huang, Tao; Berr, Stuart S.; He, Jiang; Fan, Daping; Zhang, Jiajia; Xu, Peisheng, Gold Nanosphere Gated Mesoporous Silica Nanoparticle Responsive to Near-Infrared Light and Redox Potential as a Theranostic Platform for Cancer Therapy. *Journal of Biomedical Nanotechnology* **2016,** *12* (3), 15.
70. Haiss, W.; Thanh, N. T.; Aveyard, J.; Fernig, D. G., Determination of size and concentration of gold nanoparticles from UV-vis spectra. *Anal Chem* **2007,** *79* (11), 4215-21.
71. Moore, C. M.; Hoh, I. M.; Bown, S. G.; Emberton, M., Does photodynamic therapy have the necessary attributes to become a future treatment for organ-confined prostate cancer? *BJU International* **2005,** *96* (6), 754-758.
72. Baron, E. D.; Malbasa, C. L.; Santo-Domingo, D.; Fu, P.; Miller, J. D.; Hanneman, K. K.; Hsia, A. H.; Oleinick, N. L.; Colussi, V. C.; Cooper, K. D., Silicon phthalocyanine (Pc 4) photodynamic therapy is a safe modality for cutaneous neoplasms: results of a phase 1 clinical trial. *Lasers in surgery and medicine* **2010,** *42* (10), 728-35.
73. Zeng, J.; Sun, Q.; Su, J.; Han, J.; Zhang, Q.; Jin, Y., Protoporphyrin IX catalyzed hydrogen peroxide to generate singlet oxygen. *International journal of clinical and experimental medicine* **2015,** *8* (5), 6829-34.
74. Gomes, A.; Fernandes, E.; Lima, J. L., Fluorescence probes used for detection of reactive oxygen species. *Journal of biochemical and biophysical methods* **2005,** *65* (2-3), 45-80.
75. Banerjee, R.; Tyagi, P.; Li, S.; Huang, L., Anisamide-targeted stealth liposomes: a potent carrier for targeting doxorubicin to human prostate cancer cells. *Int J Cancer* **2004,** *112* (4), 693-700.
76. Huntosova, V.; Buzova, D.; Petrovajova, D.; Kasak, P.; Nadova, Z.; Jancura, D.; Sureau, F.; Miskovsky, P., Development of a new LDL-based transport system for hydrophobic/amphiphilic drug delivery to cancer cells. *International journal of pharmaceutics* **2012,** *436* (1-2), 463-71.

77. (a) Fernando, L. P.; Kandel, P. K.; Yu, J.; McNeill, J.; Ackroyd, P. C.; Christensen, K. A., Mechanism of cellular uptake of highly fluorescent conjugated polymer nanoparticles. *Biomacromolecules* **2010,** *11* (10), 2675-82; (b) Conner, S. D.; Schmid, S. L., Regulated portals of entry into the cell. *Nature* **2003,** *422* (6927), 37-44; (c) Rosenkranz, A. A.; Jans, D. A.; Sobolev, A. S., Targeted intracellular delivery of photosensitizers to enhance photodynamic efficiency. *Immunology and cell biology* **2000,** *78* (4), 452-64.
78. (a) Castano, A. P.; Demidova, T. N.; Hamblin, M. R., Mechanisms in photodynamic therapy: part one-photosensitizers, photochemistry and cellular localization. *Photodiagnosis Photodyn Ther* **2004,** *1* (4), 279-93; (b) Hung, H. I.; Schwartz, J. M.; Maldonado, E. N.; Lemasters, J. J.; Nieminen, A. L., Mitoferrin-2-dependent mitochondrial iron uptake sensitizes human head and neck squamous carcinoma cells to photodynamic therapy. *The Journal of biological chemistry* **2013,** *288* (1), 677-86.
79. (a) Ott, M.; Robertson, J. D.; Gogvadze, V.; Zhivotovsky, B.; Orrenius, S., Cytochrome c release from mitochondria proceeds by a two-step process. *Proc Natl Acad Sci U S A* **2002,** *99* (3), 1259-63; (b) Gottlieb, E.; Armour, S. M.; Harris, M. H.; Thompson, C. B., Mitochondrial membrane potential regulates matrix configuration and cytochrome c release during apoptosis. *Cell death and differentiation* **2003,** *10* (6), 709-17.
80. (a) Wang, J.; Zhang, L.; Chen, M.; Gao, S.; Zhu, L., Activatable Ferritin Nanocomplex for Real-Time Monitoring of Caspase-3 Activation during Photodynamic Therapy. *ACS applied materials & interfaces* **2015,** *7* (41), 23248-56; (b) Xue, L. Y.; Chiu, S. M.; Azizuddin, K.; Joseph, S.; Oleinick, N. L., The death of human cancer cells following photodynamic therapy: apoptosis competence is necessary for Bcl-2 protection but not for induction of autophagy. *Photochem Photobiol* **2007,** *83* (5), 1016-23.
81. (a) Li, Y.; Tang, J.; Pan, D. X.; Sun, L. D.; Chen, C.; Liu, Y.; Wang, Y. F.; Shi, S.; Yan, C. H., A Versatile Imaging and Therapeutic Platform Based on Dual-Band Luminescent Lanthanide Nanoparticles toward Tumor Metastasis Inhibition. *ACS nano* **2016,** *10* (2), 2766-73; (b) Henderson, B. W.; Waldow, S. M.; Potter, W. R.; Dougherty, T. J., Interaction of Photodynamic Therapy and Hyperthermia: Tumor Response and Cell Survival Studies after Treatment of Mice in Vivo. *Cancer Research* **1985,** *45* (12 Part 1), 6071-6077.
82. Nahabedian, M. Y.; Cohen, R. A.; Contino, M. F.; Terem, T. M.; Wright, W. H.; Berns, M. W.; Wile, A. G., Combination cytotoxic chemotherapy with cisplatin or doxorubicin and photodynamic therapy in murine tumors. *Journal of the National Cancer Institute* **1988,** *80* (10), 739-43.
83. Chung, U. S.; Kim, J. H.; Kim, B.; Kim, E.; Jang, W. D.; Koh, W. G., Dendrimer porphyrin-coated gold nanoshells for the synergistic combination of photodynamic and photothermal therapy. *Chem Commun (Camb)* **2016,** *52* (6), 1258-61.
84. Zhang, D.; Wu, M.; Zeng, Y.; Wu, L.; Wang, Q.; Han, X.; Liu, X.; Liu, J., Chlorin e6 Conjugated Poly(dopamine) Nanospheres as PDT/PTT Dual-Modal Therapeutic Agents for Enhanced Cancer Therapy. *ACS applied materials & interfaces* **2015,** *7* (15), 8176-87.

85. DeSantis, C.; Ma, J.; Bryan, L.; Jemal, A., Breast cancer statistics, 2013. *CA: a cancer journal for clinicians* **2014,** *64* (1), 52-62.
86. Steeg, P. S.; Theodorescu, D., Metastasis: a therapeutic target for cancer. *Nature clinical practice. Oncology* **2008,** *5* (4), 206-19.
87. Redig, A. J.; McAllister, S. S., Breast cancer as a systemic disease: a view of metastasis. *Journal of internal medicine* **2013,** *274* (2), 113-26.
88. Ledzewicz, U.; Maurer, H.; Schattler, H., Optimal and suboptimal protocols for a mathematical model for tumor anti-angiogenesis in combination with chemotherapy. *Math Biosci Eng* **2011,** *8* (2), 307-23.
89. Sandler, A.; Gray, R.; Perry, M. C.; Brahmer, J.; Schiller, J. H.; Dowlati, A.; Lilenbaum, R.; Johnson, D. H., Paclitaxel-carboplatin alone or with bevacizumab for non-small-cell lung cancer. *The New England journal of medicine* **2006,** *355* (24), 2542-50.
90. Wan, L.; Pantel, K.; Kang, Y., Tumor metastasis: moving new biological insights into the clinic. *Nature medicine* **2013,** *19* (11), 1450-64.
91. (a) Turner, N.; Grose, R., Fibroblast growth factor signalling: from development to cancer. *Nature reviews. Cancer* **2010,** *10* (2), 116-29; (b) Holland, E. C.; Varmus, H. E., Basic fibroblast growth factor induces cell migration and proliferation after glia-specific gene transfer in mice. *Proceedings of the National Academy of Sciences of the United States of America* **1998,** *95* (3), 1218-23; (c) Rogelj, S.; Klagsbrun, M.; Atzmon, R.; Kurokawa, M.; Haimovitz, A.; Fuks, Z.; Vlodavsky, I., Basic fibroblast growth factor is an extracellular matrix component required for supporting the proliferation of vascular endothelial cells and the differentiation of PC12 cells. *The Journal of cell biology* **1989,** *109* (2), 823-31; (d) Tomlinson, D. C.; Lamont, F. R.; Shnyder, S. D.; Knowles, M. A., Fibroblast growth factor receptor 1 promotes proliferation and survival via activation of the mitogen-activated protein kinase pathway in bladder cancer. *Cancer research* **2009,** *69* (11), 4613-20; (e) Hanahan, D.; Folkman, J., Patterns and emerging mechanisms of the angiogenic switch during tumorigenesis. *Cell* **1996,** *86* (3), 353-64; (f) Akita, S.; Akino, K.; Imaizumi, T.; Hirano, A., Basic fibroblast growth factor accelerates and improves second-degree burn wound healing. *Wound repair and regeneration : official publication of the Wound Healing Society [and] the European Tissue Repair Society* **2008,** *16* (5), 635-41; (g) Klein-Soyer, C.; Beretz, A.; Cazenave, J. P.; Driot, F.; Maffrand, J. P., Behavior of confluent endothelial cells after irradiation. Modulation of wound repair by heparin and acidic fibroblast growth factor. *Biology of the cell / under the auspices of the European Cell Biology Organization* **1990,** *68* (3), 231-8.
92. (a) Beenken, A.; Mohammadi, M., The FGF family: biology, pathophysiology and therapy. *Nature reviews. Drug discovery* **2009,** *8* (3), 235-53; (b) Haugsten, E. M.; Wiedlocha, A.; Olsnes, S.; Wesche, J., Roles of fibroblast growth factor receptors in carcinogenesis. *Molecular cancer research : MCR* **2010,** *8* (11), 1439-52; (c) Gao, F. J.; Hebbar, S.; Gao, X. A.; Alexander, M.; Pandey, J. P.; Walla, M. D.; Cotham, W. E.; King, S. J.; Smith, D. S., GSK-3beta Phosphorylation of Cytoplasmic Dynein Reduces Ndel1 Binding to Intermediate Chains and Alters Dynein Motility. *Traffic* **2015,** *16* (9), 941-61.

93. (a) Daniele, G.; Corral, J.; Molife, L. R.; de Bono, J. S., FGF receptor inhibitors: role in cancer therapy. *Current oncology reports* **2012,** *14* (2), 111-9; (b) Dieci, M. V.; Arnedos, M.; Andre, F.; Soria, J. C., Fibroblast growth factor receptor inhibitors as a cancer treatment: from a biologic rationale to medical perspectives. *Cancer discovery* **2013,** *3* (3), 264-79; (c) Hussain, S.; Slevin, M.; Ahmed, N.; West, D.; Choudhary, M. I.; Naz, H.; Gaffney, J., Stilbene glycosides are natural product inhibitors of FGF-2-induced angiogenesis. *BMC cell biology* **2009,** *10*, 30; (d) Takano, S.; Gately, S.; Neville, M. E.; Herblin, W. F.; Gross, J. L.; Engelhard, H.; Perricone, M.; Eidsvoog, K.; Brem, S., Suramin, an anticancer and angiosuppressive agent, inhibits endothelial cell binding of basic fibroblast growth factor, migration, proliferation, and induction of urokinase-type plasminogen activator. *Cancer research* **1994,** *54* (10), 2654-60; (e) Gudernova, I.; Vesela, I.; Balek, L.; Buchtova, M.; Dosedelova, H.; Kunova, M.; Pivnicka, J.; Jelinkova, I.; Roubalova, L.; Kozubik, A.; Krejci, P., Multikinase activity of fibroblast growth factor receptor (FGFR) inhibitors SU5402, PD173074, AZD1480, AZD4547 and BGJ398 compromises the use of small chemicals targeting FGFR catalytic activity for therapy of short-stature syndromes. *Human molecular genetics* **2016,** *25* (1), 9-23; (f) Hierro, C.; Rodon, J.; Tabernero, J., Fibroblast Growth Factor (FGF) Receptor/FGF Inhibitors: Novel Targets and Strategies for Optimization of Response of Solid Tumors. *Seminars in oncology* **2015,** *42* (6), 801-19; (g) Kumar, S. B.; Narasu, L.; Gundla, R.; Dayam, R.; J, A. R. P. S., Fibroblast growth factor receptor inhibitors. *Current pharmaceutical design* **2013,** *19* (4), 687-701; (h) Lewin, J.; Siu, L. L., Development of Fibroblast Growth Factor Receptor Inhibitors: Kissing Frogs to Find a Prince? *Journal of clinical oncology : official journal of the American Society of Clinical Oncology* **2015,** *33* (30), 3372-4.

94. (a) Danesi, R.; Del Bianchi, S.; Soldani, P.; Campagni, A.; La Rocca, R. V.; Myers, C. E.; Paparelli, A.; Del Tacca, M., Suramin inhibits bFGF-induced endothelial cell proliferation and angiogenesis in the chick chorioallantoic membrane. *British journal of cancer* **1993,** *68* (5), 932-8; (b) Waltenberger, J.; Mayr, U.; Frank, H.; Hombach, V., Suramin is a potent inhibitor of vascular endothelial growth factor. A contribution to the molecular basis of its antiangiogenic action. *Journal of molecular and cellular cardiology* **1996,** *28* (7), 1523-9; (c) Park, J.; Kim, J. Y.; Hwang, S. R.; Mahmud, F.; Byun, Y., Chemical Conjugate of Low Molecular Weight Heparin and Suramin Fragment Inhibits Tumor Growth Possibly by Blocking VEGF165. *Molecular pharmaceutics* **2015,** *12* (11), 3935-42; (d) Song, S.; Wientjes, M. G.; Walsh, C.; Au, J. L., Nontoxic doses of suramin enhance activity of paclitaxel against lung metastases. *Cancer Res* **2001,** *61* (16), 6145-50; (e) Song, S.; Wientjes, M. G.; Gan, Y.; Au, J. L., Fibroblast growth factors: an epigenetic mechanism of broad spectrum resistance to anticancer drugs. *Proc Natl Acad Sci U S A* **2000,** *97* (15), 8658-63; (f) Zhang, Y.; Song, S.; Yang, F.; Au, J. L.; Wientjes, M. G., Nontoxic doses of suramin enhance activity of doxorubicin in prostate tumors. *J Pharmacol Exp Ther* **2001,** *299* (2), 426-33; (g) Song, S.; Yu, B.; Wei, Y.; Wientjes, M. G.; Au, J. L., Low-dose suramin enhanced paclitaxel activity in chemotherapy-naive and paclitaxel-pretreated human breast xenograft tumors. *Clin Cancer Res* **2004,** *10*

(18 Pt 1), 6058-65; (h) Singla, A. K.; Bondareva, A.; Jirik, F. R., Combined treatment with paclitaxel and suramin prevents the development of metastasis by inhibiting metastatic colonization of circulating tumor cells. *Clinical & experimental metastasis* **2014,** *31* (6), 705-14.
95. Tu, S. M.; Pagliaro, L. C.; Banks, M. E.; Amato, R. J.; Millikan, R. E.; Bugazia, N. A.; Madden, T.; Newman, R. A.; Logothetis, C. J., Phase I study of suramin combined with doxorubicin in the treatment of androgen-independent prostate cancer. *Clin Cancer Res* **1998,** *4* (5), 1193-201.
96. Kosarek, C. E.; Hu, X.; Couto, C. G.; Kisseberth, W. C.; Green, E. M.; Au, J. L.; Wientjes, M. G., Phase I evaluation of low-dose suramin as chemosensitizer of doxorubicin in dogs with naturally occurring cancers. *Journal of veterinary internal medicine / American College of Veterinary Internal Medicine* **2006,** *20* (5), 1172-7.
97. Bowden, C. J.; Figg, W. D.; Dawson, N. A.; Sartor, O.; Bitton, R. J.; Weinberger, M. S.; Headlee, D.; Reed, E.; Myers, C. E.; Cooper, M. R., A phase I/II study of continuous infusion suramin in patients with hormone-refractory prostate cancer: toxicity and response. *Cancer chemotherapy and pharmacology* **1996,** *39* (1-2), 1-8.
98. (a) Gan, Q.; Wang, T.; Cochrane, C.; McCarron, P., Modulation of surface charge, particle size and morphological properties of chitosan-TPP nanoparticles intended for gene delivery. *Colloids Surf B Biointerfaces* **2005,** *44* (2-3), 65-73; (b) Jonassen, H.; Kjoniksen, A. L.; Hiorth, M., Stability of chitosan nanoparticles cross-linked with tripolyphosphate. *Biomacromolecules* **2012,** *13* (11), 3747-56.
99. (a) Aston, R.; Wimalaratne, M.; Brock, A.; Lawrie, G.; Grondahl, L., Interactions between Chitosan and Alginate Dialdehyde Biopolymers and Their Layer-by-Layer Assemblies. *Biomacromolecules* **2015,** *16* (6), 1807-17; (b) Biswas, S.; Chattopadhyay, M.; Sen, K. K.; Saha, M. K., Development and characterization of alginate coated low molecular weight chitosan nanoparticles as new carriers for oral vaccine delivery in mice. *Carbohydr Polym* **2015,** *121*, 403-10.
100. (a) Csaba, N.; Koping-Hoggard, M.; Fernandez-Megia, E.; Novoa-Carballal, R.; Riguera, R.; Alonso, M. J., Ionically crosslinked chitosan nanoparticles as gene delivery systems: effect of PEGylation degree on in vitro and in vivo gene transfer. *J Biomed Nanotechnol* **2009,** *5* (2), 162-71; (b) Santander-Ortega, M. J.; Peula-Garcia, J. M.; Goycoolea, F. M.; Ortega-Vinuesa, J. L., Chitosan nanocapsules: Effect of chitosan molecular weight and acetylation degree on electrokinetic behaviour and colloidal stability. *Colloids Surf B Biointerfaces* **2011,** *82* (2), 571-80; (c) Huang, Y.; Lapitsky, Y., Monovalent salt enhances colloidal stability during the formation of chitosan/tripolyphosphate microgels. *Langmuir* **2011,** *27* (17), 10392-9.
101. (a) Elsayed, A.; Al-Remawi, M.; Qinna, N.; Farouk, A.; Al-Sou'od, K. A.; Badwan, A. A., Chitosan–Sodium Lauryl Sulfate Nanoparticles as a Carrier System for the In Vivo Delivery of Oral Insulin. *Aaps Pharmscitech* **2011,** *12* (3), 958-964; (b) El-Gibaly, I.; Meki, A. M.; Abdel-Ghaffar, S. K., Novel B melatonin-loaded chitosan microcapsules: in vitro characterization and antiapoptosis

efficacy for aflatoxin B1-induced apoptosis in rat liver. *International journal of pharmaceutics* **2003,** *260* (1), 5-22.
102. Chen, Y. L.; Wang, C. Y.; Yang, F. Y.; Wang, B. S.; Chen, J. Y.; Lin, L. T.; Leu, J. D.; Chiu, S. J.; Chen, F. D.; Lee, Y. J.; Chen, W. R., Synergistic effects of glycated chitosan with high-intensity focused ultrasound on suppression of metastases in a syngeneic breast tumor model. *Cell death & disease* **2014,** *5*, e1178.
103. Li, S.; Payne, S.; Wang, F.; Claus, P.; Su, Z.; Groth, J.; Geradts, J.; de Ridder, G.; Alvarez, R.; Marcom, P. K.; Pizzo, S. V.; Bachelder, R. E., Nuclear basic fibroblast growth factor regulates triple-negative breast cancer chemo-resistance. *Breast Cancer Res* **2015,** *17*, 91.
104. Foekens, J. A.; Sieuwerts, A. M.; Stuurman-Smeets, E. M.; Dorssers, L. C.; Berns, E. M.; Klijn, J. G., Pleiotropic actions of suramin on the proliferation of human breast-cancer cells in vitro. *Int J Cancer* **1992,** *51* (3), 439-44.
105. Li, H.; Li, H.; Qu, H.; Zhao, M.; Yuan, B.; Cao, M.; Cui, J., Suramin inhibits cell proliferation in ovarian and cervical cancer by downregulating heparanase expression. *Cancer Cell Int* **2015,** *15*, 52.
106. Lelievre, S.; Benchokroun, Y.; Larsen, A. K., Altered topoisomerase I and II activities in suramin-resistant lung fibrosarcoma cells. *Molecular pharmacology* **1995,** *47* (5), 898-906.
107. Gagliardi, A. R.; Taylor, M. F.; Collins, D. C., Uptake of suramin by human microvascular endothelial cells. *Cancer Lett* **1998,** *125* (1-2), 97-102.
108. Wang, T.; Bai, J.; Jiang, X.; Nienhaus, G. U., Cellular uptake of nanoparticles by membrane penetration: a study combining confocal microscopy with FTIR spectroelectrochemistry. *ACS nano* **2012,** *6* (2), 1251-9.
109. (a) Rashid, O. M.; Nagahashi, M.; Ramachandran, S.; Dumur, C. I.; Schaum, J. C.; Yamada, A.; Aoyagi, T.; Milstien, S.; Spiegel, S.; Takabe, K., Is tail vein injection a relevant breast cancer lung metastasis model? *J Thorac Dis* **2013,** *5* (4), 385-92; (b) Khanna, C.; Hunter, K., Modeling metastasis in vivo. *Carcinogenesis* **2005,** *26* (3), 513-23; (c) Elkin, M.; Vlodavsky, I., Tail vein assay of cancer metastasis. *Current protocols in cell biology / editorial board, Juan S. Bonifacino ... [et al.]* **2001,** *Chapter 19*, Unit 19 2.
110. (a) Plaksin, D.; Gelber, C.; Feldman, M.; Eisenbach, L., Reversal of the metastatic phenotype in Lewis lung carcinoma cells after transfection with syngeneic H-2Kb gene. *Proc Natl Acad Sci U S A* **1988,** *85* (12), 4463-7; (b) Bugge, T. H.; Kombrinck, K. W.; Xiao, Q.; Holmback, K.; Daugherty, C. C.; Witte, D. P.; Degen, J. L., Growth and dissemination of Lewis lung carcinoma in plasminogen-deficient mice. *Blood* **1997,** *90* (11), 4522-31.
111. Ichikawa, Y.; Ghanefar, M.; Bayeva, M.; Wu, R.; Khechaduri, A.; Naga Prasad, S. V.; Mutharasan, R. K.; Naik, T. J.; Ardehali, H., Cardiotoxicity of doxorubicin is mediated through mitochondrial iron accumulation. *J Clin Invest* **2014,** *124* (2), 617-30.
112. Miranda, C. J.; Makui, H.; Soares, R. J.; Bilodeau, M.; Mui, J.; Vali, H.; Bertrand, R.; Andrews, N. C.; Santos, M. M., Hfe deficiency increases susceptibility to cardiotoxicity and exacerbates changes in iron metabolism induced by doxorubicin. *Blood* **2003,** *102* (7), 2574-80.

APPENDIX A - COPYRIGHT RELEASE

1. The evidence for copyright release of Chapter 1

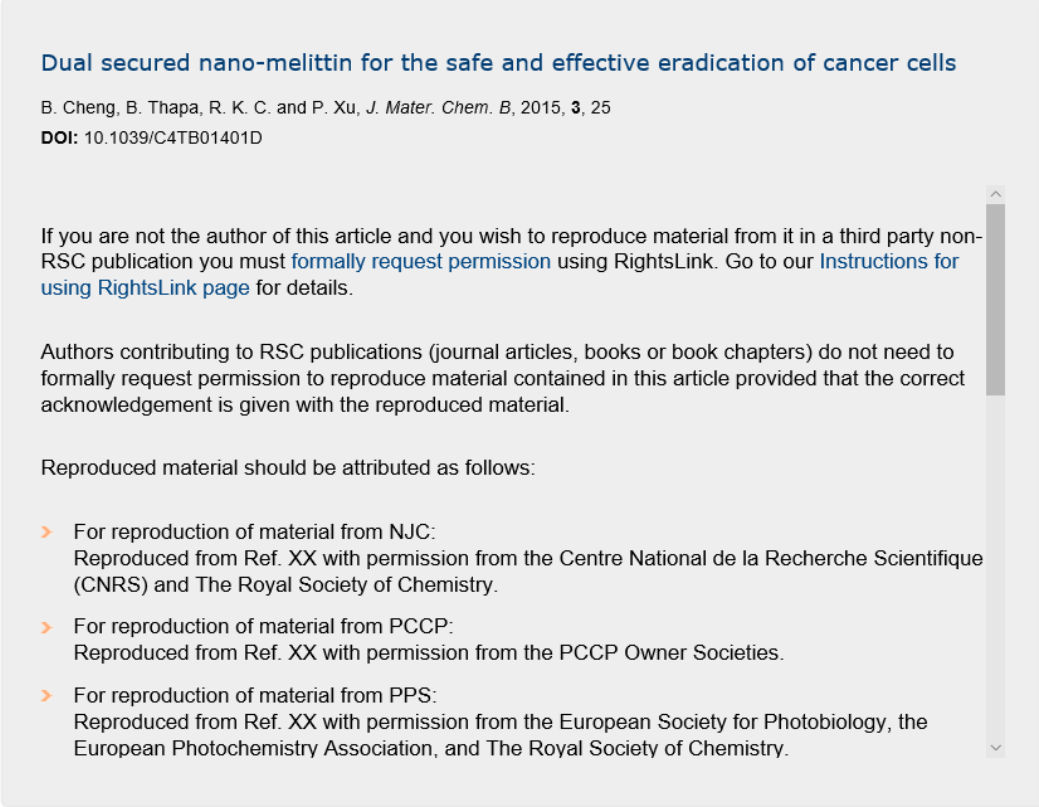

Dual secured nano-melittin for the safe and effective eradication of cancer cells

B. Cheng, B. Thapa, R. K. C. and P. Xu, *J. Mater. Chem. B*, 2015, **3**, 25

DOI: 10.1039/C4TB01401D

If you are not the author of this article and you wish to reproduce material from it in a third party non-RSC publication you must formally request permission using RightsLink. Go to our Instructions for using RightsLink page for details.

Authors contributing to RSC publications (journal articles, books or book chapters) do not need to formally request permission to reproduce material contained in this article provided that the correct acknowledgement is given with the reproduced material.

Reproduced material should be attributed as follows:

- For reproduction of material from NJC:
  Reproduced from Ref. XX with permission from the Centre National de la Recherche Scientifique (CNRS) and The Royal Society of Chemistry.
- For reproduction of material from PCCP:
  Reproduced from Ref. XX with permission from the PCCP Owner Societies.
- For reproduction of material from PPS:
  Reproduced from Ref. XX with permission from the European Society for Photobiology, the European Photochemistry Association, and The Royal Society of Chemistry.

2. The evidence for copyright release of Chapter 2

Dear Bei Cheng:

American Scientific Publishers grants permission to reuse the following whole article or parts of it in the forthcoming PhD thesis.

Cheng, B., He, H., Huang, T., Berr, S., He, J., Fan D., Zhang, J., and Xu, P, Gold Nanosphere Gated Mesoporous Silica Nanoparticle Responsive to NIR Light and

Redox Potential as a Theranostic Platform for Cancer Therapy. J. Biomed. Nanotechnol. 12, 435-449 (2016)

Best regards,

H. S. Nalwa, PhD

Publisher

Dr. Hari Singh Nalwa | Editor-in-Chief: Journal of Nanoscience and Nanotechnology | Web: www.aspbs.com/jnn

Editor: Encyclopedia of Nanoscience and Nanotechnology (25-Volume set) | Web: www.aspbs.com/enn

American Scientific Publishers | 26650 The Old Road, Suite 208, Valencia , California 91381-0751 , USA